

“I find that some parts [...] are less interesting than the most interesting ones.” -Referee A

2D Semiconductor-Superconductor Hybrids



Henri J. Suominen

Two-dimensional Semiconductor- Superconductor Hybrids

Henri J. Suominen

TWO-DIMENSIONAL
SEMICONDUCTOR-SUPERCONDUCTOR
HYBRIDS

HENRI J. SUOMINEN

Ph.D. Thesis
Center for Quantum Devices
Station Q Copenhagen
Niels Bohr Institute
University of Copenhagen

Academic advisor:
Prof. Charles M. Marcus

Assessment committee:
Prof. Jens Paaske
Prof. Bart van Wees
Dr. Francesco Giazotto

September 2017

ABSTRACT

This thesis investigates hybrid two-dimensional semiconductor-superconductor (Sm-S) devices and presents a new material platform exhibiting intimate Sm-S coupling straight *out of the box*.

Starting with the conventional approach, we investigate coupling superconductors to buried quantum well heterostructures, observing clear evidence of supercurrent, and the first direct spectroscopy of an induced superconducting gap in a two-dimensional electron gas. Nonetheless, these experiments reveal inhomogeneous contacts and a soft-induced superconducting gap, likely due to disorder at the Sm-S interface

To overcome these issues we integrate the superconductor directly into the semiconducting material growth stack, depositing it *in-situ* in a molecular beam epitaxy system under high vacuum. We present a number of experiments on these hybrid heterostructures, demonstrating near unity interface transparency and a hard induced superconducting gap. Furthermore the thin superconducting (< 10 nm) aluminium films allow for the application of large in-plane magnetic fields without destroying superconductivity. In such a scenario we investigate the magneto-transport properties in S-Sm-S junctions, revealing anomalous Fraunhofer diffraction, qualitatively in agreement with a complex interplay between Zeeman coupling, spin-orbit interaction and disorder.

Finally by patterning quasi-one-dimensional structures we observe coalescing Andreev bound states stabilizing at zero energy in large magnetic fields, in agreement with previous reports of Majorana modes in semiconductor nanowires. By offering a patternable two-dimensional platform our approach opens up the door

to experiments probing the predicted topological properties in this system.

ACKNOWLEDGMENTS

This work would not have been possible without an enormous amount of support from countless people. First I would like to thank Charlie for the opportunity of carrying out my Ph.D. at Qdev and providing an amazing scientific environment (including but not limited to top of the line facilities, excellent coffee, clean lab aesthetic, and a limitless supply of materials and extensive network of collaborators). Moreover, thank you Charlie for your support and guidance, and imparting your scientific vision and attention to detail.

Much of this thesis owes itself to an intimate collaboration with Morten Kjaergaard and Fabrizio Nichele, thank you both for the all the long hours in the cleanroom and in front of the fridge. Javad Shabani, thank you for the amazing work growing epitaxial aluminum/InAs wafers, much of this thesis would likely describe fabrication recipes and hunts for leakage paths if it were not for this fruitful collaboration. To the rest of the 2DEG team, Charlotte Böttcher, Asbjorn Drachmann, Alexander Whitticar, Eoin O'Farrel and Antonio Fornieri thank you for many good times and for picking up the pieces while I was away writing.

The first months at Qdev would not have been quite as welcoming had it not been for a trumpet echoing through the corridors of Qdev followed by plenty of Chinese hotpot and whisky, thank you for those memories Willy Chang. Sven Albrecht, thank you for the constant entertainment, amazing photoshops, and supply of Soy-lent bars to power the long nights. Thorvald Larsen and Christian Olsen, thank you for the many in-lab dinners and much needed weekly Wednesday.

Jeroen Danon, thank you for wading through the seemingly impassable Anomalous Fraunhofer project with me. It is unlikely that data would ever have graced the light of day, much less the PRB kaleidoscope without your theoretical support. Shivendra Upadhyay, thank you for your near limitless support at all hours of the day, and patience with our reinterpretations of the machine booking policies (and other reasonably unreasonable requests). Ferdinand Kuemmeth, thank you for teaching me how to hunt down noise sources, locate fridge leaks, and countless other technical tricks. Thank you also to Karsten Flensburg for many enlightening discussions. Konrad Wölms and Sam Sanchez, thank you for putting up with me trying to understand topological insulators, and invaluable tips optimizing tight-binding simulations. Alex Hamilton, thank you spreading the Aussie sunshine in Copenhagen, babysitting our samples, and surprising me with random Finnish chat. The Qdev administrative team also deserves a massive thank you for all their hard work. Thanks especially to Jess Martin, Katrin Hjorth, and Dorthe Bjergskov.

I would also like to thank Kasper Grove-Rasmussen for showing me around HCØ before Qdev existed, and the NTT Butsuryo group, especially Satoshi Sasaski and Koji Muraki for early encouragement and the tip that Charlie was moving to Copenhagen. Thank you to Prof. Bart van Wees and Dr. Francesco Giazotto for accepting the invitation to act on the thesis assessment committee.

Finally a huge thank you to Emma and my family for the unfaltering support over the years, and understanding when experiments in the fridge seemed to take precedence over everything else.

PUBLICATIONS

EPITAXIAL SEMICONDUCTOR-SUPERCONDUCTOR HETEROSTRUCTURES

The work elaborated in this thesis is partially an adaptation of the following peer-reviewed articles, with a focus on [2], [4], and [5]

- [1] F. Nichele, A. C. C. Drachmann, A. M. Whiticar, E. C. O'Farrel, **H. J. Suominen**, A. Fornieri, T. Wang, G. C. Gardner, C. Thomas, A. T. Hatke, P. Krogstrup, M. J. Manfra, K. Flensberg, and C. M. Marcus. "Scaling of Majorana Zero-Bias Conductance Peaks." *Accepted in Physical Review Letters* (2017).
- [2] **H. J. Suominen**, M. Kjaergaard, A. R. Hamilton, J. Shabani, C. J. Palmstrøm, C. M. Marcus, and F. Nichele. "Zero-Energy Modes from Coalescing Andreev States in a Two-Dimensional Semiconductor-Superconductor Hybrid Platform." *Under review* (2017).
- [3] A. C. C. Drachmann, **H. J. Suominen**, M. Kjaergaard, B. Shojaei, C. J. Palmstrøm, C. M. Marcus, and F. Nichele. "Proximity Effect Transfer from NbTi into a Semiconductor Heterostructure via Epitaxial Aluminum." *Nano Letters* 17.2 (2017), pp. 1200–1203. DOI: [10.1021/acs.nanolett.6b04964](https://doi.org/10.1021/acs.nanolett.6b04964).
- [4] M. Kjaergaard*, **H. J. Suominen***, M. P. Nowak, A. R. Akhmerov, J. Shabani, C. J. Palmstrøm, F. Nichele, and C. M. Marcus. "Transparent Semiconductor-Superconductor Interface and Induced Gap in an Epitaxial Heterostructure Josephson Junction." *Physical Review Applied* 7 (3 2017), p. 034029. DOI: [10.1103/PhysRevApplied.7.034029](https://doi.org/10.1103/PhysRevApplied.7.034029).

* Equal contribution

- [5] **H. J. Suominen**, J. Danon, M. Kjaergaard, K. Flensberg, J. Shabani, C. J. Palmstrøm, F. Nichele, and C. M. Marcus. “Anomalous Fraunhofer interference in epitaxial superconductor-semiconductor Josephson junctions.” *Physical Review B* 95 (3 2017), p. 035307. DOI: [10.1103/PhysRevB.95.035307](https://doi.org/10.1103/PhysRevB.95.035307).
- [6] M. Kjaergaard, F. Nichele, **H. J. Suominen**, M. P. Nowak, M. Wimmer, A. R. Akhmerov, J. A. Folk, K. Flensberg, J. Shabani, C. J. Palmstrøm, and C. M. Marcus. “Quantized conductance doubling and hard gap in a two-dimensional semiconductor–superconductor heterostructure.” *Nature Communications* 7 (2016), p. 12841. DOI: [10.1038/ncomms12841](https://doi.org/10.1038/ncomms12841).
- [7] A. Rasmussen, J. Danon, **H. J. Suominen**, F. Nichele, M. Kjaergaard, and K. Flensberg. “Effects of spin-orbit coupling and spatial symmetries on the Josephson current in SNS junctions.” *Physical Review B* 93 (15 2016), p. 155406. DOI: [10.1103/PhysRevB.93.155406](https://doi.org/10.1103/PhysRevB.93.155406).
- [8] J. Shabani, M. Kjaergaard, **H. J. Suominen**, Y. Kim, F. Nichele, K. Pakrouski, T. Stankevic, R. M. Lutchyn, P. Krogstrup, R. Feidenhans'l, S. Kraemer, C. Nayak, M. Troyer, C. M. Marcus, and C. J. Palmstrøm. “Two-dimensional epitaxial superconductor-semiconductor heterostructures: A platform for topological superconducting networks.” *Physical Review B* 93 (15 2016), p. 155402. DOI: [10.1103/PhysRevB.93.155402](https://doi.org/10.1103/PhysRevB.93.155402).

These works, whilst part of the research undertaken during this Ph.D., are not included in this thesis.

- [1] F. Nichele, M. Kjaergaard, **H. J. Suominen**, R. Skolasinski, M. Wimmer, B.-M. Nguyen, A. A. Kiselev, W. Yi, M. Sokolich, M. J. Manfra, F. Qu, A. J. A. Beukman, L. P. Kouwenhoven, and C. M. Marcus. "Giant Spin-Orbit Splitting in Inverted InAs/GaSb Double Quantum Wells." *Physical Review Letters* 118 (1 2017), p. 016801. DOI: [10.1103/PhysRevLett.118.016801](https://doi.org/10.1103/PhysRevLett.118.016801).
- [2] B.-M. Nguyen, A. A. Kiselev, R. Noah, W. Yi, F. Qu, A. J. A. Beukman, F. K. de Vries, J. van Veen, S. Nadj-Perge, L. P. Kouwenhoven, M. Kjaergaard, **H. J. Suominen**, F. Nichele, C. M. Marcus, M. J. Manfra, and M. Sokolich. "Decoupling Edge Versus Bulk Conductance in the Trivial Regime of an InAs/GaSb Double Quantum Well Using Corbino Ring Geometry." *Physical Review Letters* 117 (7 2016), p. 077701. DOI: [10.1103/PhysRevLett.117.077701](https://doi.org/10.1103/PhysRevLett.117.077701).
- [3] F. Nichele, **H. J. Suominen**, M. Kjaergaard, C. M. Marcus, E. Sajadi, J. A. Folk, F. Qu, A. J. A. Beukman, F. K. de Vries, J. van Veen, S. Nadj-Perge, L. P. Kouwenhoven, B.-M. Nguyen, A. A. Kiselev, W. Yi, M. Sokolich, M. J. Manfra, E. M. Spanton, and K. A. Moler. "Edge transport in the trivial phase of InAs/GaSb." *New Journal of Physics* 18.8 (2016), p. 083005. DOI: [10.1088/1367-2630/18/8/083005](https://doi.org/10.1088/1367-2630/18/8/083005).

CONTENTS

I	COUPLING SEMICONDUCTORS AND SUPERCONDUCTORS	1
1	BUILDING BLOCKS	3
1.1	Introduction	4
1.2	Two-dimensional electron gas	5
1.2.1	Surface accumulation layers	5
1.2.2	Quantum well heterostructures	7
1.2.3	Determining density and mobility	11
1.2.4	Spin-orbit interaction	12
1.2.5	Competition between Zeeman and SOI	14
1.2.6	Quantum point contact	17
1.2.7	Choice of material system	19
1.3	Superconductivity	23
1.4	Hybrid structures	26
1.4.1	Andreev reflection	26
1.4.2	The Josephson junction	31
1.4.3	Andreev bound states to a supercurrent	31
1.4.4	Fraunhofer pattern	34
1.5	Topological hybrids	37
1.5.1	Majorana fermions	37
1.5.2	A recipe	37
2	THE LONG ROAD TO HYBRIDS	41
II	EX-SITU SUPERCONDUCTING CONTACTS	44
3	BURIED STRUCTURES	47
3.1	InAs 2DEG	47
3.2	Supercurrent	53
3.2.1	Inhomogeneous contacts	53

3.3	Confined geometries	56
3.3.1	Supercurrent in SNS configuration	56
3.3.2	Tunneling spectroscopy	58
3.4	Outlook	59
III EPITAXIAL SUPERCONDUCTING CONTACTS		62
4	SUPERCONDUCTOR-SEMICONDUCTOR HETEROSTRUCTURES	65
4.1	Introduction to a new platform	65
4.1.1	Material considerations	65
4.2	Fabrication	70
4.3	Al and 2DEG properties	74
4.3.1	Al film	74
4.3.2	Two-dimensional electron gas	75
4.4	Andreev Quantum Point Contact	79
5	TRANSPARENT INTERFACES	83
5.1	Josephson junction in a QW heterostructure	83
5.2	Multiple Andreev reflection	86
5.3	Electrostatic gate dependence	90
5.4	Elucidating the induced gap	93
5.5	Conclusion	95
6	ANOMALOUS FRAUNHOFER INTERFERENCE	97
6.1	Methods	99
6.2	Perpendicular magnetic field	101
6.3	In-plane magnetic field	106
6.4	Combined perpendicular & in-plane magnetic fields	110
6.4.1	SNS-to-SQUID transition	110
6.4.2	Asymmetries in the interference patterns	115
6.5	Conclusion	121
7	SCALABLE MAJORANA DEVICES	123
7.1	Ballistic tunnel probe	123
7.2	Magnetic field regimes	128
7.3	Majorana zero modes	129

7.4	Magnetic field angle and temperature dependence	130
7.5	Conclusion	131
IV	APPENDIX	133
A	EPITAXIAL HETEROSTRUCTURE FABRICATION	135
B	ANOMALOUS FRAUNHOFER SIMULATIONS	141
B.1	Estimating \mathbf{B}_{c1}	141
B.2	Gate dependence	142
B.3	Additional devices	145
B.3.1	Flux focusing control device	145
B.3.2	Devices rotated with respect to crystal axes	145
B.4	Tight binding simulations	149
C	WIRE DEVICES	155
C.1	Single channel junction	155
C.2	Superconducting transitions	157
C.3	S-QPC-N and S-QPC-S	160
C.4	Subgap state g-factors	160
	BIBLIOGRAPHY	163

LIST OF FIGURES

Figure 1.1	Superconductor and semiconductor building blocks	5
Figure 1.2	Interface band bending	6
Figure 1.3	Rectangular QW heterostructure	8
Figure 1.4	Hall characterization.	11
Figure 1.5	Rashba SOI.	16
Figure 1.6	Quantum point contact	19
Figure 1.7	III-V material comparison	22
Figure 1.8	Superconducting density of states.	24
Figure 1.9	Andreev reflection	25
Figure 1.10	BTK coefficients as a function of barrier transparency	30
Figure 1.11	Fraunhofer diffraction	36
Figure 1.12	Bandstructure of a one dimensional wire with SOI, superconductivity, and Zeeman coupling.	40
Figure 2.1	Development of 2D Sm-S hybrids	43
Figure 3.1	Buried InAs 2DEG.	48
Figure 3.2	2DEG device fabrication	48
Figure 3.3	Contact strategies to buried 2DEGs.	50
Figure 3.4	Buried S-2DEG-S device.	52
Figure 3.5	Inhomogeneous contacts.	54
Figure 3.6	Irregular Fraunhofer interference.	55
Figure 3.7	Wire device scanning electron micrograph.	56
Figure 3.8	Supercurrent in confined buried structures.	57
Figure 3.9	Tunneling spectroscopy in a buried structure.	60
Figure 4.1	Superconductor-semiconductor hybrid material considerations.	66
Figure 4.2	Superconductor-semiconductor epitaxy.	69

Figure 4.3	Epitaxial device fabrication.	72
Figure 4.4	CAD chip layout	73
Figure 4.5	Epitaxial aluminum film properties.	74
Figure 4.6	Two-dimensional electron gas properties.	78
Figure 4.7	Andreev quantum point contact	79
Figure 4.8	Hard superconducting gap	81
Figure 5.1	Andreev reflection in an S-2DEG-S device.	85
Figure 5.2	Multiple Andreev reflection as a function of gate voltage.	87
Figure 5.3	Simulations of multiple Andreev reflection for different junction transparencies.	89
Figure 5.4	Multisubband occupation revealed from MAR and the Hall slope	91
Figure 5.5	Temperature dependence of the gap inferred from MAR	94
Figure 6.1	SNS device schematic and Fraunhofer	102
Figure 6.2	Supercurrent in-plane magnetic field dependence	107
Figure 6.3	In-plane field induced Fraunhofer asymmetry	111
Figure 6.4	Flux dipole induced SNS to SQUID transition	113
Figure 6.5	Asymmetry evolution upon field rotation	117
Figure 7.1	Device schematic and behavior of the ballistic probe.	125
Figure 7.2	Superconducting gap in the tunneling regime and transition to an effective normal probe in a magnetic field.	126
Figure 7.3	Stable zero energy state at large in-plane field.	127
Figure 7.4	Stability of the zero bias peak as a function of field angle and temperature.	132
Figure A.1	Anodization.	140
Figure B.1	Supercurrent density gate dependence	143
Figure B.2	Gate dependence of the Fraunhofer asymmetry	144

Figure B.3	No flux focusing.	146
Figure B.4	Additional devices.	148
Figure B.5	Varying disorder configuration.	151
Figure B.6	Varying Zeeman strength.	152
Figure B.7	Effect of the dipole.	154
Figure C.1	Magnetic field tuning.	157
Figure C.2	Open and closed regimes.	159
Figure C.3	Behavior of proximitized 2D regions.	161
Figure C.4	Dependence of g factor on gate voltage.	162

Part I

COUPLING SEMICONDUCTORS AND
SUPERCONDUCTORS

BUILDING BLOCKS

The invention of the transistor at Bell labs in 1947 [1, 2] and subsequent development of integrated circuits [3] ushered in the modern era of pervasive computing devices, enabled by the ability of semiconducting materials to seamlessly transition from metallic conductors to insulators at the flip of a switch. This property of gate-tuneability has likewise opened up a rich field of mesoscopic physics [4] exploring electron transport in diverse nanoscale structures from quantum dots [5, 6], quantum point contacts [7], to interferometers [8].

Superconductivity, since its discovery in 1911 [9] has similarly driven vast technological change, owing to the ability of transporting electric current without dissipation. Moreover, the prediction by Brian D. Josephson in 1962 [10, 11] that a supercurrent could flow between two closely spaced but disconnected superconducting banks, has opened up a diverse field of superconducting electronics.

In comparison to these vast fields, hybrid systems have been slow to develop, in large part to the substantial difficulties of coupling them reproducibly. Recent years have however seen a dramatic resurgence of interest in such hybrid systems owing to the possibility of realizing topological systems applicable to quantum computing.

While both semiconducting and superconducting quantum computing platforms have been heavily investigated over the past years, both suffer from the inherent problem that information encoded in qubits (quantum analogues of transistors) is very fragile and short-lived. Topological systems theoretically allow for the encoding of

quantum information in extended states, offering an in-built protection from environmental noise.

One of the most promising candidates for realizing such systems are semiconducting nanowires with strong spin-orbit interaction and induced superconductivity, predicted to host topological Majorana bound states. Over the past few years a number of experiments on crystalline nanowires have reported results consistent with these predictions [12–17]. Experiments directly probing the topological properties of these systems however require access to a second spatial dimension in order to manipulate them by braiding.

1.1 INTRODUCTION

In this chapter we introduce the key concepts that underpin the work carried out in this thesis. The aim is to get a general feel for two-dimensional electron gases, superconductors, and coupled hybrid systems. At the end of the chapter we give an introduction to exotic properties that may arise in such hybrid systems, one of the key motivations for this work.

Condensed matter systems offer a versatile playground of components which can be combined to form a variety of systems. Imagine that we have two different types of Lego bricks, red ones representing semiconductors, and blue superconductors (Figure 1.1). Section 1.2 details the relevant properties of the semiconductor system followed by a brief introduction to superconductors in Section 1.3. Upon stacking these lego bricks, two types of systems can be constructed, a single superconductor-semiconductor (S-N) interface, or two stacked interfaces forming an S-N-S structure. These two types of structures are examined in Sections 1.4.1 and 1.4.2 respectively.

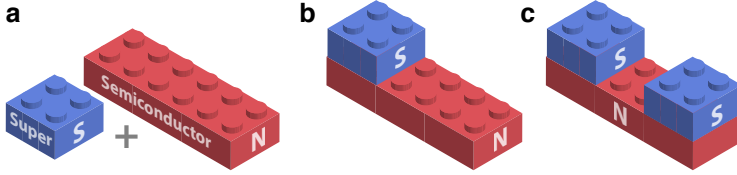


Figure 1.1: **Superconductor and semiconductor building blocks.** From two constituent building blocks (a), red representing a semiconductor and blue a superconductor, two types of structures can be built: single S-N interfaces (b) or S-N-S “weak-links” (c).

1.2 TWO-DIMENSIONAL ELECTRON GAS

Metals are typically described using the free electron model, with electrons in the conduction band roughly behaving like a gas of non-interacting electrons in three dimensions. Intrinsic semiconductors (without doping) on the other hand, at low temperature ($T \sim 1$ K), are expected to behave like insulators [18]. With the Fermi level aligned within the band gap and negligible thermal population of carriers, no transport should take place¹. Nonetheless, certain semiconductors curiously demonstrate significant surface conduction at low temperatures.

1.2.1 *Surface accumulation layers*

Figure 1.2 shows a vacuum-semiconductor interface for two typical semiconductors found in condensed matter physics laboratories, InAs (left) and GaAs (right). The zinc blende crystal structure, common to III- V semiconductors, terminating at a vacuum inter-

¹ The probability of exciting an electron from the valence band into the conduction band is $\sim \exp(-E_g/2k_B T)$, with E_g the band gap, k_B the Boltzmann constant, and T the temperature. With conventional semiconductor band gaps $E_g \sim 1$ eV and typical measurement temperatures of 0.03 K, this number is essentially zero.

face is shown in the upper panels. As a function of depth z from the surface ($z = 0$), the band alignment of the conduction and valence bands are shown below. For both materials, deep in the crystal the Fermi level E_F rests in the band gap. Approaching the vacuum-semiconductor interface however, the bands may bend up or down potentially crossing the Fermi level, depending on details of microscopic surface structure (and material composition).

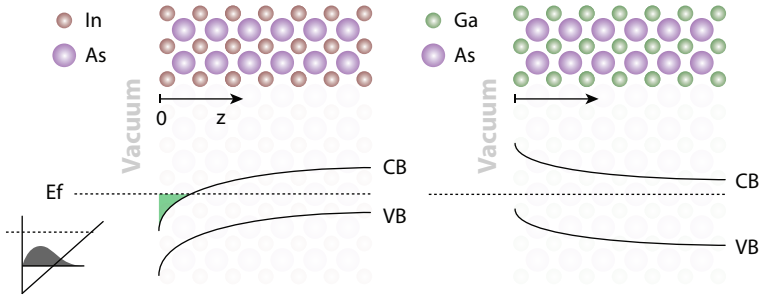


Figure 1.2: **Interface band bending.** Comparison of the typical band alignment at a vacuum-crystal interface for two typical III-V semiconductors, InAs (left) and GaAs (right).

Unique to the III-V group, in InAs the bands bend down at the surface such that the Fermi level crosses the conduction band [19–21]. Donor-like surface states pin the Fermi level above the conduction band minimum, whilst other III-Vs tend to form acceptor-like states at the surface causing the bands to bend up [22, 23]². This peculiar band alignment in InAs forms a triangular quantum well (QW) at the interface leading to a quantization of the electron states along the z axis (see e.g. [26]). For typical high quality InAs crystals only one or two of these states are occupied, depending on mate-

² Despite a considerable amount of research, the exact nature of these surface states is to date not fully understood [24, 25].

rial details influencing the precise position of the Fermi level [22]. This yields a conducting sheet of electrons at the surface: a two-dimensional electron gas (2DEG). Despite being fundamental in the development of semiconductor systems, such surface accumulation layer 2DEGs suffer from low mobilities owing the proximity of the electrons to the surface, thus prone to interface scattering [27, 28]. We next introduce quantum well heterostructures, where the band alignment can be engineered to form QWs within the crystal lattice. This opens up a larger flexibility in their design and significantly improves their transport properties.

1.2.2 Quantum well heterostructures

The III-V group of semiconductors contains twelve binary compounds with lattice constants ranging from 4.5 \AA to 6.5 \AA and band gaps in the range $0.25 \text{ eV} \leq E_g \leq 2.5 \text{ eV}$ [29]. Together with a rich set of ternary alloys and the relative ease of growing layered structures by molecular beam epitaxy [30–32], this enables a vast platform for band engineering QWs by *a priori* design.

The top inset of Figure 1.3c shows a schematic representation of a three layer semiconductor sandwich, chosen such that the band gap in the central segment (yellow) is considerably smaller than in the flanking barriers (blue). Such a scenario can for example be practically realized in AlSb/InAs/AlSb [33] or InGaAs/InAs/InGaAs [34] heterostructures (among many others). This semiconductor stack results in the band alignment shown by the solid black line, confining electrons along the growth direction z in a rectangular QW of width w .

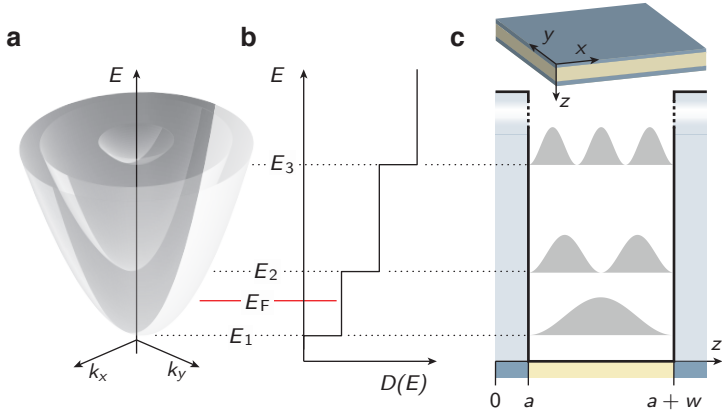


Figure 1.3: **Rectangular QW heterostructure** (a) Parabolic dispersion for the first three energy states confined to a 2D plane. (b) Density of states $D(E)$ as a function of energy. (c) Electric potential as a function of depth z from the surface. In gray the probability amplitudes of the first three levels are shown. The inset shows a three dimensional representation of the semiconductor sandwich structure.

For sufficiently high barriers, this situation resembles the toy model found in any quantum mechanics text book, the one dimensional infinite potential well (or a “particle in a box”). For finite height barriers, the results are similar with minor quantitative differences as the wave functions penetrate into the barriers. Whilst we neglect this effect for now, this will become important in Chapter 4. Concentrating on the infinite well, the energy levels are given by

$$E_n^z = \frac{\hbar^2}{2m^*} \left(\frac{n\pi}{w} \right)^2 \quad \text{with} \quad n = 1, 2, \dots \quad (1.1)$$

with \hbar the reduced Planck constant, m^* the effective mass, n the band index, and w the well width. The corresponding wavefunctions are given by

$$\psi_n(z) = A_n \sin\left(\frac{n\pi(z-a)}{w}\right) \quad (1.2)$$

defined in the range $a < z < a + w$ and zero elsewhere. A_n is a normalization constant. The corresponding probability densities $|\psi_n|^2$ are shown in [Figure 1.3\(c\)](#) for the first three levels ($n = 1, 2, 3$).

Whilst the electron motion in z direction is confined to this set of states, movement along the x - y plane is unrestricted. The total energy of an electron inhabiting this plane can then be written as the sum of the confinement energy E_n^z and a kinetic energy term

$$E_n(k_x, k_y) = \frac{\hbar k^2}{2m^*} + E_n^z \quad (1.3)$$

Here $k = \sqrt{k_x^2 + k_y^2}$, while k_x and k_y denote the electron momenta along the x and y directions. This equation defines free electron-like, isotropic, and parabolic bands as shown in [Figure 1.3\(a\)](#). Owing to the confinement along z the zero-point energy is given by $E_n(0, 0) = E_n^z$.

The total density of states (DOS) of the 2DEG is shown in [Figure 1.3\(b\)](#) with an energy independent contribution from each band of

$$d_n(E) = \frac{m^*}{\pi\hbar} \quad (1.4)$$

assuming a two-fold degeneracy for spin. The total DOS is a sum over all occupied subbands $\mathcal{D} = \sum_n d_n$. In order to get a handle on an experimentally measurable quantity we note that the total electron density follows as [\[35\]](#)

$$n = \int_{E_F^z}^{\mu_c} dE \mathcal{D}(E) = \mathcal{D} \cdot (\mu_c - E_F^z) = \mathcal{D} \cdot E_F \quad (1.5)$$

where μ_c is the chemical potential. By considering characteristic momentum of states at the Fermi level

$$E_F = \frac{\hbar^2 k_F^2}{2m^*} \quad (1.6)$$

we arrive at k_F , the Fermi wavevector. Combination of [Equation 1.5](#) and [1.6](#) then gives us

$$k_F = \sqrt{2\pi n} \quad (1.7)$$

which can be experimentally determined (see [Section 1.2.3](#) below). Other quantities of interest such as the Fermi wavelength and velocity follow as $\lambda_F = k_F/2\pi$ and $v_F = \hbar k_F/m^*$ respectively.

One aspect so far undiscussed is the “cleanliness” of electron transport in the 2D plane. Typically this is parametrized by the electron mobility

$$\mu = \frac{|e|\tau}{m^*} \quad (1.8)$$

where τ is the mean time an electron travels between scattering events. The mean free path is then

$$l_e = \mu v_F = \frac{\hbar\mu}{e} \sqrt{2\pi n} \quad (1.9)$$

which describes the average distance an electron travels ballistically before encountering a scattering event. Whilst a number of different scattering mechanisms contribute to determining the overall mobility we here simply consider an average scattering time. The different contributions can be disentangled by careful measurements of the mobility as a function of temperature [[36](#)], a useful tool in 2DEG development.

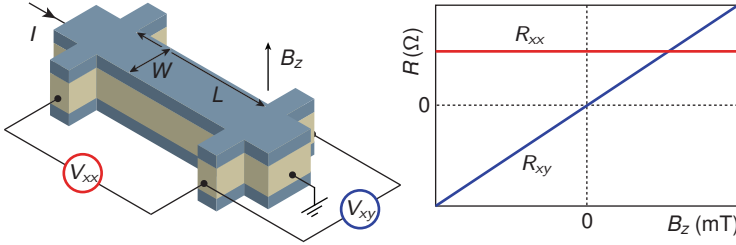


Figure 1.4: **Hall characterization.** A typical Hall bar geometry (left) with six ohmic contacts, two at either end acting as source and drain electrodes, and four along the mesa periphery used to measure the longitudinal and Hall voltages, V_{xx} (red) and V_{xy} (blue) respectively. The behavior of the corresponding resistances as a function of perpendicular magnetic field is shown on the right. In the low field regime the Hall resistance exhibits a finite slope from which the density can be deduced, whilst the longitudinal resistance remains constant.

1.2.3 Determining density and mobility

Now that we have determined the primary parameters of interest in the characterization of a 2DEG, we need to examine how to measure them. The measurement concept relies on the Drude model (see e.g. [35]), and is carried out by measuring the low magnetic field response of a Hall bar as shown in Figure 1.4(a). A constant current of magnitude I is driven from one end of the Hall bar to the other while a perpendicular magnetic field B_z is swept. Simultaneously, the longitudinal (V_{xx}) and Hall (V_{xy}) voltages are recorded. The per-square resistivity of the material can then be determined as

$$\rho_{xx} = \frac{V_{xx}}{I} \frac{W}{L} \quad (1.10)$$

which for low fields is constant (see [Figure 1.4\(b\)](#)). The Hall resistivity on the other hand increases linearly with field and is given by

$$\rho_{xy} = \frac{V_{xy}}{I} \quad (1.11)$$

From these quantities, measured over a small magnetic field range, the density and mobility can be extracted [35]

$$n = \frac{1}{|e|d\rho_{xy}/dB|_{B=0}}, \quad \mu = \frac{d\rho_{xy}/dB|_{B=0}}{\rho_{xx}(B=0)} \quad (1.12)$$

This type of characterization is key to benchmarking 2DEGs and will be used extensively throughout the thesis. Typically we will quote the resulting parameters, though more detailed results will be presented when we move to more novel materials. One key point to note is that the quantities extracted using this method represent the total density and mean mobility of all carriers contributing to transport. As such, further steps need to be taken to ensure that only a single subband is occupied in the QW. This point will be elaborated in [Chapter 5](#).

1.2.4 *Spin-orbit interaction*

So far we have implicitly assumed that the dispersion shown in [Figure 1.3\(a\)](#) tells the whole story. Realistic systems can however deviate in a number of ways from this two-fold spin degenerate, isotropic, and parabolic dispersion relation. One of the most interesting is through spin-orbit interaction (SOI). First discovered in the context of atomic and molecular physics as a relativistic correction coupling an electron's spin to its orbital momentum [37, 38], an analogous effect appears in condensed matter systems.

Owing to the additional complexity of solid-state systems where both crystal structure and interfaces play an important role, this

effect can manifest itself in two distinct forms termed structural inversion asymmetry (SIA) and bulk inversion asymmetry (BIA). These symmetry breaking mechanisms result in the Rashba and Dresselhaus spin-orbit terms respectively.

Rashba SOI relies on a structural symmetry breaking perpendicular to the 2DEG plane, typically provided by the confining potential. Hence the overall magnitude of this effect is given by $\alpha = \alpha_0 \langle \mathbf{E} \cdot \hat{\mathbf{z}} \rangle$ with a material dependent prefactor α_0 called the Rashba coefficient and $\mathbf{E} \cdot \hat{\mathbf{z}}$ the symmetry breaking electric field.

Dresselhaus spin-orbit on the other hand requires a crystal structure which breaks inversion symmetry (such as e.g. zinc blende). In this case the overall strength is determined by $\beta = \beta_0 \langle k_z^2 \rangle$ where β_0 is again a material dependent prefactor, the Dresselhaus coefficient, and $\langle k_z^2 \rangle \sim \pi^2/w^2$ is the squared average momentum in the z direction, dependent only on the QW width w [39].

The overall magnitude of both these effects is set by material parameters α_0 and β_0 , which derive from the atomic spin-orbit strength of the constituent atoms. Consequently crystals composed of heavier elements tend to have stronger spin-orbit coupling. The band gap also plays a fundamental role as the interaction between the valence and conduction bands drives this phenomenon. As a result, $(\alpha_0, \beta_0) \propto 1/E_g$ [40]. For more details the interested reader is directed at the comprehensive treatise on this topic by R. Winkler [41].

Understanding the origin of these effects we can now write the effective first order Hamiltonians for Rashba and Dresselhaus SOI respectively³

$$H_R = \frac{\alpha}{\hbar} (\sigma_x p_y - \sigma_y p_x) \quad (1.13)$$

$$H_D = \frac{\beta}{\hbar} (\sigma_x p_x - \sigma_y p_y) \quad (1.14)$$

³ Assuming a (001) grown QW

The total spin-orbit Hamiltonian is the sum of these two contributions $H_{\text{SO}} = H_{\text{R}} + H_{\text{D}}$.

Concentrating now on Rashba SOI, typically dominant in III-V materials, the dispersion relation follows from Equation 1.13 and is given by

$$E_{\pm}(\mathbf{k}) = \frac{\hbar^2 k^2}{2m} \pm \alpha k \quad (1.15)$$

and shown in Figure 1.5(a), with $k = \sqrt{k_x^2 + k_y^2}$. Owing to the form of the Hamiltonian, the spins always point in-plane and are tied to the electron momentum as demonstrated by the spin textures of the upper and lower spin-orbit bands shown in Figure 1.5(b) and (c) respectively. For each band the spin texture takes on the form of a vortex with the spin pointing perpendicular to the electron motion.

Due to time reversal symmetry however all states come in Kramers pairs of the form

$$E_{\uparrow}(\mathbf{k}) = E_{\downarrow}(-\mathbf{k}) \quad (1.16)$$

such that at zero magnetic field, details of the spin-orbit bandstructure do not contribute to transport. In order to examine this further we need to consider the effect of a magnetic field in the presence of Rashba SOI.

1.2.5 Competition between Zeeman and SOI

Applying a magnetic field induces an energy gap between spins of opposite orientation. Neglecting orbital effects, this can be described using the Zeeman Hamiltonian

$$H_{\text{Z}} = \frac{1}{2} g^* \mu_{\text{B}} (\mathbf{B} \cdot \boldsymbol{\sigma}) \quad (1.17)$$

where g^* is the Landé g -factor (assumed to be isotropic), \mathbf{B} the applied field, and $\boldsymbol{\sigma} = \{\sigma_x, \sigma_y, \sigma_z\}$ are the Pauli matrices. Assuming a magnetic field $\mathbf{B} \parallel \hat{\mathbf{x}}$ and negligible Dresselhaus SOI, the Hamiltonian then takes the form

$$H = H_0 + \frac{\alpha}{\hbar}(\sigma_x k_y - \sigma_y k_x) + \frac{g^* \mu_B B}{2} \sigma_x \quad (1.18)$$

in which we can identify the Zeeman energy $\epsilon_z = g^* \mu_B B/2$. The eigenvalues now take the form (see e.g. [42])

$$E_{\pm} = \frac{\hbar^2 k^2}{2m} \pm \sqrt{\alpha^2 k_x^2 + (\alpha k_y - \epsilon_z)^2} \quad (1.19)$$

Considering the case of transport purely along k_x or k_y yields

$$E_{\pm}(k_x = 0, k_y) = \frac{\hbar^2 k^2}{2m} \pm (\alpha k_y - \epsilon_z) \quad (1.20)$$

$$E_{\pm}(k_x, k_y = 0) = \frac{\hbar^2 k^2}{2m} \pm \sqrt{\alpha^2 k_x^2 \pm \epsilon_z^2} \quad (1.21)$$

where we can clearly identify that for $\mathbf{k} \perp \mathbf{B}$ a trivial extra energy shift ϵ_z appears, linearly shifting the bands as a function of magnetic field as shown in [Figure 1.5\(e\)](#). Conversely for $\mathbf{k} \parallel \mathbf{B}$, a nontrivial band mixing opens a finite energy gap at $\mathbf{k} = 0$ as shown in [Figure 1.5e](#). Nonetheless, for 2DEGs this gap is effectively quenched by the gapless dispersion along k_y . We will return to this so-called “spin-orbit gap” in [Section 1.5.2](#) in the context of confined one-dimensional structures with induced superconductivity.

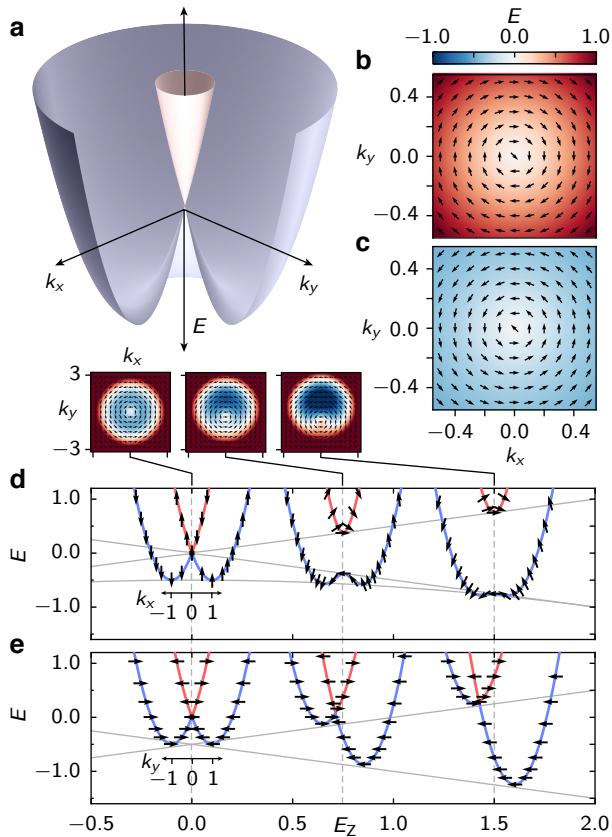


Figure 1.5: **Rashba SOI.** (a) 2DEG dispersion of the lowest band in the presence of finite Rashba SOI. For zero magnetic field the spin textures of the inner and outer bands are shown in (b) and (c) respectively. For transport along k_x (d) and k_y (e), positions of the band turning points (gray) are shown as a function of magnetic field $B \parallel k_x$ (in Zeeman units E_Z). For three magnetic fields, the corresponding full dispersions are shown with the superimposed spin orientation.

1.2.6 Quantum point contact

Now that we have a firm understanding of extended 2DEGs, the next step is to consider how they can be controlled to form arbitrarily shaped structures (such as one-dimensional wires if we want to investigate the aforementioned “spin-orbit gap”). The key aspect of semiconductors which has driven their technological prevalence is their ability to act as a voltage controlled switch. Similarly, by applying an external electric field, typically using electrodes on the sample surface (often called electrostatic gates) the density in the 2DEG can be locally tuned. This allows for the formation of complex devices with relative ease as nanometer-scale gate designs can be deposited in a single step without the need for troublesome etching of fine semiconductor features.

To introduce gating we will briefly review the “quantum point contact” (QPC) which represents the elementary unit in more complex designs. By depositing two metallic electrodes on the surface of a 2DEG as shown in [Figure 1.6\(a\)](#) and applying a gate voltage V_G , a one dimensional channel can be formed as the carriers below the gates are depleted. The red shading in the figure depicts a representation of the local electron density. We follow the results of Buttiker to examine the behavior in this 1D segment [\[43\]](#).

The potential in the central region (dashed box) between the gates takes the form of a saddle point ([Figure 1.6\(a\)](#) top inset)

$$V(x, y, z) = \frac{m^*}{2}(\omega_x^2 x^2 + \omega_y^2 y^2) + V(z) \quad (1.22)$$

where $V(z)$ is the confinement potential of the 2DEG and $\omega_{x/y}$ are characteristic frequencies in the x/y directions. The Hamiltonian is separable, and the total energy can thus be written as $E = E_x + E_y + E_z$. Along y the potential is that of a harmonic oscillator $E_y^n = \hbar\omega_y(n + 1/2)$ with $n = 1, 2, 3, \dots$ ([Figure 1.6\(a\)](#) bottom inset). Classically, only levels E_y^n up to the Fermi energy con-

tribute to transport. Quantum mechanically however, electrons can tunnel through the barrier with a transmission probability $\mathcal{T}_n(E)$. This problem of scattering from a saddle point potential has been solved analytically in the context of atomic and molecular physics and the transmission coefficients take the form [44, 45]

$$\mathcal{T}_n(E) = \frac{1}{1 + \exp(-2\pi\epsilon_n)} \quad (1.23)$$

with the energy parametrization

$$\epsilon_n = \frac{E - \hbar\omega_y(n + 1/2) - E_z}{\hbar\omega_x} \quad (1.24)$$

The conductance through the constriction can then be calculated as the sum of transmission coefficients at E_F

$$G = \frac{2e^2}{h} \sum_n \mathcal{T}_n(E_F) \quad (1.25)$$

with the conductance quantum $G_0 = 2e^2/h$, for a two-fold spin degenerate subband. In the presence of finite Zeeman splitting this degeneracy is broken and the conductance rises in steps of e^2/h [46].

For zero magnetic field, the theoretical conductance as a function of Fermi energy is shown in Figure 1.6(b) for two different curvatures of the saddle point potential $\omega_y/\omega_x = 1$ (dashed) and $\omega_y/\omega_x = 2$ (solid). Such conductance quantization was first experimentally observed in 1988 jump starting the rich field of mesoscopic transport [7, 47], owing largely to the versatility of the gateable 2DEG platform.

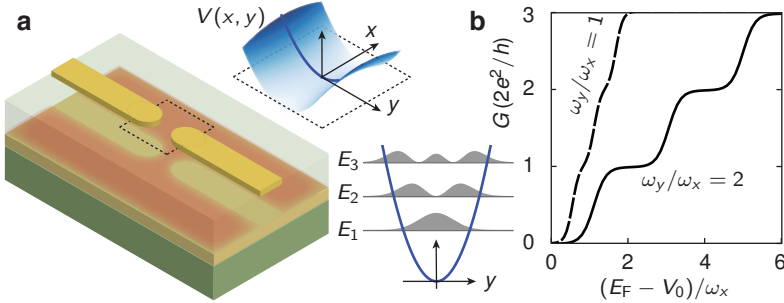


Figure 1.6: **Quantum point contact.** (a) Schematic of a metallic split-gate deposited on the surface of buried 2DEG. By applying a negative potential to the gates the 2DEG underneath is depleted, indicated by the red shading representing local electron density. The local potential in the constriction takes the form of a saddle (top inset). Along y the potential resembles the harmonic oscillator with constantly spaced energy levels as shown in (bottom inset), with the corresponding wavefunction amplitudes shown in gray. (b) The calculated conductance through the constriction in units of the conductance quantum $2e^2/h$. Results are shown for two constrictions of different curvatures $\omega_y/\omega_x = 1$ (dotted) and $\omega_y/\omega_x = 2$ (solid).

1.2.7 Choice of material system

So far we have kept things general, concentrating on the key ideas required for understanding the behavior of 2DEGs with electrostatic gate control. We have briefly addressed differences with respect to how the band structure behaves at the surfaces of two different III-V materials, namely InAs and GaAs. In this section we give an overview of the three III-V binary semiconductors GaAs, InAs and InSb available for electron transport experiments and compare their characteristics.

Before diving in it is instructive to consider the desired characteristics. In terms of the 2DEG we want a high mobility, stable gating, large g -factor, and strong SOI. The reasoning for wanting strong SOI will be examined in detail towards the end of this section.

From a practical perspective the ability to fabricate devices is also of utmost importance. Whilst one might expect that the differences between III-V materials are negligible, this is far from true. Simply from an energetics perspective, InSb is a relatively unstable material compared to GaAs and is as such prone to crystal defects but also to forming unwanted oxides when exposed to the atmosphere. As a result it is especially unstable at the elevated temperatures $\sim 180^\circ\text{C}$ typical in processing.

Finally, we would like the material to be compatible with inducing superconductivity. This characteristic somewhat poorly understood but is typically related to tendency of the bands to bend up or down at the surface. If well behaved Ohmic contacts can be formed, inducing superconductivity should in theory be straightforward. In the case of depletion layers forming a Schottky barrier at the surface, substantial efforts are required to pull this down.

Over the course of this work, measurements have been carried out on QPCs in all three material systems. Results are shown in [Figure 1.7\(b\)](#), plotted on an arbitrary gate voltage scale to allow for a cleaner comparison. All three materials show a similar trend of quantized conductance plateaus at integer values of $G_0 = 2e^2/h$ (c.f. [Figure 1.6](#)). The quality of the data however is distinctly different, with the GaAs devices showing negligible signs of disorder, compared to the somewhat more disordered InAs, and almost questionable InSb. Indeed, the InSb sample whilst seemingly showing a plateau at $2e^2/h$ for certain gate sweeps, was very unstable in time. The two sweeps shown in the figure reflect two consecutive gate traces (both swept down), clearly indicating gate instability.

Motivated by these traces, in [Figure 1.7a](#) we show a radar plot scoring each of the materials in the aforementioned categories to

give and overview of their respective advantages and disadvantages. As some of the figures of merit are hard to objectively quantify, the categories *Fabrication*, *Gating*, and *Induced Superconductivity* are scored largely on intuition based on the state of the literature and experiences in the lab. The values of the other figures of merit are given in the table of [Figure 1.7](#), with densities and mobilities reported for the measured materials together with the current records (at the time of writing). The g-factors and Rashba coefficients are quoted from literature for bulk crystals.

It is clear from [Figure 1.7](#) that all three materials have their own areas of strength. Largely the dominance of GaAs in mobility, fabrication, and gating is due to nearly 40 years of active research and development. InAs and InSb on the other hand while relatively widely studied in the context of photon detection (though much of it classified) have only relatively recently been investigated in 2DEG experiments. As a result, further material developments may well significantly improve these characteristics.

As large SOI and g-factors are paramount to studying the potential topological states which will be introduced in [Section 1.5.2](#), in this work we have concentrated primarily on InAs. Very early in this work InSb was tested but eventually abandoned due to countless issues with material stability during fabrication.

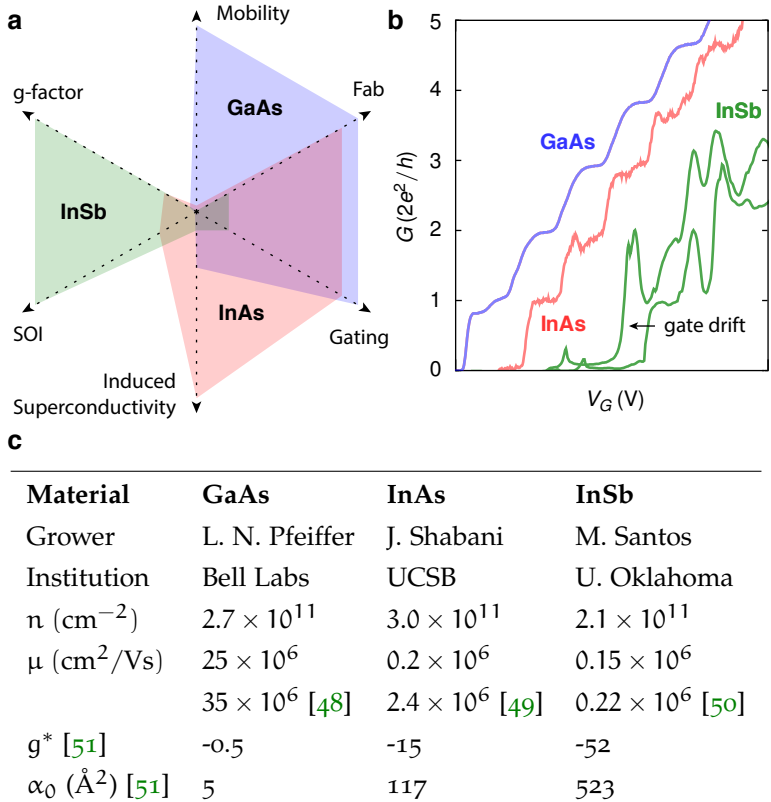


Figure 1.7: **III-V material comparison.** (a) Radar chart scoring GaAs (blue), InAs (red), and InSb (green) in six figures of merit. (b) Conductance as a function of gate voltage measured on QPCs in each material system. (c) Figures of merit for the three materials and collaborating materials growers/institutions.

1.3 SUPERCONDUCTIVITY

In a seminal work in 1957, Bardeen, Cooper, and Schrieffer (BCS) developed a microscopic description of superconductivity [52]. The key idea was that electrons with opposite momentum and spin could pair up to form an effective bosonic particle called the Cooper pair ($\mathbf{k} \uparrow, -\mathbf{k} \downarrow$), with the attractive potential driving this process mediated by weak electron-phonon coupling. Owing to this pairing, Cooper pairs condense into an energetically favorable ground state separated from the continuum of single-electron states by an energy gap Δ . Quasiparticle excitations from the BCS condensate can be conveniently described by the Bogoliubov-de Gennes (BdG) equation [53, 54]

$$\begin{bmatrix} H(\mathbf{r}) & \Delta(\mathbf{r}) \\ \Delta^*(\mathbf{r}) & -H(\mathbf{r}) \end{bmatrix} \begin{pmatrix} u_{\mathbf{k}}(\mathbf{r}) \\ v_{\mathbf{k}}(\mathbf{r}) \end{pmatrix} = E \begin{pmatrix} u_{\mathbf{k}}(\mathbf{r}) \\ v_{\mathbf{k}}(\mathbf{r}) \end{pmatrix} \quad (1.26)$$

with the single electron Hamiltonian $H(\mathbf{r})$ defined as

$$H(\mathbf{r}) = -\frac{\hbar^2}{2m^*} \nabla^2 + U(\mathbf{r}) - \mu_c \quad (1.27)$$

where m^* is the effective mass, $U(\mathbf{r})$ a scalar potential, and μ_c the chemical potential. The solutions of this equation of the form $(u_{\mathbf{k}}, v_{\mathbf{k}})^T$ represent electron or hole-like quasiparticle excitations. The vector components individually represent the probability of finding a quasiparticle in a electron or hole-like state.

For a homogeneous superconductor $\Delta(\mathbf{r}) = \Delta$ the spatial dependence can be separated out. Assuming plane wave solutions of the form

$$\begin{pmatrix} u_{\mathbf{k}}(\mathbf{r}) \\ v_{\mathbf{k}}(\mathbf{r}) \end{pmatrix} = \exp(i\mathbf{k} \cdot \mathbf{r}) \begin{pmatrix} u_0 \\ v_0 \end{pmatrix} \quad (1.28)$$

the electron and hole weights u_0 and v_0 are thus

$$u_0^2 = \frac{1}{2} \left(1 + \frac{\sqrt{E^2 - \Delta_0^2}}{E} \right), \quad v_0^2 = 1 - u_0^2 \quad (1.29)$$

with the energy eigenvalues given by

$$E = \pm \sqrt{\xi_k^2 + |\Delta_0|^2} \quad \text{where} \quad \xi_k = \frac{\hbar^2 k^2}{2m^*} - \mu_c \quad (1.30)$$

The density of states then takes the form

$$\rho_S(E) = \begin{cases} \frac{E}{\sqrt{E^2 - \Delta^2}} & E > \Delta \\ 0 & E < \Delta \end{cases} \quad (1.31)$$

shown in [Figure 1.8](#).

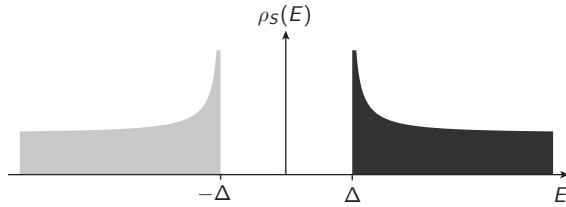


Figure 1.8: Superconducting density of states

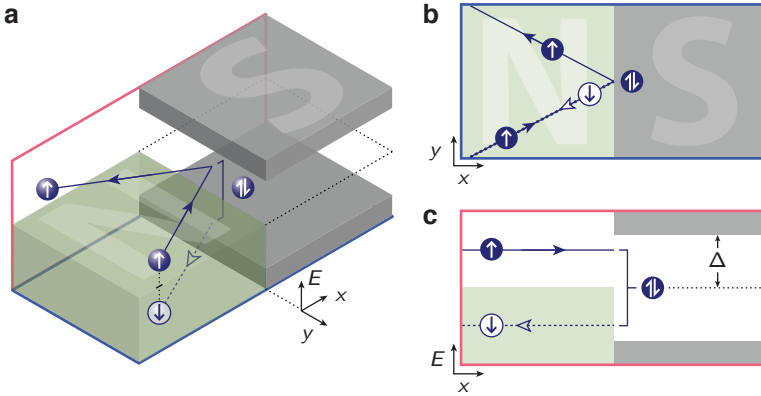


Figure 1.9: **Andreev reflection.** (a) Schematic representation of Andreev reflection at a normal metal-superconductor interface. To capture the key ingredients we assume transport is confined to the two-dimensional xy plane. The third dimension is energy, with the filled regions indicating a finite density of single particle states. In the normal region (green), states are available up to the Fermi level E_F , fixed to $E = 0$ in the center of the superconducting gap. (b) A cut of (a) in the spatial plane showing the two possible reflection processes. Normal reflection leads to an incoming $(\mathbf{k}_e \uparrow)$ electron bouncing off the interface yielding a returning $(-\mathbf{k}_e \uparrow)$ electron. Andreev reflection on the other hand dumps a $(\mathbf{k}_e \uparrow, -\mathbf{k}_e \downarrow)$ Cooper pair into the superconductor, yielding a retroreflected $(\mathbf{k}_h \downarrow)$ hole exactly retracing the path of the incident electron. (c) A cut of (b) in the energy/space plane depicting the Andreev reflection process. The incoming electron with energy ϵ is reflected as a hole with energy $-\epsilon$.

1.4 HYBRID STRUCTURES

1.4.1 *Andreev reflection*

Consider now the case of a semiconductor-superconductor (NS) interface as shown in [Figure 1.9\(a\)](#). As the coupling may not be perfect we include an intervening barrier at the interface $H\delta(x)$, with H the barrier height. In the semiconductor, all states below the Fermi level are occupied as indicated by the green shading. The superconductor on hand has a finite energy gap, with no single particle states available within $\pm\Delta$ of the Fermi level ([Figure 1.9\(c\)](#)).

Assuming an incident spin-up electron arriving from the N region described by a wavefunction Ψ_{in} ([Equation 1.32a](#)), upon hitting the interface two processes are possible dependent on both the energy of the incoming electron, and the opacity of the barrier. For energies $E < \Delta$ transmission into the superconductor (in a single-particle sense) is prohibited and as such the electron must undergo a reflection process yielding $\Psi_{\text{reflection}}$ ([Equation 1.32b](#)). For a transparent barrier the electron can be Andreev retro-reflected as a hole, creating a Cooper pair in the superconducting condensate with a total charge transfer of $2e$ as shown in [Figure 1.9](#). The presence of the barrier however also allows for a normal specular reflection off the interface resulting in an effective charge transfer of $-e$. For energies $E > \Delta$ the electron may be injected into the superconductor

as electron or hole-like quasi-particle excitations described by the wavefunction $\Psi_{\text{transmission}}$ (Equation 1.32c).

$$\Psi_{\text{in}} = \boxed{\begin{pmatrix} 1 \\ 0 \end{pmatrix} e^{ik_e x}} \quad (1.32a)$$

Incident electron

$$\Psi_{\text{reflection}} = \boxed{a \begin{pmatrix} 0 \\ 1 \end{pmatrix} e^{ik_h x}} + \boxed{b \begin{pmatrix} 1 \\ 0 \end{pmatrix} e^{-ik_e x}} \quad (1.32b)$$

Andreev Normal

$$\Psi_{\text{transmission}} = \boxed{c \begin{pmatrix} u \\ v \end{pmatrix} e^{i\tilde{k}_e x}} + \boxed{d \begin{pmatrix} u \\ v \end{pmatrix} e^{-i\tilde{k}_h x}} \quad (1.32c)$$

Electron-like Hole-like

The corresponding probabilities of Andreev and normal reflection are given by $A = a^*a$ and $B = b^*b$ respectively, and for energies above the gap, probabilities of quasi-particle transmission by $C = c^*c$ and $D = d^*d$. The solution of this set of equations under probability conservation, $A(E) + B(E) + C(E) + D(E) = 1$, yields the probabilities of each process as tabulated in Table 1 and shown in Figure 1.10, with $\gamma^2 = [u_0^2 + Z^2(u_0^2 - v_0^2)]^2$ while u_0^2 and v_0^2 are defined by Equation 1.29 [55]. Here Z represents the dimensionless barrier strength, determined by the magnitude H of the barrier and is also directly related to the transmission probability \mathcal{T}

$$Z = H/\hbar v_F = \sqrt{\frac{1}{\mathcal{T}} - 1} \quad (1.33)$$

The current through the junction can be evaluated by considering the integral

$$I_{\text{NS}}(V) = \frac{G_{\text{N}}}{e} \int_{-\infty}^{\infty} dE [f_{\rightarrow}(E) - f_{\leftarrow}(E)] \quad (1.34)$$

	$E < \Delta$	$E > \Delta$
A	$\frac{\Delta^2}{E^2 + (\Delta^2 - E^2)(1 + 2Z^2)^2}$	$\frac{u_0^2 v_0^2}{\gamma^2}$
B	$1 - A$	$\frac{(u_0^2 - v_0^2)^2 Z^2 (1 + Z^2)}{\gamma^2}$
C	0	$\frac{u_0^2 (u_0^2 - v_0^2) (1 + Z^2)}{\gamma^2}$
D	0	$\frac{v_0^2 (u_0^2 - v_0^2) Z^2}{\gamma^2}$

Table 1: Transmission and reflection coefficients at an NS interface with transparency Z and superconducting gap Δ . A gives the probability of Andreev reflection and B of normal reflection. C and D give the probabilities of transmission into the superconductor as electron or hole-like quasiparticles respectively. For energies below the gap these processes are forbidden.

with the right moving distribution function originating from the semiconductor side given by

$$f_{\rightarrow}(E) = f_0(E - eV) \quad (1.35)$$

with f_0 the Fermi distribution function. The distribution function originating from the superconducting bank is

$$f_{\leftarrow}(E) = A(E)[1 - f_{\rightarrow}(-E)] + B(E)f_{\rightarrow}(E) + [C(E) + D(E)]f_0(E) \quad (1.36)$$

Noting that $A(E) = A(-E)$ and $f_0(-E) = 1 - f_0(E)$, Equation 1.34 can then be written as

$$I_{NS}(V) = \frac{G_N}{e} \int_{-\infty}^{\infty} dE [f(E) - f(E - eV)] (1 + A(E) - B(E)) \quad (1.37)$$

Here we identify the expression $1 + A(E) - B(E)$ as the “transmission coefficient for electrical current” [55]. Appreciating that the quantities of interest for transport are the Andreev and normal reflection coefficients A and B , in Figure 1.10 we study their dependence on both energy and the interface transparency Z .

Following from Equation 1.37, $dI/dV = G(eV) \propto 1 + A(eV) - B(eV)$. The right hand panel of Figure 1.10 thus shows the differential conductance normalized by the normal state conductance⁴ $G_{NN} \propto (1 + Z^2)^{-1} = \mathcal{T}$. We note here that in this simple picture the normal state conductance is equivalent to the conductance at large bias $G_{NN} = G(eV \gg \Delta)$. The colorscale is centered on $G(eV)/G_{NN} = 1$ in white, to highlight regions of conductance enhancement (red) and suppression (blue). For $Z < 1$ a conductance enhancement is observed for $|eV| \leq \Delta$, approaching a factor of two for $Z \ll 1$. For $Z = 0.1$ the enhancement is ~ 1.95 . In the opposite limit, for an opaque interface $Z > 1$ a significant suppression of the conductance is observed within the gap. In this limit the conductance is proportional to the density of states in the superconductor $G(eV) \propto \rho_S(eV)$ (cf. Equation 1.31). Indeed this somewhat surprising result is the key to the final chapters of the thesis. By controllably forming an opaque NS interface, the junction allows us to probe the local density of states in at the interface by tunneling spectroscopy.

⁴ Whilst this is quite intuitive, it can be derived from Equation 1.37 by considering the limit $A \rightarrow 0$. Probability conservation then implies $1 - B = C = (1 + Z^2)^{-1}$.

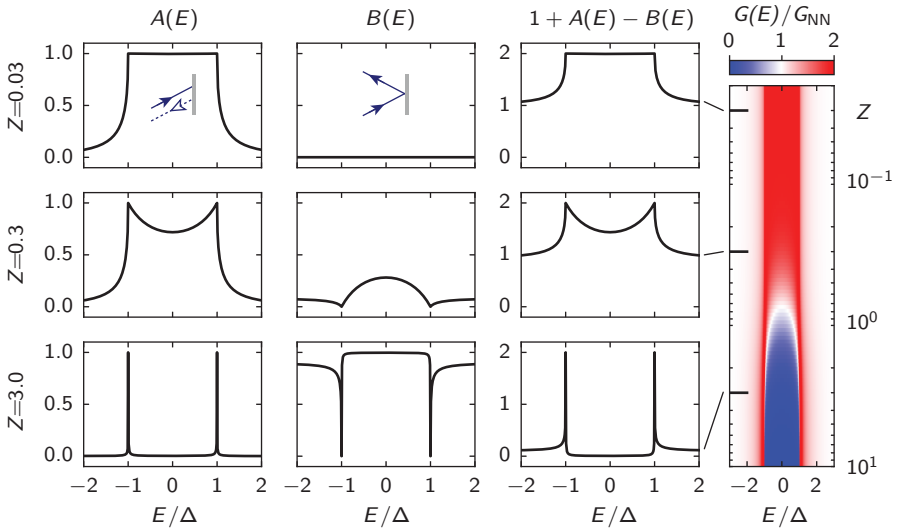


Figure 1.10: **BTK coefficients as a function of barrier transparency.** The probability of Andreev reflection $A(E)$ (left column), normal reflection $B(E)$ (middle column), and the “transmission coefficient for electrical current” [55] $1 + A(E) - B(E)$ (right column), shown for three different values of the interface transparency $Z = \{0.03, 0.3, 3.0\}$ in the top, middle, and bottom rows respectively. The rightmost panel shows the ratio $G(E)/G_{NN}$ as a function of Z . The colorscale is saturated at 2 to emphasize the in-gap conductance doubling for $Z < 1$. For $Z > 1$ the BCS coherence peaks at the gap edge may yield a ratio $G(E)/G_{NN}$ significantly larger than 2.

1.4.2 *The Josephson junction*

In 1962 Josephson proposed that a supercurrent could flow between two disconnected superconducting leads, with its magnitude proportional to the phase difference between them $\phi = \chi_1 - \chi_2$ [10]:

$$I_S(\phi) = I_C \sin(\phi) \quad (1.38)$$

Generically however this current phase relation may include higher order components

$$I_S(\phi) = \sum_{n \geq 1} [I_n \sin(n\phi) + J_n \cos(n\phi)] \quad (1.39)$$

with the odd J_n terms vanishing in the presence of time-reversal symmetry. In this thesis we will largely assume a sinusoidal CPR, however noting that recent evidence on epitaxial superconductor-semiconductor nanowires suggests the presence of substantial higher order components as expected for transparent junctions [56].

1.4.3 *Andreev bound states to a supercurrent*

To examine the behavior of a SNS structure it is instructive consider two SN junctions in series. In this case however we need to explicitly consider right (Ψ_{\rightarrow}) and left (Ψ_{\leftarrow}) moving wavefunctions

separately [57]. These can be compactly be written together in the form

$$\Psi_\tau = \begin{cases} A_\tau \begin{pmatrix} v_0 e^{-i\phi/2} \\ u_0 \end{pmatrix} e^{i\tau \tilde{k}_{(-\tau)} x} & x < 0 \\ B_\tau \begin{pmatrix} v_0 e^{-i\phi/2} \\ 0 \end{pmatrix} e^{i\tau k_e x} + B_\tau \begin{pmatrix} 0 \\ u_0 \end{pmatrix} e^{i\tau k_h x} & 0 < x < L \\ C_\tau \begin{pmatrix} v_0 e^{+i\phi/2} \\ u_0 \end{pmatrix} e^{i\tau \tilde{k}_{(\tau)}(x-L)} & x > L \end{cases} \quad (1.40)$$

with $\tau = \pm 1$ corresponding to Ψ_\rightarrow and Ψ_\leftarrow respectively. $\tilde{k}_{(\tau)}$ denote the wavevectors for electrons ($\tau = 1$) and holes ($\tau = -1$) in the superconducting banks, and k the wavevectors in the normal region. Given some work, this system of equations can be shown to yield Andreev bound states for an SNS junction of length L with perfect transmission

$$\left(\frac{E}{\Delta}\right) \left(\frac{L}{\xi}\right) = 2 \arccos\left(\frac{E}{\Delta}\right) \pm \phi - 2\pi n \quad (1.41)$$

For short junctions in the limit $L \ll \xi$, the left hand side tends to zero such that

$$E^\pm(\phi) = \pm \Delta \cos\left(\frac{\phi}{2}\right) \quad (1.42)$$

In the case of finite barriers at the interfaces the calculation is somewhat more involved but can be solved in a similar fashion yielding

$$E^\pm(\phi) = \pm \Delta \sqrt{\frac{\cos^2(\phi/2) + 4Z^2}{4Z^2 + 1}} \quad (1.43)$$

1.4.3.1 Supercurrent

As these bound states allow for a dissipationless transfer of charge across the normal region, a supercurrent flows. The total supercurrent carried by these discrete states is given by

$$I = \sum_{n,\pm} \frac{2e}{\hbar} \frac{dE_n^\pm(\phi)}{d\phi} f[E_n^\pm(\phi)] \quad (1.44)$$

Plugging Equation 1.43 into Equation 1.44 yields

$$I(\phi) = \frac{e\Delta_0}{\hbar} \frac{\sin(\phi)}{2\sqrt{(4Z^2+1)(\cos^2(\phi/2)+4Z^2)}} \tanh(E_B^+/2k_B T) \quad (1.45)$$

$$= \frac{e\Delta}{2\hbar} \mathcal{T} \left(\frac{\sin(\phi)}{\sqrt{1-\mathcal{T}\sin^2(\phi/2)}} \right) \tanh \left(\frac{\Delta}{2k_B T} \sqrt{1-\mathcal{T}\sin^2(\phi/2)} \right) \quad (1.46)$$

Whilst this calculation was done explicitly for a clean junction with finite transparency barriers, equivalent results are obtained largely independent of the scattering mechanism, including arbitrary delta functions barriers [58–60], arbitrary smooth potentials [61], resonant impurity levels [62], or the presence of a single scattering impurity in the junction [63].

In the limit of perfect interfaces we obtain the form derived by Beenakker and Furusaki for a superconducting quantum point contact with N occupied channels [64, 65]

$$I(\phi) = \frac{Ne}{\hbar} \Delta_0 \sin(\phi/2) \tanh \left[\frac{\Delta_0}{2k_B T} \cos(\phi/2) \right] \quad (1.47)$$

Indeed in the classical (many mode) limit this reduces to the originally derived Kulik-Omelyanchuk (KO-2) model [66] and can be obtained from Equation 1.47 by division by the quantized resistance $R_N = \pi\hbar/Ne^2$.

1.4.4 *Fraunhofer pattern*

In the presence of a perpendicular magnetic field B_{\perp} as shown on the upper right of [Figure 1.11](#) the phase difference across a Josephson junction gains an extra term (c.f. [Equation 1.38](#))

$$\phi = \chi_2 - \chi_1 - \frac{2\pi}{\Phi_0} \oint_C \mathbf{A} \cdot d\mathbf{s} \quad (1.48)$$

where \mathbf{A} is the magnetic vector potential, related to the applied field by $\mathbf{B} = \nabla \times \mathbf{A}$, and $d\mathbf{s}$ is an infinitesimal surface element in the plane of the junction. Letting the integration contour C run the full width of the junction and deep into the contacts we see that the integral describes the total flux $\Phi = B_{\perp}(WL)$ enclosed by the junction area. This results in a constant winding of the phase along the contacts of the form

$$\frac{\partial \phi}{\partial y} = \frac{2\pi}{\Phi_0} B_{\perp} L \quad (1.49)$$

yielding a linear gradient

$$\phi(y) = \frac{2\pi}{\Phi_0} B_{\perp} L y + \phi_0 \quad (1.50)$$

where ϕ_0 is an integration constant enumerating the phase difference at $y = 0$. Letting $k_{\phi} = (2\pi/\Phi_0)B_{\perp}L$ we can now combine [Equation 1.38](#) and [1.50](#) to write the total supercurrent I_s as a function of applied magnetic field

$$I_s(B_{\perp}) = \int_{-W/2}^{W/2} J_c(y) \sin(k_{\phi}y + \phi_0) dy \quad (1.51)$$

here $J_c(y)$ is the supercurrent density along the junction width. Typically for well behaved junctions $J_c = \text{constant}$ as shown in the

upper inset of [Figure 1.11](#). As the phase offset ϕ_0 only contributes a phase factor to the integral [Equation 1.51](#) can be rewritten as

$$I_s^{\max}(B_{\perp}) = \left| \int_{-W/2}^{W/2} J_c(y) \exp(ik_{\phi}y) dy \right| \quad (1.52)$$

which we identify as the Fourier transform of the critical current density J_c .

For the case of J_c being constant this results in the well known *Fraunhofer diffraction pattern*

$$I_s^{\max}(\Phi) = I_c \left| \frac{\sin(x)}{x} \right| \quad \text{where} \quad x = \frac{\pi\Phi}{\Phi_0} \quad (1.53)$$

shown at the bottom of [Figure 1.11](#).

To gain insight into the physical origin of this effect, the local supercurrent density $J_s(y) = J_c(y) \sin(k_{\phi}y + \phi_0)$ is plotted for a range of different magnetic fields corresponding to fluxes of $\Phi = 0, 0.5, 1.0, 1.5\Phi_0$ threading the junction (assuming a current flow directed from bottom to top). For $\Phi = 0$, J_s is constant along the junction width leading to uniform current flow of magnitude I_c^0 . Upon increasing the field however, the k_{ϕ} term becomes important, leading to a sinusoidal oscillation of J_s with a period $\Delta y = 2\pi/k_{\phi}$. For $\Phi = \Phi_0/2$ half a wavelength is enclosed within the junction leading to negligible supercurrent transport near the junction edges, overall lowering the critical current magnitude. Further increasing the field to $\Phi = \Phi_0$, a full wavelength of the oscillation is enclosed in the junction such that half of the junction carries supercurrent parallel to the external current flow ($+J_s$), while the other half carries a backward propagating supercurrent anti-parallel to it. This scenario results in a net zero supercurrent forming the first node of the Fraunhofer pattern. As the field is increased further this scenario repeats, resulting in nodes whenever the enclosed flux equates to integer multiples of Φ_0 .

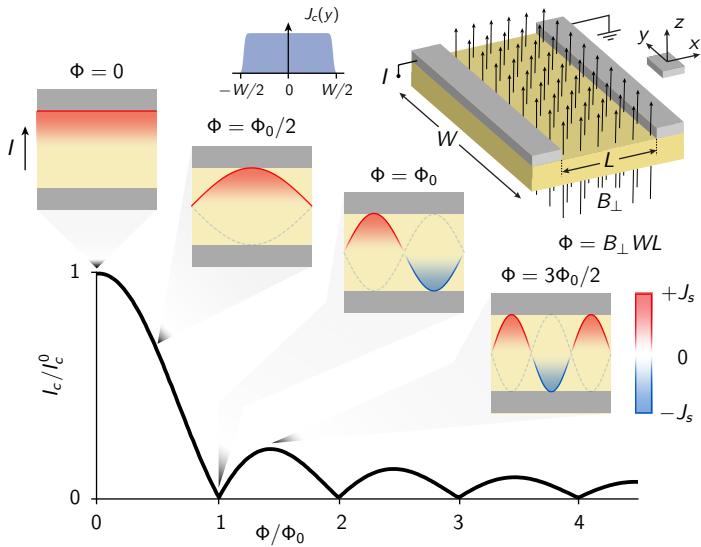


Figure 1.11: **Fraunhofer diffraction.** (Top right) SNS junction in an external perpendicular magnetic field B_{\perp} with a current I sourced from left to right. In the ideal case the critical current density along the junction width is constant as shown by the top inset. In this case the resulting diffraction pattern takes on the Fraunhofer form (bottom). The local supercurrent densities for a range flux quanta threading the junction are shown inset. Positive supercurrent flow (along I) is colored red, while negative flow (against I) is in blue.

1.5 TOPOLOGICAL HYBRIDS

1.5.1 Majorana fermions

Proposed by Ettore Majorana in 1937 as an overlooked solution to the Dirac equation, Majorana fermions are particles which acts as their own antiparticle [67]

$$\gamma = \gamma^\dagger \quad (1.54)$$

To date, no fermions included in the Standard Model have been shown to demonstrate this property, with experiments still underway on neutrinos. Condensed matter systems however often display rich phenomenna beyond those found in particle physics [68]. Indeed, half a century after Majorana's work, proposals appeared suggesting that such particles could emerge as excitations in a topological superconductor [69, 70]. Some more time was required to reformulate the proposals into actionable experiments, but in 2010 a recipe for creating such topological superconductors was published using off the shelf parts [71, 72].

1.5.2 A recipe

The proposed physical model combines ingredients typically found in a condensed matter physics laboratory, namely a quasi-one-dimensional semiconductor with SOI, Zeeman coupling and superconductivity. This system is described by the Hamiltonian

$$H = \int dy \Psi^\dagger \mathcal{H} \Psi \quad \text{where} \quad \Psi = (\psi_\uparrow, \psi_\downarrow, \psi_\downarrow^\dagger, -\psi_\uparrow^\dagger)^T \quad (1.55)$$

with

$$\mathcal{H} = \underbrace{\left[\frac{k_y^2}{2m^*} - \mu_c \right]}_{\text{Kinetic}} \tau_z + \underbrace{\frac{\alpha}{\hbar} k_y \sigma_x \tau_z}_{\text{SOI}} + \underbrace{\frac{g\mu_B}{2} B_y \sigma_y}_{\text{Zeeman}} + \underbrace{\Delta_0 \tau_x}_{\text{Sc.}} \quad (1.56)$$

Here the Pauli matrices σ and τ act on spin and particle-hole spaces respectively. Further m^* is the effective mass, μ_c the chemical potential, α the magnitude of Rashba SOI, \hbar the reduced Planck constant, g^* the g -factor, μ_B the Bohr magneton, B_y the magnetic field applied along the wire axis, and finally Δ the superconducting gap. Collecting terms for clarity such that $E_Z = g^* \mu_B B_y / 2$ and $\xi = (k_y^2 / 2m^*) - \mu_c$, the dispersion can be readily obtained

$$E_{\pm}^2(k_y) = E_Z^2 + \Delta_0^2 + \xi^2 + \left(\frac{\alpha}{\hbar} k_y\right)^2 \pm 2\sqrt{E_Z^2(\Delta_0^2 + \xi^2) + \left(\frac{\alpha}{\hbar} k_y\right)^2 \xi^2} \quad (1.57)$$

and is shown in [Figure 1.12\(a\)](#) for a range of magnetic fields (with $\mu_c = 0$, $\alpha = 1$ and $m^* = 1$, and Δ_0 assumed to be independent of applied magnetic field). The dispersion relations at each field are shaded according to their electron (red) and hole (blue) weights, obtained from the corresponding eigenvectors. Furthermore the spin textures are also shown, similarly to [Figure 1.5](#).

For $E_Z = 0$ a gap of magnitude Δ opens at E_F with the spectrum mirrored around $E = 0$ owing to the introduced superconducting pairing. As the magnetic field is increased the gap is suppressed linearly as $\Delta = 2(\Delta_0 - E_Z)$, with spin orientations at the gap edge at $k = 0$ fixed in an antiparallel configuration. For a critical magnetic field $E_Z = E_Z^* = \Delta$ the gap closes, reopening as $\Delta = 2(E_Z - \Delta_0)$ for $E_Z > \Delta_0$ with an inversion of the lower energy bands. In this regime the system has become topological, and by bulk-edge correspondence for a finite system we expect the appearance of a set of edge states connecting the inverted bands, resulting in the zero-energy Majorana bound state (MBS) indicated by the dashed line. This state is delocalized along the entire wire length, with exponentially suppressed wave function weight in the center. As such, the MBS is protected from local perturbations.

For the general case of a non-zero chemical potential the critical field is given by $E_Z^* = \sqrt{\Delta^2 + \mu_c^2}$ as shown in Figure 1.12(b). Whilst the topological gap opens at E_Z^* and initially grows linearly, deep in the topological regime the magnitude of the gap is governed by the strength of SOI. In Figure 1.12(c) the size of the lowest energy gap is shown for a range of spin orbit strengths $\alpha = \{0.5, 1.0, 1.5, 2.0\}$ denoted by $\{\bullet, \blacktriangle, \blacksquare, \star\}$ respectively. After some characteristic field value, dependent on α , the topological gap saturates when the $k = 0$ gap exceeds that at k_{SO} as seen in Figure 1.12(a). For large E_Z the gap is largely constant and determined by the magnitude of α . In Figure 1.12(d) the magnitude of the topological gap is shown for increasing α at a constant field magnitude of $E_Z/\Delta_0 = 3$. For weak spin-orbit $\Delta \propto \alpha$, whilst in the strong spin-orbit regime the gap is bounded by $\Delta \leq \Delta$.

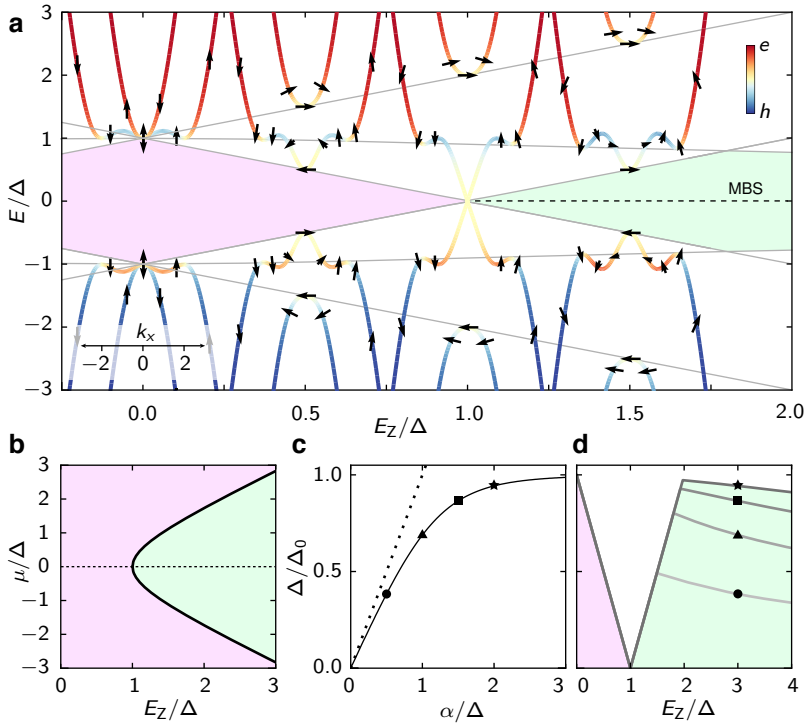


Figure 1.12: **Bandstructure of a one dimensional wire with SOI, superconductivity, and Zeeman coupling.** (a) Bandstructure of a one-dimensional wire as a function of Zeeman energy E_Z . The gray lines indicate the locations of the band local minima. Pink shading denotes a trivial gapped system while green indicate a topological gap. The dashed line signifies the zero-energy Majorana bound state in a finite length wire. (b) Phase diagram as a function of chemical potential and Zeeman energy. (d) Lowest energy gap in the system for four value of Rashba SOI strength indicated in (c). (c) Size of the topological gap for $E_Z = 3\Delta$ as a function of Rashba SOI strength.

Not even a year after Brian D. Josephson's seminal prediction [10, 11], Anderson and Rowell confirmed this effect in metal oxide junctions [73], jump-starting a novel field of superconducting electronics.

After a considerable amount of effort by numerous groups [74], some ten years after these advances on metallic structures, Huang and Van Duzer succeeded in fabricating semiconductor-superconductor Josephson junctions (Sm-S JJs) on silicon [75, 76]. Starting from this milestone, we briefly review the progress of hybrid semiconductor-superconductor structures over the past fifty years in Figure 2.1. In the interest of brevity and relevance to this thesis we highlight mainly papers concentrating on III-V materials. On the left hand side, a histogram of the number of papers published per year is shown, with those related to 2DEGs in blue.

Following the first Sm-S JJs it took another ten years before control by electrostatic gating was demonstrated, with simultaneous successes on both silicon [77] and InAs platforms [78]. Fraunhofer interference, first observed in metallic junctions in 1963 [79] and key to proving Josephson's predictions, was shortly after confirmed in InAs junctions [80]. Whilst most of the early work was carried out on single crystal inversion layers, heterostructured materials grown by molecular beam epitaxy soon followed. Initially this approach focused on improving the inversion layers [81], eventually superseded by buried quantum wells, leading to significant improvements in the two-dimensional electron gas properties [34, 82]. More complex device geometries taking advantage of the gate control of the semiconducting weak-link showed possible evidence

of quantization of the supercurrent [83] following earlier theoretical predictions [64]. Further, analysis of multiple Andreev reflections in the finite voltage state indicated the presence of an effective superconducting energy gap in the semiconductor [84].

Following this flurry of papers, the field however started to slow down. Early hints of the fundamental issues can be found in a range of papers investigating for example the induced damage in the QW as a result of the cleaning methods prior to superconductor deposition [85, 86]. An encompassing review of the state of the field at this point was published by Schäpers [87], outlining the importance of the “interface transparency” problem, highlighted in red on the timeline.

Perhaps coincidentally, this slow down in 2DEG-superconductor hybrids saw the rise of an alternate Sm-S hybrid platform, namely semiconductor nanowires contacted with superconducting leads [88–90]. Due to the confined structure of these crystalline wires, and correspondingly large surface to volume ratio, inducing superconductivity was relatively straightforward (as it had initially been for surface inversion layers in 2D). Recent work on complex structures allowing for direct tunneling spectroscopy however have highlighted similar issues to those previously encountered in 2DEGs. Most experiments reported “soft” superconducting gaps [12, 13, 91] presumably due to disordered Sm-S interfaces [92].

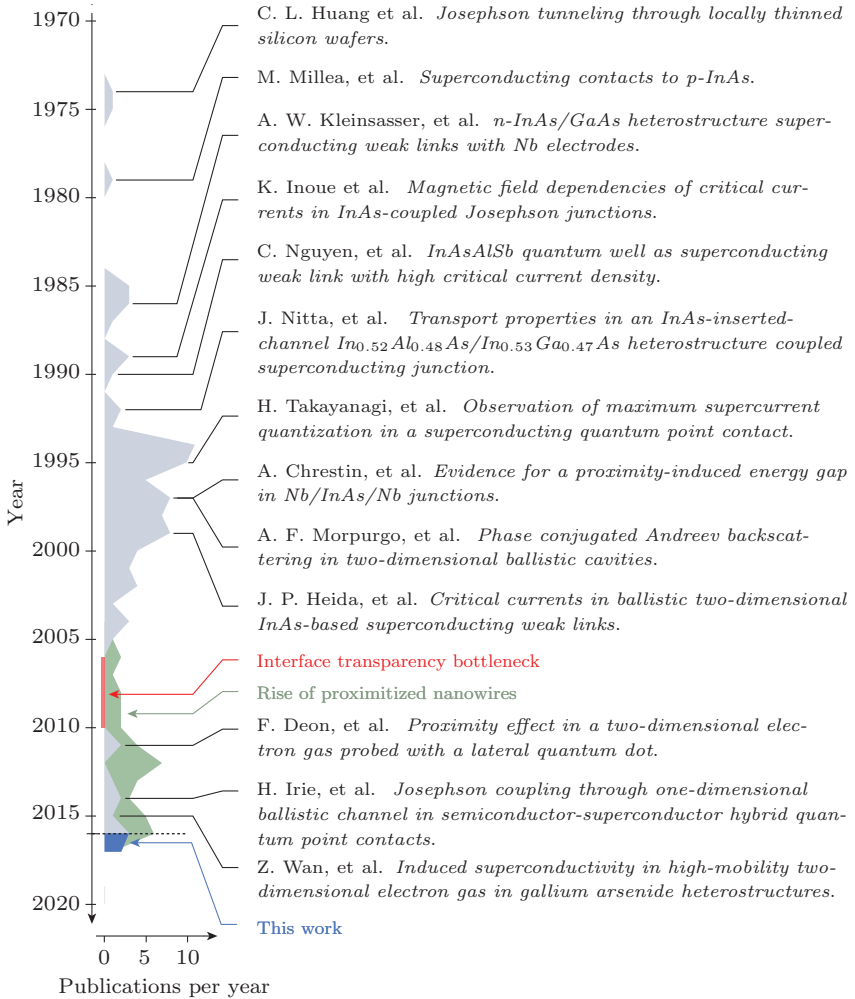
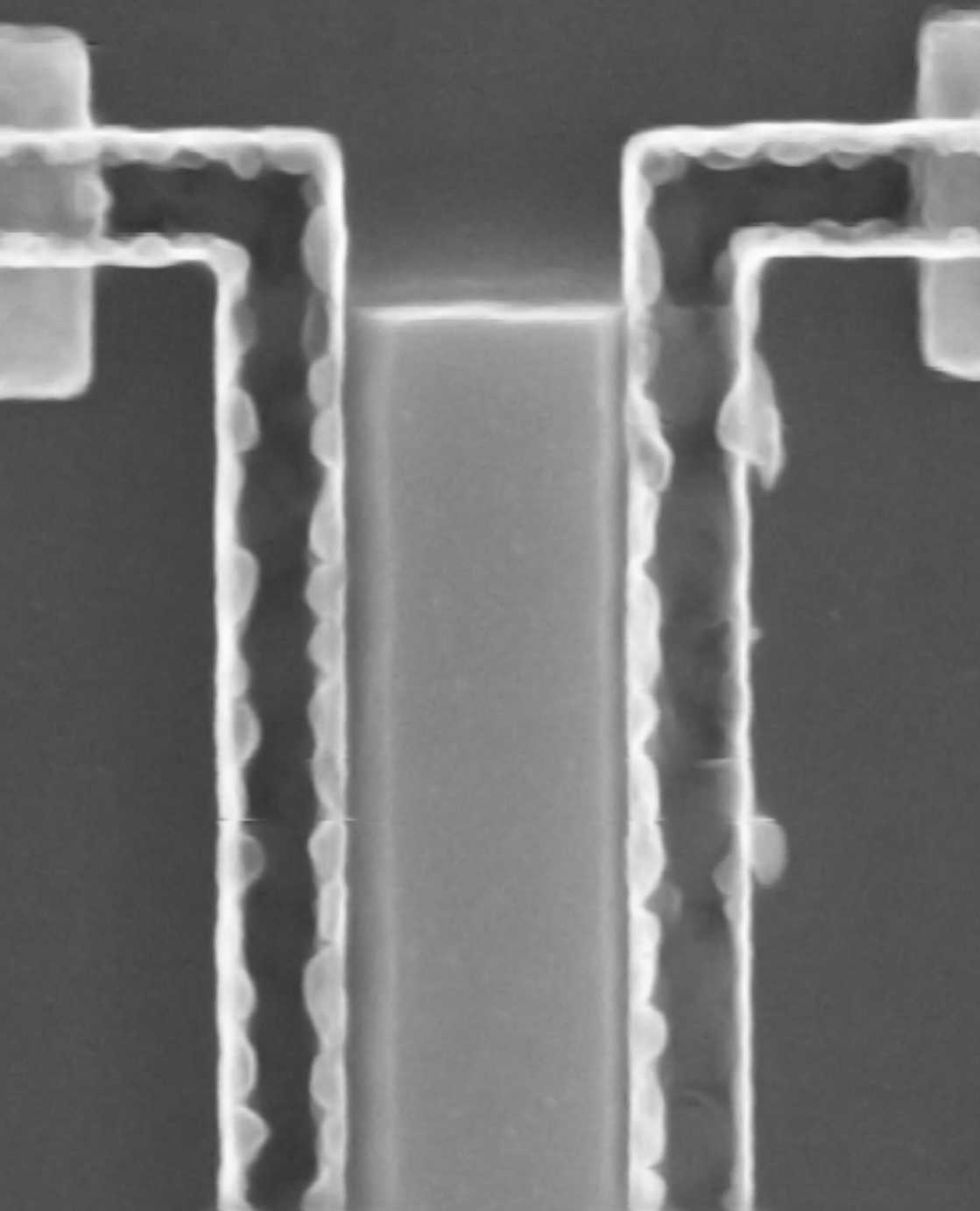


Figure 2.1: **Development of 2D Sm-S hybrids.** A selection of works highlighting the progress in III-V semiconductor-superconductor hybrids [34, 75, 80–84, 93–98]. The histogram to the left indicates the number of papers published per year in the fields of hybrid 2DEGs (blue) and nanowires (green).

Part II

EX-SITU SUPERCONDUCTING
CONTACTS



BURIED STRUCTURES

This chapter focuses on an early portion of this thesis work attempting to couple superconductors to conventional buried InAs quantum wells (QWs), largely along the lines of previously published studies [34, 99–101]. Despite somewhat promising results, the contact strategy employed here proved to be very cumbersome and hard to carry out reproducibly. Though many of the issues encountered have been documented previously [87], we include this brief chapter as a stepping stone to contrast with the vastly improved approach which was ultimately adopted, to be introduced in [Chapter 4](#).

3.1 INAS 2DEG

The wafer structure used for this portion of the work is shown in [Figure 3.1](#), together with an electrostatic Schrödinger-Poisson simulation of the QW (courtesy of J. Shabani). Hallbar characterization of the 2DEG yielded an electron mobility (at zero gate) of $\mu = 200,000 \text{ cm}^2/\text{Vs}$ at a density of $n = 3 \times 10^{11} \text{ cm}^{-2}$ [102–104].

In order to fabricate nanoscale devices from a wafer such as this, the general (simplified) fabrication flow consists of at least two steps, shown in [Figure 3.2](#). First, portions of the 2DEG must be isolated to form the active device region or mesa (middle panel), by locally etching down into the wafer. How exactly this is done will be left to the more detailed fabrication overview in [Chapter 4](#). Once the mesas are defined they need to be contacted to the outside world, this is generally done by depositing metallic contacts using electron beam evaporation (right panel). Depending on the types

of experiments envisioned a variety of metals can be used to obtain either Ohmic (well behaved and low-resistance) normal contacts or superconducting contacts.

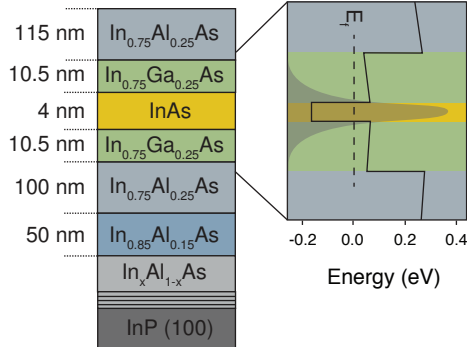


Figure 3.1: **Buried InAs 2DEG wafer structure.** Wafer stack of the buried InAs 2DEGs used in this work (left). A zoom-in of the InAs QW flanked by InGaAs barriers is shown on the right. Superimposed we show the conduction band level (solid line), and 2DEG probability density (shaded gray).

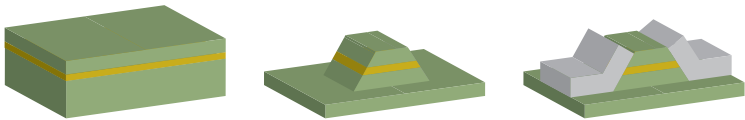


Figure 3.2: **2DEG device fabrication.** Starting from a semiconductor wafer with an embedded QW (left) devices are defined and isolated using a chemical wet-etch (middle). Finally contacts are made to the 2DEG, typically by depositing metallic electrodes using electron beam evaporation (right). A more thorough overview of the fabrication process is presented in [Figure 4.3](#).

In order to obtain superconducting contacts to the buried QW, two approaches are available [105]

- top down (2D) contacts by locally etching away the top barrier [34, 82, 106–108]
- sidewall (1D) contacts to the mesa edge [83, 109–114]

Examples of these two contact methods are shown schematically in Figure 3.3(a) and (b), with corresponding SEMs of devices fabricated utilizing these two methods in Figure 3.3(c) and (e).

For top down contacts, selective wet chemical etching of the barriers is typically employed, for example in the InP/InGaAs [106] and AlSb/InAs [82, 107] material systems. Unfortunately however, no etch exists with sufficient selectivity to stop at the InGaAs/InAs interface defining our QW [115]. One solution is to finely calibrate the etch time to stop close to the interface.

Another option is to use physical cleaning methods such as Argon sputtering [86, 116]. In this case again the etch times need to be finely calibrated to ensure the QW is not damaged or etched away in the process. One viable approach here to avoid to fine tuned calibration would be to simultaneously monitor the sputtered etch residues using secondary ion mass spectrometry. If the QW and barriers have a sufficiently differentiated material compositions this would allow for a well defined etch end point. This method has for example been used for ohmic contacts to buried InSb QWs [50], but to our knowledge has to date not been employed for superconducting contacts.

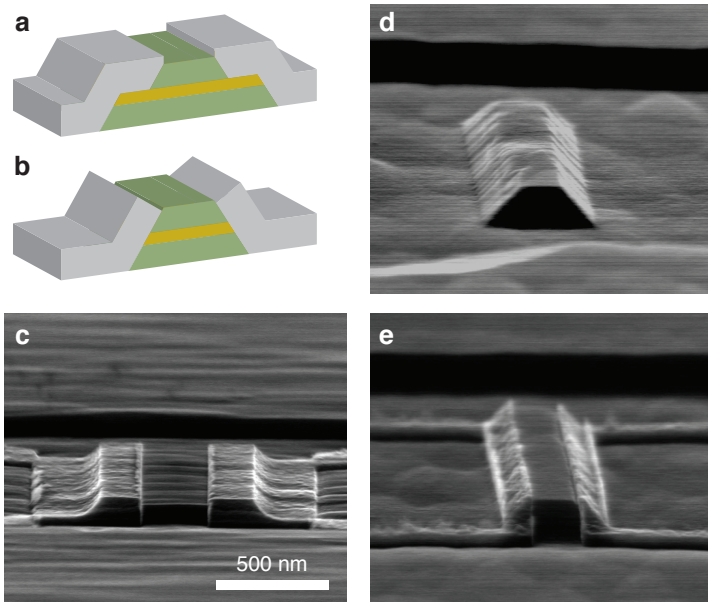


Figure 3.3: **Contact strategies to buried 2DEGs.** Schematics showing sidewall contacts (a) and top down contacts (b) between a superconductor (gray) and buried 2DEG (yellow). (c) SEM image of a completed SNS device fabricated utilizing the top down technique. (d) SEM image after mesa etching showing the isotropic etching of the III-V stack yielding a trapezoidal shape with sloping $\sim 45^\circ$ sidewalls. The corresponding sidewall contacted device after superconductor deposition is shown in (e).

Sidewall contacts are more straightforward as the 2DEG is directly exposed at the mesa periphery. The oxidation of the semiconductor surface after mesa etching however typically leads to an effectively semi-insulating barrier which must be removed before

contact deposition. Conventionally the mesa edges are cleaned *in-situ* before contact deposition, using e.g. Argon sputtering [83, 86].

Unable to decide on a clearly superior option, both approaches were investigated with the following strategies

1. **Top down contact:** Wet chemical etch to a depth of ~ 120 nm into the top barrier of the QW, followed by *in-situ* cleaning using RF plasma.
2. **Side contact:** *in-situ* cleaning using RF plasma

After a number of rounds of optimization of these methods in parallel, varying both the chemical etching and RF plasma cleaning times, the top-down contact technique was abandoned due to negligible signs of superconductivity in all tested devices. In contrast the sidewall contacted devices showed promising results early on. The fabrication steps for the surface preparation and superconductor deposition for these early results are detailed in [Method 3.1](#).

Figure 3.4(a) shows a false colored SEM image of a second generation sidewall contacted SNS device with superconducting Al contacts in blue connected to Ti/Pt/Au extension lines in yellow¹. Further, in red, fine gates can be seen allowing for control of the density distribution in the junction, which could unfortunately not be used however due issues with gate leakage. The Al contact to the the 2DEG at the sloped mesa sidewalls is shown by the zoom ins shown in [Figure 3.4\(b\)](#) and (c). The 2DEG position can be seen in the SEMs, as highlighted by the white arrow in [Figure 3.4\(c\)](#).

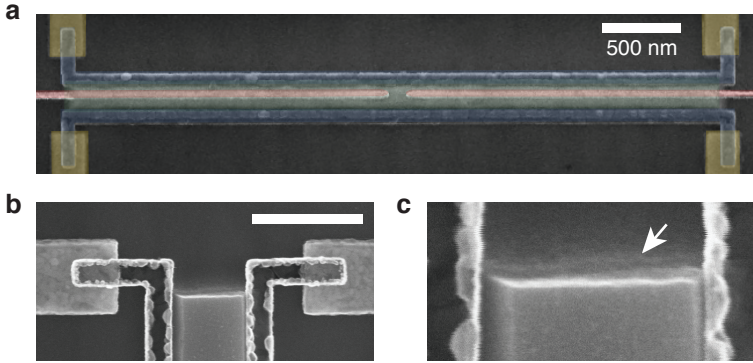


Figure 3.4: **Buried S-2DEG-S device.** (a) False colored SEM showing a second generation sidewall contacted SNS structure with normal metal leads (yellow). Superconducting Al is shown in blue contacting the mesa (green) with electrostatic gates in red. (b) Zoom in of (a) without false coloring at one end of the device highlighting the superconducting contacts climbing up the mesa sidewalls. The scale bar is shown for 500 nm. (c) Further zoom in at the exposed mesa sidewall. The faintly visible horizontal line indicated by the white arrow is the InAs QW contacted on either side by Al leads.

-
1. **Plasma clean:** 60 s RF plasma (for 4 nm)
 2. **Superconductor deposition:** Ebeam evaporation of 5 nm Ti at 0.5 \AA/s followed by 100 nm Al at 1.0 \AA/s
-

Method 3.1: Details of the initial interface cleaning and superconductor deposition.

3.2 SUPERCURRENT

3.2.1 *Inhomogeneous contacts*

An example of the typical behavior of SNS junctions prepared using the in-situ RF cleaning prior to superconductor deposition as detailed in Method 3.1 is shown in Figure 3.5(a). As a function of the driving current I the junction switches from a superconducting regime to dissipative transport with a critical current $|I_c| \sim 15$ nA. As a function of magnetic field the critical current undergoes oscillations, as a result of interference effects as described in Section 1.4.4. However, in contrast to the expected Fraunhofer type decay of the supercurrent, a smooth envelope is observed. In Figure 3.5(b) a schematic of the junction is shown together with the expected supercurrent density J_c as a function of the position along the mesa width. For a homogeneous contact, uniform density would be expected as indicated by the blue shaded area, yielding Fraunhofer diffraction as a function of magnetic field [Figure 3.5(c) blue line]. The slowly decaying envelope observed in Figure 3.5(a) is consistent with supercurrent transport at the mesa periphery as indicated by the red shading in (b) (and corresponding diffraction pattern in (c)).

This behavior was observed in a number of devices using the sample preparation detailed in Method 3.1, indicating that coupling of the Al leads to the mesa is reproducibility enhanced at the edges. This is presumably due to enhanced physical bombardment at the mesa corners during RF plasma cleaning, yielding better local contact. The possibility of other mechanisms causing electron accumulation at the mesa edges however cannot be ruled out.

As a result, the contact method was amended to include a brief wet etch for oxide removal prior to in-situ cleaning as detailed in

¹ The Pt interlayer was used to prevent the "purple plague", an insulating intermetallic formed between Au and Al [117]

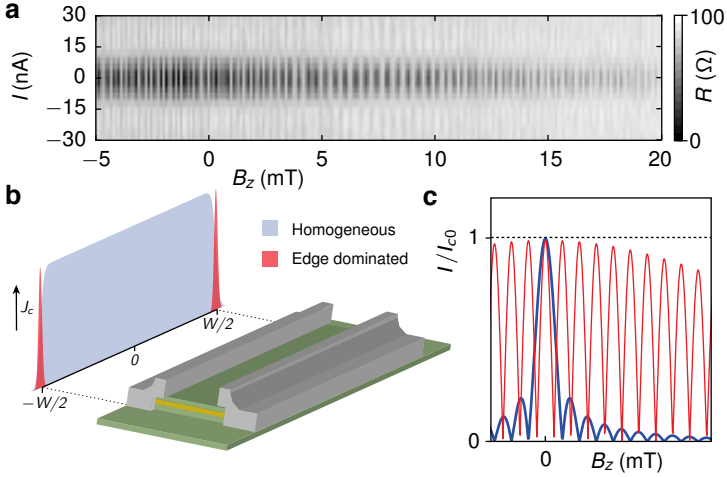


Figure 3.5: **Inhomogeneous contacts.** (a) Differential resistance R as a function of driving current I and perpendicular magnetic field B_{\perp} of a sidewall contacted SNS junction with interfaces prepared using contact method 3.1. (b) 3D schematic of the SNS junction with anticipated uniform supercurrent density J_c along the junction width (blue). A supercurrent density consistent with electron accumulation at the mesa edges is shown in red. (c) Expected critical current magnitude I_c as a function of B_{\perp} for the two current distributions shown in (b). A uniform density results in the Fraunhofer form (blue), whilst edge conduction results in a SQUID form (red).

Method 3.2². The result of this improved recipe is shown in Figure 3.6 for three devices with increasing contact separation $L = \{220, 270, 330\}$ nm from left to right. Whilst resembling the expected Fraunhofer form, irregularities are apparent, indicative of non-uniform critical current density along the contacts [119–122].

² See also appendix of Ref. [118] for further details

-
1. **Oxide removal wet etch:** 20 s mesa etch, quenched in MQ water and dried immediately prior to loading into the deposition chamber
 2. **Plasma clean:** 60 s RF plasma (for 4 nm)
 3. **Superconductor deposition:** Ebeam evaporation of 5 nm Ti at 0.5 \AA/s followed by 40 nm Al at 1.0 \AA/s
-

Method 3.2: Details of the improved interface cleaning and superconductor deposition.

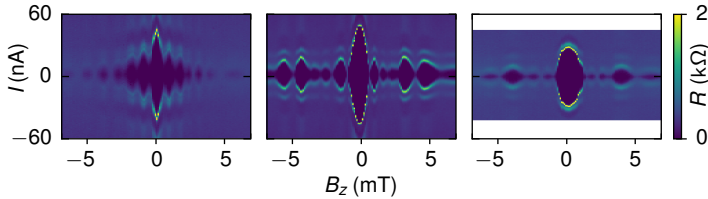


Figure 3.6: **Irregular Fraunhofer interference.** Diffraction patterns in the differential resistance R as a function of current I and perpendicular magnetic field B_z for three devices with lengths 220, 270 and 330 nm from left to right.

Further, despite the length variation between devices, the maximal critical current at zero magnetic field I_c^{\max} , is almost constant. For uniform junctions, a roughly inverse exponential dependence is expected between the critical current and the junction length $I_c^{\max} \sim \exp(-L/\xi)$ [123]. The largely independent behavior of I_c^{\max} on junction length thus suggests that it is dominated by the differences in contact transparency rather than the junction geometry.

3.3 CONFINED GEOMETRIES

3.3.1 Supercurrent in SNS configuration

Despite the issues with obtaining reproducible homogeneous and transparent contacts between Al and the buried InAs QW, more complex devices were envisioned with the goal of exploring possible topological superconductivity in this system. Figure 3.7 shows a false colored SEM demonstrating the device structure. In dark gray, along the upper edge of the mesa two Al contacts locally induce superconductivity. Surrounding the Al contacts, a number of gates (yellow) allow for electrostatic control of the electron density. Finally the ends of the mesa are connected to two Ohmic contacts on each end (not shown), allowing for four-probe transport measurements.

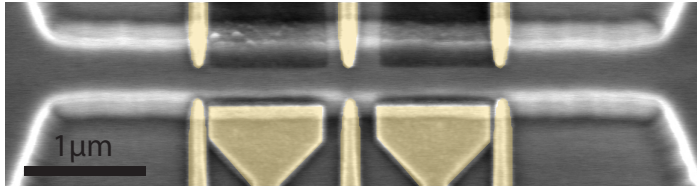


Figure 3.7: **Wire device scanning electron micrograph.** Electrostatic gates are shown false colored in yellow. The upper darker gray pads are Al contacts. The mesa extends out at either end to two Ohmic contacts allowing for four-terminal measurements through the structure.

Characterization of the superconducting properties is shown in Figure 3.8(b) and (c), with the measurement configuration indicated in (a). By fixing all the outer gates to $V_g = 0$ and utilizing the

central QPC gates, the device can be tuned from a superconducting regime (Figure 3.8(b), solid line) to an insulating state (dashed line). This is evidenced by the negligible voltage drop observed in the range $I = \pm 20$ nA for $V_g = 0$, indicative of a supercurrent. Conversely for $V_g = -3.9$ V the nearly vertical slope of the IV curve indicates insulating behavior. The full gate voltage dependence of the critical current is shown in Figure 3.8(c). The critical current is relatively stable $I_c \sim 20$ nA down to approximately $V_g = -1.5$ V after which it steadily decreases to zero as the junction is depleted.

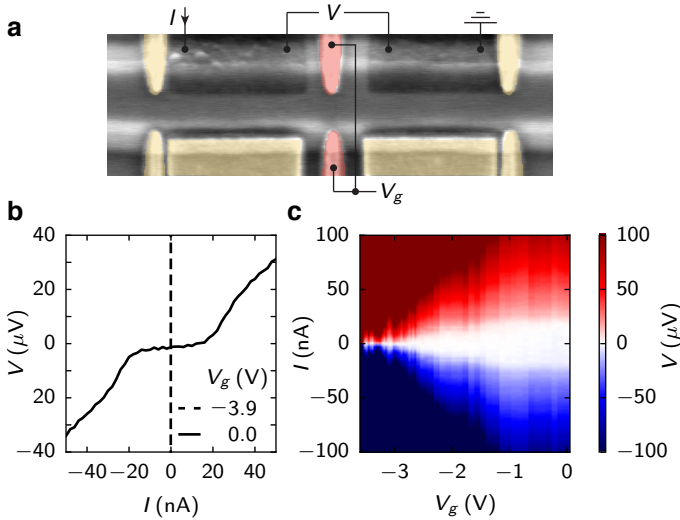


Figure 3.8: **Supercurrent in confined buried structures** (a) False colored SEM of the device, showing the measurement configuration. The yellow gates are held at a fixed potential while the red ones are varied to tune the device from an open superconducting regime (b, solid line) to an insulating state (b, dashed line). (c) Four-terminal voltage drop across the junction as a function of driving current and gate voltage.

3.3.2 Tunneling spectroscopy

In [Figure 3.9\(a\)](#) we change the contact configuration to study transport across a single SN interface. By fully depleting the middle QPC (red), we cut off the right side of the device. [Figure 3.9\(b\)](#) shows the device conductance as a function of the source-drain bias³ V and left QPC gate voltage V_{lqpc} . In the open regime, near zero bias, a finite conductance enhancement is observed as shown by the gray linecut in [Figure 3.9\(c\)](#). For more negative gate voltages a BCS-like superconducting gap on the order $\Delta^* \sim 100 \mu\text{eV}$ (black) develops. To our knowledge this is the first reported direct tunneling spectroscopy on a proximitized buried 2DEG structure⁴.

For such an S-QPC-N geometry, the expected behavior can be understood by extending the analysis of [Figure 1.10](#) to the quantum (single channel) regime [[124](#)]. Qualitatively the measurements mirror [Figure 1.10](#) with a gradual transition between a zero-bias conductance enhancement owing to excess current carried by Andreev reflections, to a zero-bias conductance suppression in the tunneling regime directly probing the gapped local density of states in the proximitized QW. The theoretical expectation for the zero bias conductance (G_{NS}) as a function of the normal state conductance (G_{NN}) is given by [[124](#)]

$$G_{\text{NS}} = 2G_0 \frac{G_{\text{NN}}^2}{(2G_0 - G_{\text{NN}})^2} \quad (3.1)$$

and is shown by the red curve in [Figure 3.9\(d\)](#), together with the experimental data (black dots)⁵. The large discrepancy between the data and the theoretical expectation is likely due to a poor

³ The data are plotted using the measured four-terminal voltage drop V , between the source and drain leads, when a voltage V_{sd} is applied at the source electrode.

⁴ An indirect measurement through a proximitized quantum dot is reported in [[96](#)]

⁵ With G_{NN} extracted at large bias ($V \gg \Delta^*$)

superconductor-semiconductor interface resulting in a “soft gap” [125].

Finally in Figure 3.9(e) the superconducting gap is investigated as a function of magnetic field B_{\parallel} , applied in the plane of the junction parallel to the S-N contact as indicated in the Figure 3.9(a). Despite the relatively thin Al leads (~ 40 nm), the induced gap is rapidly suppressed, collapsing at roughly $B_c = 0.2$ T.

3.4 OUTLOOK

The results presented in this chapter on proximitizing buried 2DEGs highlight the difficulties with this approach. Largely these results confirm the issues previously encountered in the literature (c.f. Figure 2.1). The quality of the superconductor-semiconductor interface is paramount, and chemical etching methods together with physical in-situ cleaning seem insufficient to obtain strong and uniform coupling.

Ideally one would remove the requirement of cleaning the semiconductor interfaces entirely and grow the entire superconductor-semiconductor structure in the same growth chamber. One viable route may be to utilize cleaved edge overgrowth of superconductors in-situ [126]. Another option may be to etch the mesa structures and subsequently load them into an MBE chamber and degas them at high temperature before superconductor deposition. For III-V materials however, especially InAs and InSb it is unclear if the temperatures needed for degassing are too high to ensure the integrity of the QW structure.

In the next chapter we introduce a novel approach allowing for in-situ growth of the superconductors in the MBE chamber by bringing the 2DEG closer to the surface.

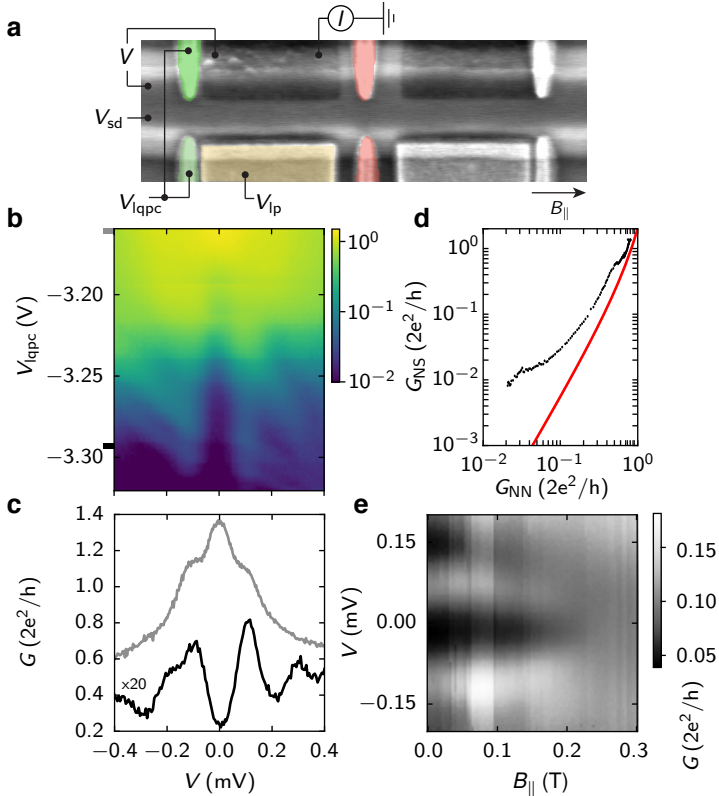
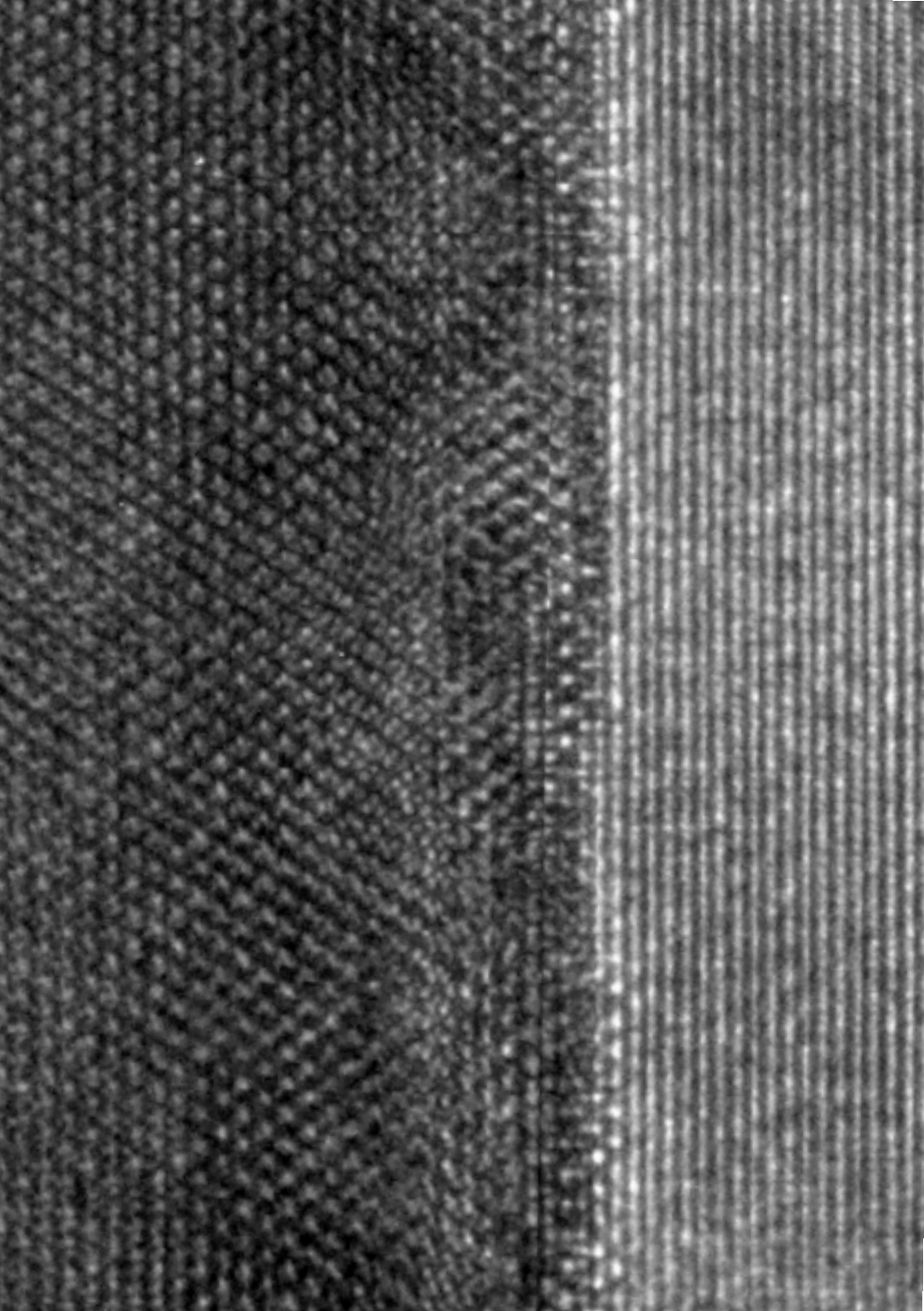


Figure 3.9: **Tunneling spectroscopy in a buried structure.** (a) False colored SEM of the device, showing the measurement configuration. The gates in red are fixed at -4 V to isolate the left side. The gates in green are operated in the QPC regime. (b) Conductance through the S-QPC-N as a function of gate voltage and source-drain bias. (c) Line cuts from (b) in the open (gray) and tunneling regimes (black). (d) Zero bias conductance G_{NS} plotted against the normal state conductance G_{NN} (black dots), extracted from (a). The theoretical expectation from Equation 3.1 is shown in red.

Part III

EPITAXIAL SUPERCONDUCTING
CONTACTS



SUPERCONDUCTOR-SEMICONDUCTOR HETEROSTRUCTURES

4.1 INTRODUCTION TO A NEW PLATFORM

Owing to the plethora of issues with obtaining transparent superconducting contacts to buried quantum wells, a new approach was developed to grow superconductors directly on the III-V wafer stack. This idea followed recent success with nanowires where epitaxial matching between the underlying InAs crystal structure and covering Al was demonstrated [127], together with strongly enhanced properties in transport experiments [125].

Indeed this isn't a totally novel approach, and has coincidentally been attempted before with promising results here in the same building at HCØ almost 20 years ago [128, 129] as well as in Cambridge sometime later [130]. However at the time the target was to obtain transparent superconducting contacts to GaAs which typically forms large Schottky barriers at the interface. Follow up experiments nonetheless demonstrated clear evidence of a supercurrent [131, 132] and multiple Andreev reflections [133, 134].

4.1.1 *Material considerations*

First a near-surface InAs quantum well is grown by MBE and capped with an InGaAs barrier of thickness d as shown in Figure 4.1a. Without breaking vacuum, a thin Al film of thickness h is then grown on top. Under the right growth conditions the Al forms an epitaxial match with the crystal structure of the underlying semiconductor [127].

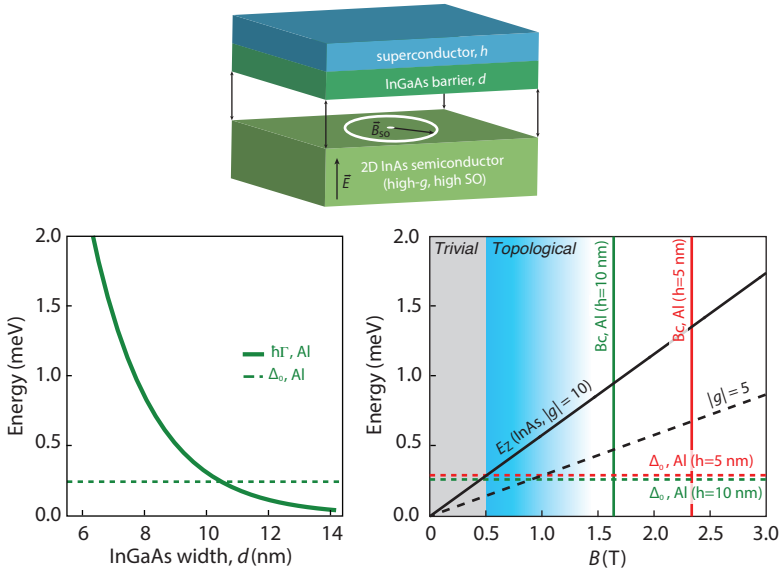


Figure 4.1: **Superconductor-semiconductor hybrid material considerations.** (a), General design for a hybrid superconductor/near-surface InAs z DEG structure with tunable inter-layer coupling via a InGaAs barrier of variable width d . (b) Semiconductor-superconductor coupling $\hbar\Gamma$ as a function of InGaAs barrier thickness (solid). The Al superconducting gap is shown for comparison (dashed). (c) Estimated Zeeman energy for quasiparticle states with $|g| = 10$ (solid black) and $|g| = 5$ (dashed black). Green and red solid lines indicate the in-plane critical fields of Al films of thicknesses 10 nm and 5 nm respectively. Similarly the gaps for these films are shown by dotted lines. For appropriate structures the topological regime is anticipated for $E_z > \Delta$, highlighted in light blue (for $|g| = 10$).

The reasoning for adding the InGaAs cap may be unclear at first, it's primary role being to enhance the mobility of the carriers in the

2DEG by pushing the wavefunction away from scattering impurities at the surface. To give an idea for scale, typical InAs surface inversion layers have mobilities on the order $7000 \text{ cm}^2/\text{Vs}$ whilst buried InAs quantum wells as discussed in [Chapter 3](#) have typical mobilities on the order $200,000 \text{ cm}^2/\text{Vs}$ [102, 103], with recent on structures grown on lattice matched substrates reaching as high as $\mu = 700,000 \text{ m}^2/\text{Vs}$ [135–137]. Further, the width of the barrier allows control over the coupling between the superconductor and 2DEG. Whilst the overall goal is to have a clean and transparent interface, recent theoretical insights suggest that too strong of a coupling may also hinder experiments probing topological systems [138].

By varying the height of the barrier, the interface can be tuned such that the 2DEG inherits superconducting properties from the proximitizing superconductor whilst retaining the large SOI and g-factors inherent to the InAs QW. The extent to which these quantities are renormalized by the superconductor is non-trivial, however a good estimate can be made by considering the wavefunction weights residing in the S_m and S regions. The average time quasiparticles spend in the InAs QW is governed by the coupling to the superconductor $\tau_{sm} \sim 1/\Gamma$ [139]. The time spent in superconductor on the other hand is given by $\tau_s \sim \hbar/\Delta$ with Δ the superconducting gap. A simple compromise in terms of proximity coupling whilst retaining the semiconductor characteristics is obtained for $\tau_{sm} = \tau_s$ such that the quasiparticles spend on average an equal amount of time in the semiconductor and superconductor.

In [Figure 4.1b](#) we plot $\hbar\Gamma$ as a function of InGaAs barrier thickness (solid line), with the superconducting gap $\Delta = 250 \text{ } \mu\text{eV}$ for a 10 nm thick Al film shown dotted. The intersection between these two curves indicates the ideal region of operation from the perspective of coupling optimization such that $\Delta = \hbar\Gamma$. It is worth noting that this doesn't tell the whole story as the mobility in the 2DEG is also of considerable importance, the ideal structure in practice

may compromise on coupling in order to push the 2DEG to higher mobilities leading to overall better results.

The final variable parameter to consider is the superconductor thickness h . For simplicity we concentrate here on Al films as these are relatively well lattice matched to InGaAs and have been shown to work well on InAs nanowires [127]. Furthermore, the ubiquity of Al in most MBE systems, and its widespread adoption in the superconducting electronics community, makes this a well understood and relatively easy material to work with. For the curious and forward thinking reader, full tabulations of lattice mismatches between elemental metals (and superconductors) and the III-V binaries (InAs, InSb, GaAs) are provided in the supplementary material of Ref. [127].

In order to be viable as a platform for topological devices, the superconducting film needs to withstand sizable magnetic fields of the order $B > \Delta / (g\mu_B)$, with μ_B the Bohr magneton and g the g -factor in InAs [140]. Whilst bulk Al has a comparatively low critical magnetic field of 10 mT [141], thin films can sustain significantly larger magnetic fields when they are applied in-plane [142–144], even up to 6.0 T [145]. In Figure 4.1c the Zeeman energy E_Z of a state with the g -factor of InAs $|g| = 10$ is shown as a function of magnetic field (solid black). As realistically the effective g -factor may be lower due to renormalization by coupling to the superconductor, we also show for reference in dashed black the energy for a state with $|g| = 5$. Dashed green and dashed red lines indicate the respective quasiparticle gaps for Al films of thicknesses 10 nm and 5 nm respectively, the critical fields B_c are shown as solid lines. For both values of the g -factor it is clear that $E_Z > \Delta_0$ for $B < B_c$, the practical criterion for accessing the topological regime.

In Figure 4.2a we show a TEM cross section of a grown superconductor-semiconductor heterostructure, indicating a clean match at the interface. Due to very similar scattering cross sections, InGaAs and InAs cannot be directly distinguished from TEM imaging. In Fig-

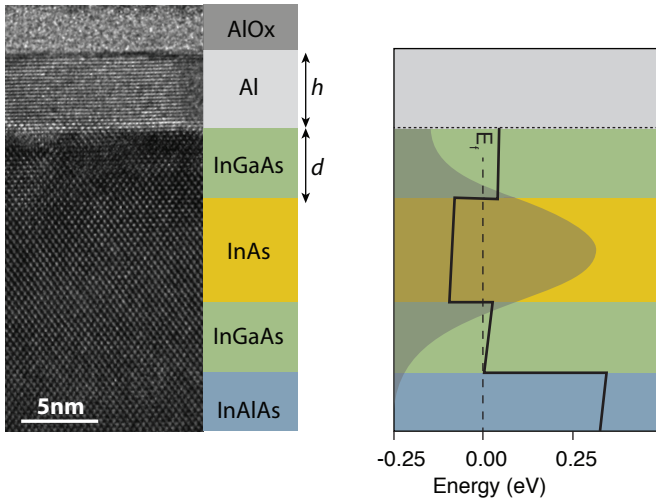


Figure 4.2: **Superconductor-semiconductor epitaxy.** (a) TEM cross section of the wafer structure with $d = 5$ nm and $h = 7$ nm. (b) Schrödinger-Poisson simulation showing in black the conduction band energy and the 2DEG probability density as a function of depth z from the surface (in a.u.).

Figure 4.5b a Schrödinger-Poisson simulation is shown for the grown structure. The conduction band profile is indicated in black, with the Fermi level highlighted by the dashed line. The corresponding electron probability density is shown in shaded gray, centered at the InAs QW with finite tails leaking into the lower barrier and the surface Al layer. This wavefunction leakage into the surface superconductor is key to proximitizing the 2DEG.

4.2 FABRICATION

Now that we have a material to work with, the next step is to develop a fabrication recipe. An overview of steps required to go from a wafer received from our collaborators to a working device are shown in [Figure 4.3](#). As this recipe was developed together with M. Kjaergaard and detailed in great depth in his thesis [118], we limit ourselves here to a high level overview (with details in [Appendix A](#)).

The first step in the process is cleaving the large growth wafers into appropriately sized $5 \text{ mm} \times 2.5 \text{ mm}$ chips. This is done by aligning to the underlying crystal axes and using a diamond scribe to dice up the wafer. Due to growth constraints the material quality is typically highest near the center of the wafer, thus we start by using chips from this region as shown in the figure. The outer edges are discarded or used for preliminary process optimization.

Before fabrication can commence, we need to design the devices using computer aided design (CAD) software. An example of a typical chip layout is shown in [Figure 4.4](#) (top right). For each subsequent fabrication step, a separate mask is designed as indicated by the color groupings: blue for the mesa etch, green for the aluminium etch, and yellow for the gate deposition. The subgroupings shown in [Figure 4.4](#) indicate masks exposed within the same step, however with different exposure parameters. This is somewhat of an implementation detail, however it is important to minimize the overall exposure time. Using such minor modifications the mesa etch exposure (with over 50% chip coverage) for example takes on the order of 2h, while it would take orders of magnitude longer otherwise.

Once the design is set it's time to get comfortable in the clean room. The overall fabrication flow requires five separate steps, four of which require lithographic patterning. In order to imprint the designs onto the chip, first a thin layer of polymeric resist is spun

onto the chip surface. Next by using an electron beam lithography system, the desired pattern can be exposed such that upon chemical development the exposed regions of the polymer dissolve away. This yields a chip with a polymer mask of the designed pattern, ready for further processing.

The first step is to define the mesas using a standard III-V chemical wet etch. Next, aluminium is selectively etched away in certain areas¹, for example to create the S-N junction shown in [Figure 4.3](#). This is followed by atomic layer deposition of an insulating oxide covering the entire chip. Finally electrostatic gates are patterned and deposited in a two-step process using electron-beam evaporation. Full processing details for each of these steps are included in [Appendix A](#).

¹ Another option is oxidize it, see [Figure A.1](#)

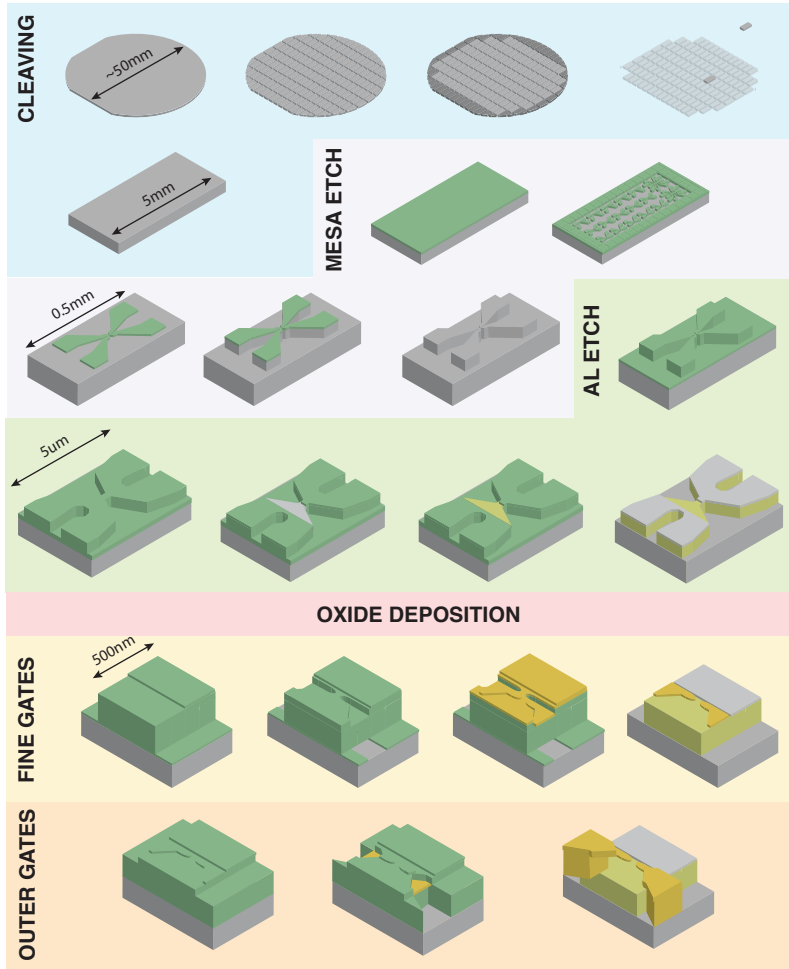


Figure 4.3: **Epitaxial device fabrication.** A simplified process flow showing all steps required to go from a bare semiconducting wafer to a working S-QPC-N device.

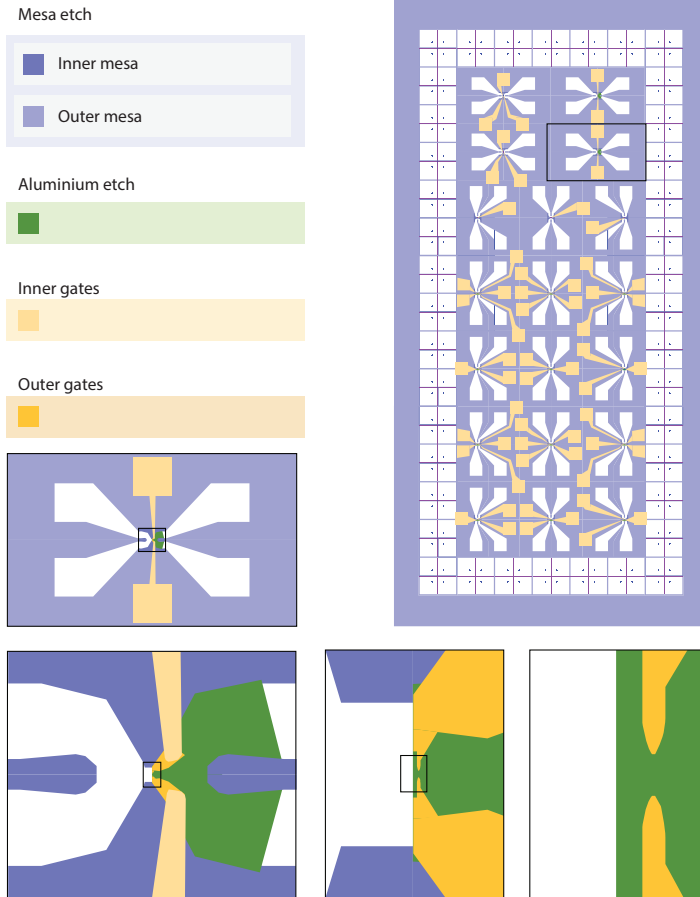


Figure 4.4: **CAD chip layout** Example of a typical chip layout (top right), with masks for each subsequent fabrication step indicated by the color groupings shown on the left. Successive zoom-ins from the global layout to a S-QPC-N device are shown at the bottom.

4.3 AL AND 2DEG PROPERTIES

4.3.1 Al film

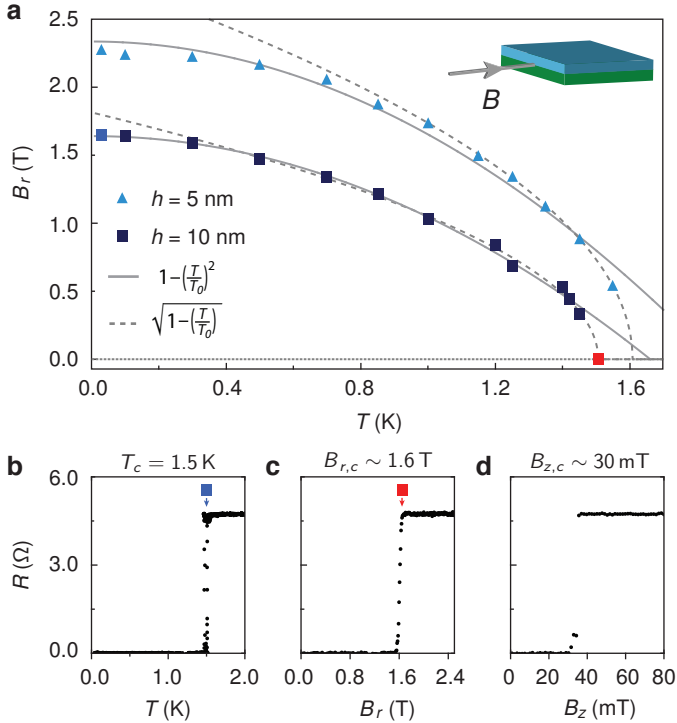


Figure 4.5: **Epitaxial aluminum film properties.** (a) Superconducting phase boundaries for films of thickness $h = 5$ nm (triangles) and $h = 10$ nm (squares) as function of temperature and in-plane magnetic field. Resistance as a function of temperature (b), in-plane magnetic field (c) and perpendicular field (d) for the $h = 10$ nm film.

To characterize the grown Al films, a range of films of different thicknesses were measured to determine both their critical temperature T_c and in-plane magnetic field $B_{r,c}$. In [Figure 4.5\(b\)](#) a characteristic measurement of a $h = 10$ nm film is shown (for $B_r = 0$) as a function of temperature. As the temperature is decreased, at $T = 1.5$ K a sharp transition is seen in the resistance of the film from approximately $R = 5 \Omega$ to $R = 0$ indicating the onset of superconductivity. Similar measurements are shown in [Figure 4.5c](#) and [d](#) as a function of in-plane B_r and perpendicular B_z magnetic fields (taken at $T = 30$ mK). At base temperature the obtained values for the parallel and perpendicular critical fields for the $h = 10$ nm film are $B_{r,c} \sim 1.6$ T and $B_{z,c} \sim 30$ mT. In [Figure 4.5\(a\)](#) the superconducting phase boundaries are shown for the $d = 10$ nm (squares) and 5 nm films (triangles). At elevated temperatures the data is relatively well described by the BCS form $B_c(T) = B_c(0)[1 - (T/T_c)^2]$ [[54](#)]. For low temperatures, the thinner 5 nm film is better described by the Chandrasekhar-Clogston limit $B_c = \Delta_0/\sqrt{2}\mu_B \sim 2.4$ T [[146](#), [147](#)]. Close to T_c data from both films is well described by $B_c(T) = B_c(0)\sqrt{1 - T/T_c}$ [[148](#)].

4.3.2 *Two-dimensional electron gas*

Having established that the Al film is working as anticipated the next step is to characterize the 2DEG. Unfortunately characterizing the proximitized 2DEG under the Al seems out of reach, at least from a transport perspective, owing to the orders of magnitude higher carrier density in the Al film shunting out anything we might hope to see in the 2DEG. Nonetheless, by either growing identical structures without the Al, or simply etching the Al away, the properties of the normal 2DEG can be studied.

In [Figure 4.6\(a\)](#) we show an optical micrograph of a typical characterization Hall bar used for both testing the properties of the Al film as described in [Section 4.3.1](#) and for investigating the proper-

ties of the 2DEG. The left and right edges of the devices, in light gray, are covered in epitaxial Al and act as the source and drain electrodes. The left side of the Hall bar is fully covered in Al and is used for characterizing the film. On the right side however, the Al is etched away exposing the InGaAs surface (dark gray surface). The gold pad covering this region in the micrograph is a global top gate allowing us to tune the carrier density in the Hall bar. The measured longitudinal ρ_{xx} and Hall ρ_{xy} resistivities measured on such a device as a function of perpendicular magnetic field are shown in Figure 4.6(b) in black and red respectively, for $V_g = -2.5$ V ($d = 10$ nm). These traces show the hallmarks of two dimensional transport, namely Shubnikov de Haas oscillations in the longitudinal resistivity, and the quantum Hall effect at high field.

Extracted from low field Hall measurements, the evolution of carrier density and mobility as a function of gate voltage are shown in Figure 4.6(c) and (f) for two wafers with $d = 10$ nm (solid) and $d = 0$ nm (dashed). The general trend in both wafers is similar, for more negative gate voltages the carrier density falls roughly linearly whilst the mobility increases gradually before peaking and falling to zero. Such a non-monotonic behavior of the mobility could be interpreted as the wavefunction being pushed away from the surface as the gate voltage is made more negative. However, further measurements comparing the extracted densities from the Hall slope compared to the Shubnikov de Haas spectrum revealed that near $V_g = 0$ (Figure 4.6(b), gray) two subbands are occupied in the 2DEG (see also Section 5.2). Probably then as the second subband is depleted by gating a reduction of intersubband scattering is responsible for the mobility peak. It is still unclear whether these two mechanisms might coexist however.

In Figure 4.6(d) the mobilities of a range of wafers are shown with different barrier thicknesses. Further, we compare sets of wafers that were grown without Al (red) to those where the Al has been

chemically etched (gray). The observed trend is in agreement with the preliminary comparison between the $d = 10$ nm and $d = 0$ nm wafers, a larger barrier tends to increase mobility, most likely due to a suppression of surface impurity scattering. Moreover, the etching process appears to have a non-negligible effect on the 2DEG mobility suggesting that improved process development could potentially yield up to a factor of two improvement.

Finally in [Figure 4.6\(f\)](#) the low field magnetoconductance measured on a wafer with a 5 nm InGaAs barrier is shown, in units of $\delta\sigma = \sigma(B) - \sigma(B = 0)$. The measurements were taken at a density of $n = 1 \times 10^{16} \text{ m}^{-2}$ to ensure single subband occupation. The zero field conductance enhancement is indicative of weak antilocalization, arising as a result of spin-orbit coupling. Utilizing a model developed by Iordanski, Lyanda-Geller, and Pikus (ILP) [[149](#), [150](#)], the fit to the data yields two parameters, the phase coherence length $l_\phi = 350$ nm and Rashba coefficient $\alpha = 0.28 \text{ eV\AA}$, corresponding to a spin-orbit length $l_{so} \sim 50$ nm. Further details can be found in Ref. [[151](#)].

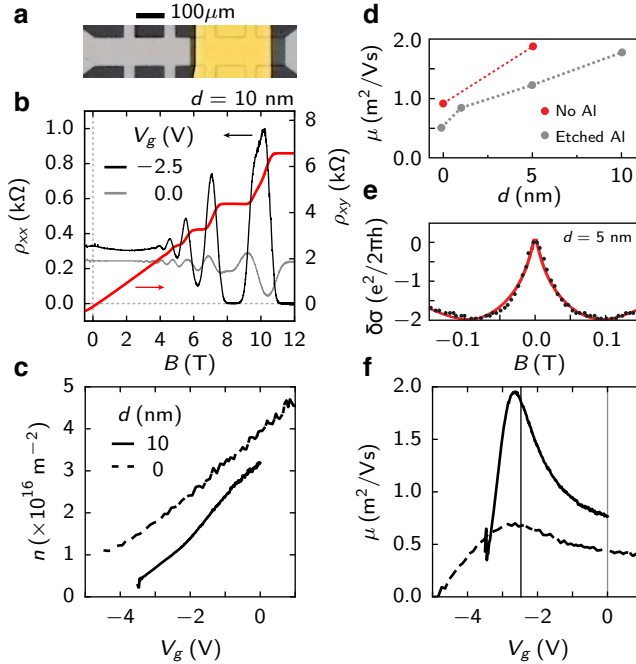


Figure 4.6: **Two-dimensional electron gas properties.** (a) Optical micrograph showing the Hall bar structure used to characterize both the Al film and the 2DEG. (b) Longitudinal and Hall resistivities as a function of perpendicular magnetic field at $V_g = -2.5$ V in black and red respectively. The longitudinal resistivity at $V_g = 0$ is shown in gray. All traces are for $d = 10$ nm. Density (c) and mobility (f) as a function of gate voltage for $d = 10$ nm (dashed) and $d = 0$ nm (solid). (d) Extracted peak mobilities as a function of InGaAs barrier thickness d , for samples grown without Al (red) and etched Al (gray). (e) Low field magnetoconductance $\delta\sigma = \sigma(B) - \sigma(B = 0)$ for $d = 5$ nm. The red curve is a fit using the ILP model.

4.4 ANDREEV QUANTUM POINT CONTACT

In order to investigate the properties of the induced superconductivity in this system, we investigate an S-QPC-N structure as shown by the zoom in (lower right) of Figure 4.4. This is essentially the same experiment as that presented on buried structures in Figure 3.9. The results are shown in Figure 4.7 for two nominally identical devices.

Probing the normal state of the junction, with a large source-drain bias ($V_{sd} \gg \Delta$, red), high temperature ($T > T_c$, green) or large magnetic field ($B_{\perp} > B_{\perp,c}$), a well defined conductance plateau is observed at $G = 2e^2/h$, consistent with the behaviour of a conventional quantum point contact. In the superconducting regime however, the conductance is doubled to $G = 4e^2/h$ (black traces).

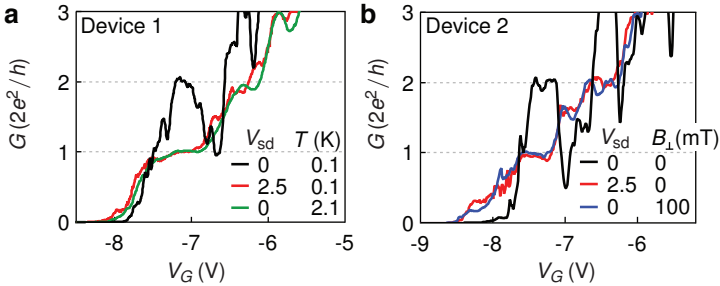


Figure 4.7: **Andreev quantum point contact.** (a,b) Differential conductance G as a function of gate voltage V_G for two nominally identical S-QPC-N junctions. Traces are shown at zero bias for both devices (black) indicating a conductance plateau at $4e^2/h$, double the value observed for large V_{sd} (red), high temperature (green), or large magnetic field (blue).

Figure 4.8(a) investigates the S-QPC-N conductance as a function of gate voltage and source-drain bias (c.f. Figure 3.9. Near

$V_G = -8.2$ V on the first QPC plateau the conductance enhancement is visible, with a line-cut shown in (b). At more negative gate voltages, the conductance near zero bias is strongly suppressed. This conductance gap indicates the induced superconducting gap Δ^* in the QW. In contrast to the buried structures where a gap was also observed, the gap appears better defined and “harder”. To investigate this, in [Figure 4.8\(c\)](#) we plot the zero bias conductance against the normal state conductance, determined by averaging for $V_{sd} > 0.8$ mV. The experimental data, extracted from (a) are shown as black dots. For comparison the data from [Figure 3.9](#) is overlaid in blue. Finally the green curve is the theoretical prediction of [Equation 3.1](#) [124], without any fitting parameters. The good agreement between the theory and experiment over two orders of magnitude, and up to $4e^2/h$, indicates that the junction is well described by nearly perfect Andreev reflection of a single mode.

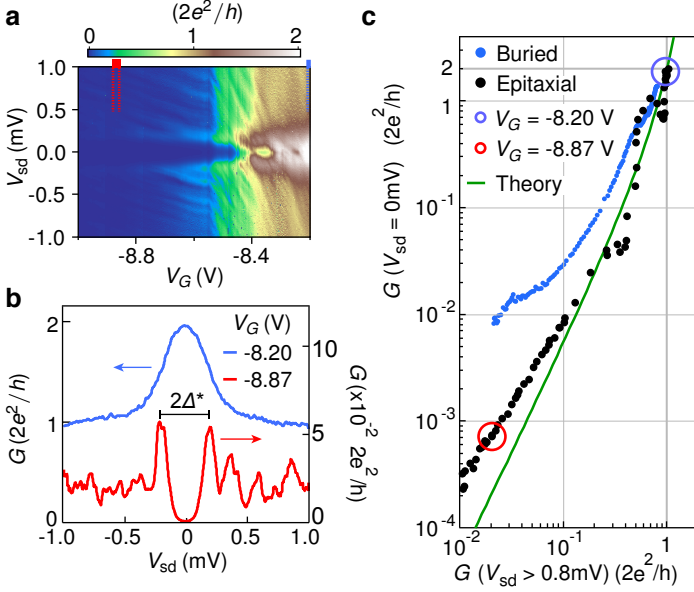
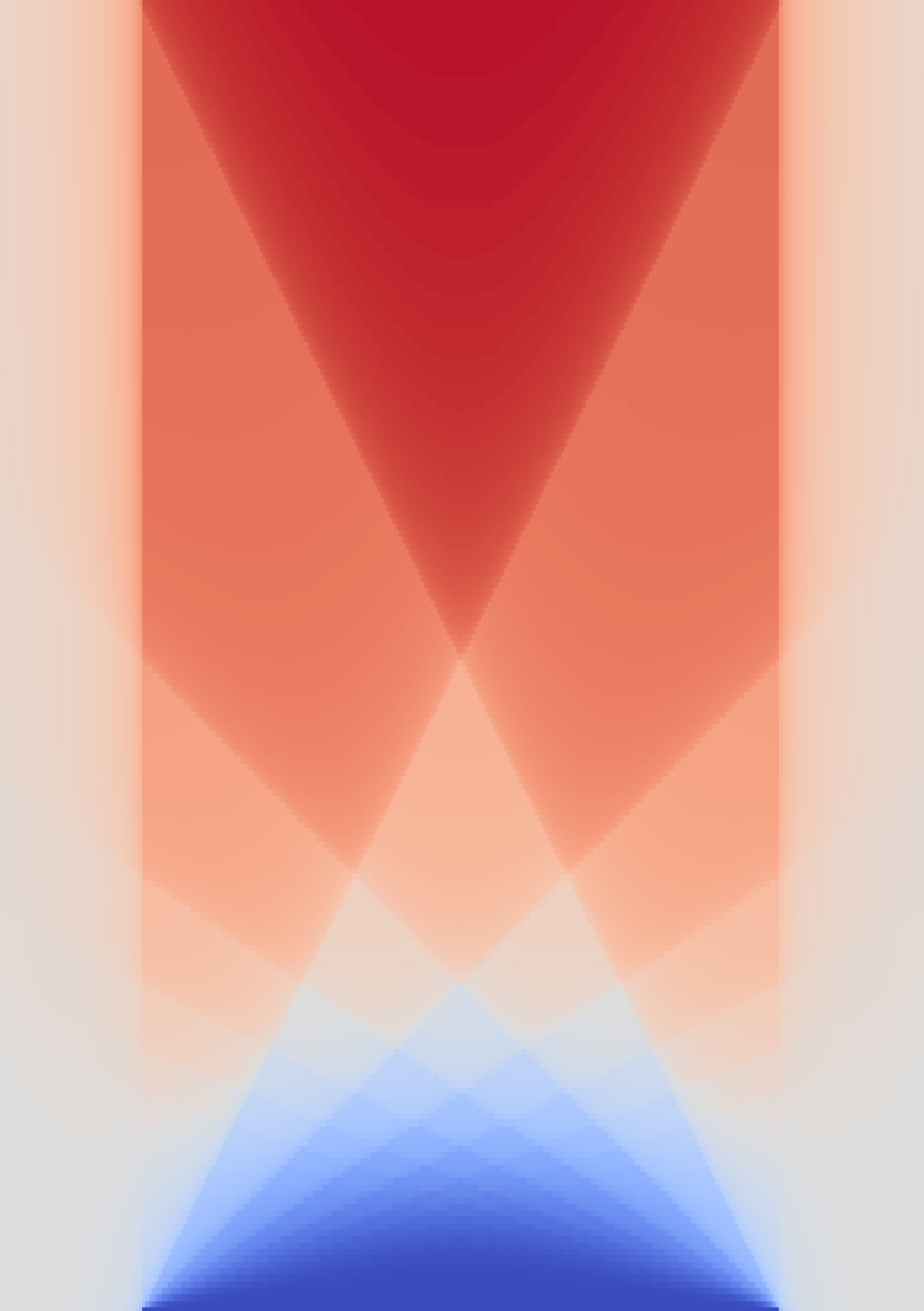


Figure 4.8: **Hard superconducting gap.** (a) Differential conductance map as a function of gate voltage and source drain bias from device 1. (b) Line cuts of (a) at the indicated positions demonstrating the conductance doubling on the first plateau, and a hard superconducting gap near pinch off. (c) G at zero bias versus G for $V_{sd} > 0.8$ mV, indicating the ratio between the in-gap and normal state conductance. Black dots are extracted from (a), blue dots indicate the behaviour of the buried QW device from Figure 3.9. The green line is the theoretical prediction following Equation 3.1.



Measurement of multiple Andreev reflection (MAR) in a Josephson junction made from an InAs quantum well heterostructure with epitaxial aluminum is used to quantify a highly transparent effective semiconductor-superconductor interface, indicating near-unity transmission. The observed temperature dependence of MAR does not follow a conventional BCS form, but instead agrees with a model in which the density of states in the quantum well acquires an effective induced gap, in our case $180 \mu\text{eV}$, close to that of the epitaxial superconductor, indicating an intimate contact between Al and the InAs quantum well. Carrier density dependence of MAR is investigated using a depletion gate, revealing the subband structure of the proximitized quantum well, consistent with magnetotransport experiments of the bare InAs performed on the same wafer.

5.1 JOSEPHSON JUNCTION IN A QW HETEROSTRUCTURE

We report multiple Andreev reflection (MAR) in a gateable Josephson junction formed from an InAs 2DEG/epitaxial Al heterostructure. We observe a temperature dependence of the MAR peak positions that differs from expectations for a conventional BCS-like gap, but is consistent with an induced gap in the InAs under the Al [92, 138, 153, 154]. The appearance of an induced gap, Δ^* , in the local density of states of the semiconductor reflects the finite time a state from the quantum well spends in the superconductor [155].

Adapted from [152]

Comparing MAR data to a quantitative model (described below), we infer an induced gap $\Delta^* = 180 \mu\text{eV}$ in the InAs region covered by Al, and a transmission through the effective interface formed at the boundary between the covered and uncovered InAs in excess of 97%. These results are consistent with tunnel spectroscopy measurements on the same wafer [156].

The high transparency of our junction is further confirmed by the shape of the MAR features, where we observe *dips* in conductance when the applied voltage is a fraction of the gap, $V = 2\Delta^*/en$. This dip-to-peak transition in conductance is a longstanding prediction for highly transparent junctions [157], also confirmed by our quantitative modeling. To our knowledge, this inversion is often overlooked in the experimental literature, even for junctions considered highly transparent (see, for instance, Ref. [88, 90, 158]), leading to erroneous identification of the gap. We discuss the dip-to-peak transition further in Section 5.2 below.

Modeling also reveals the existence of two distinct families of MAR resonances at zero top-gate voltage, which we associate with two occupied subbands in the 2DEG. By energizing a top gate on the exposed 2DEG, the resonant features change, becoming consistent with single-subband occupancy. The gate-dependent change from two to one subband is consistent with magnetotransport measurements on a Hall bar with the Al removed, fabricated on the same wafer.

Figure 5.1(a) shows a false-color scanning electron micrograph of the final device, and Fig. 5.1(c) shows a schematic cross-section through the junction. The exposed 2DEG region has a length $L \simeq 250 \text{ nm}$ and a width $W = 3 \mu\text{m}$. The superconducting gap of the 10 nm thick Al layer is inferred from the critical temperature ($T_C = 1.56 \text{ K}$, independently measured in four-terminal measurement) via $\Delta_{\text{Al}} = 1.76 k_B T_C = 237 \mu\text{eV}$. We note that the gap of the Al layer is larger than bulk Al [159], with a T_C consistent with previously reported values [160, 161].

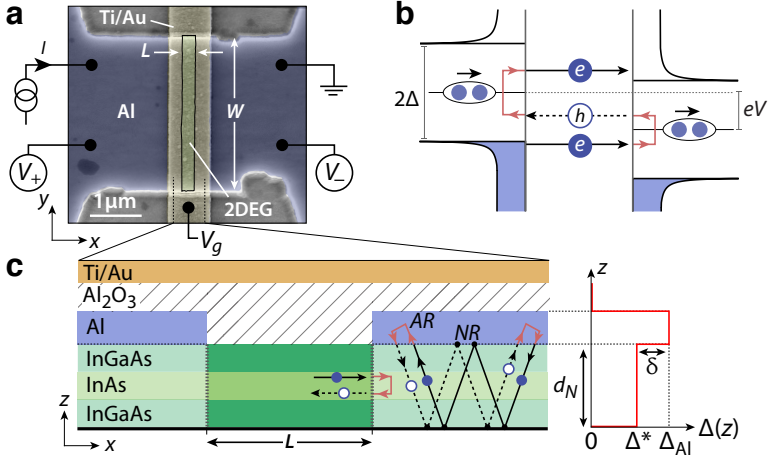


Figure 5.1: **Andreev reflection in an S-2DEG-S device.** (a) False-color scanning electron micrograph of the S-2DEG-S device. (b) Schematic of the 2nd order MAR process when a voltage $eV < \Delta$ is applied across an ideal SNS junction. (c) Cross-sectional schematic of the device in (a) (not to scale). Due to processes such as the one sketched in the schematic, involving multiple Andreev reflections (ARs) and potentially also normal reflections (NRs), the part of the quantum well covered by Al gains an induced gap Δ^* . Andreev reflection of particles in the uncovered region happen at the vertical *effective* interface, indicated by the gray, vertical dashed line, stemming from the gap Δ^* in the quantum well. Right schematic indicates variation of superconducting gap $\Delta(z)$ in the growth direction, for the case of an effective quantum well thickness much less than the normal-state coherence length, $d_N \ll \xi_N$ (see text for details), in the part of the quantum well covered by Al.

All measurements were performed in a dilution refrigerator with base temperature $T \sim 30$ mK using standard DC and lockin techniques, with current excitation in the range 2.5 nA to 5 nA.

5.2 MULTIPLE ANDREEV REFLECTION

The theoretical approach to this system begins with the Octavio-Blonder-Tinkham-Klapwijk (OBTK) model for multiple Andreev reflections [162]. As originally formulated, this model assumes a well-defined voltage is dropped across the normal region (green rectangle in Fig. 5.1a), leading to the MAR process sketched in Fig. 5.2b. For a planar junction where the 2DEG extends *under* the Al (Fig. 5.1c), the voltage can also drop along the horizontal Al-2DEG interface. In the case of imperfect Al-2DEG transparency, this leads to smearing of the resonances arising from MAR [34, 163]. The OBTK model was later extended to account for the planar geometry [153], denoted *SNcNS*, where *c* is the semiconducting region in which the superconducting top layer has been removed. The *SN* electrodes, consisting of 2DEG with Al on top, are assumed to be disordered and in equilibrium, while the exposed 2DEG region of length *L* is assumed ballistic. The model yields a renormalized density of states in the 2DEG, with an induced gap, $\Delta^* < \Delta_{\text{Al}}$ determined by the quality of the interface between the quantum well and the Al [153].

Figure 5.2 shows differential conductance (left) and DC voltage (right), as a function of applied DC current, for two gate voltages. The inset in Fig. 5.2a shows a zoom-in indicating the excess current and critical current for $V_g = 0$ V. The critical current is $I_c = 1.77 \mu\text{A}$ yielding an $I_c R_n$ product of $165 \mu\text{eV}$, about 70% of the gap of the Al film, and a critical current density $J_c = I_c/W = 0.59 \mu\text{A}/\mu\text{m}$. The excess current, reflecting enhanced current through the junction due to Andreev reflection, is defined as the $V = 0$ intercept of a linear fit to $V(I)$ taken at $V \gg \Delta_{\text{Al}}/e$ (green dashed line in Fig. 5.2a). The measured excess current, $I_{\text{exc}} =$

$1.44 \mu\text{A}$, corresponds to $I_{\text{exc}}R_n = 140 \mu\text{eV}$ ¹. The differential conductance (red curve in Fig. 5.2a) shows a series of peaks/dips as the current is increased. The peak/dip structure is a manifestation of the MAR processes and is expected to follow the series $eV = 2\Delta/n$, with $n = 1, 2, 3, \dots$ corresponding to the number of Andreev reflections.

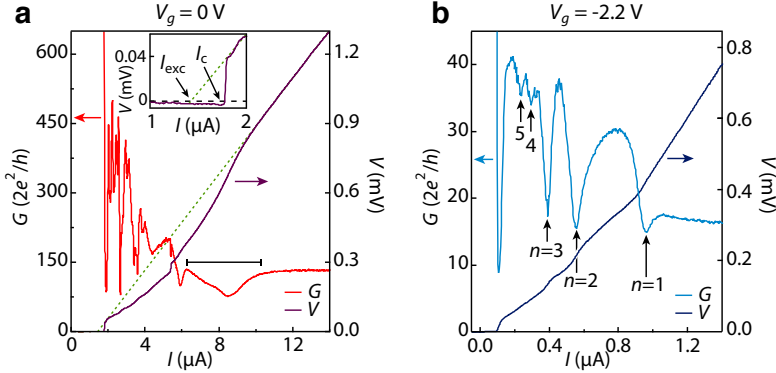


Figure 5.2: Differential conductance (left axis) and voltage (right axis) at two different gate voltages. In (a), the dashed green line shows linear fit at $eV(I) \gg \Delta_{\text{Al}}$, used to extract the excess current, I_{exc} , as the intercept with the $V = 0 \text{ mV}$ (as shown in the inset). I_c is the current at which the system switches to a resistive state. The dips highlighted in (b) correspond to multiple Andreev reflections of order n .

However, a broad dip in conductance, highlighted with black horizontal bar in Fig. 5.2a, occurs at energies larger than 2Δ but follows the temperature dependence of I_c and disappears at T_c , indicating that the feature has a superconductive origin. Such anoma-

¹ The excess current is related to the gap via $I_{\text{exc}} = \alpha\Delta/eR_n$, where $\alpha = 8/3$ in the ballistic, fully transparent case [55], and $\alpha = (\pi^2/4 - 1)$ in the diffusive case [164].

lous resistance features are believed to be associated with the planar Josephson junction geometry [99, 165], where quasiparticles in the 2DEG can undergo several scattering events at the Al interface before ultimately undergoing Andreev reflection and traversing the same path back. On a length scale smaller than the normal-state coherence length $\xi_N = \hbar v_F / k_B T$, this process will appear as Andreev reflection from an *effective* boundary, indicated by the gray vertical dashed line in Fig. 5.1c. The finite-bias properties of such systems cannot be adequately described by either the SNcNS or OBTK models, and the simple picture in Fig. 5.1b breaks down. With the contacts out of equilibrium, the position of the peaks in Fig. 5.2a cannot be directly related to the superconducting gap. However, by increasing the resistance in the exposed region relative to the horizontal interface, the peaks at finite-bias follow a regular series and can be used to extract a value for the induced gap.

In Fig. 5.2(b), the gate covering the exposed 2DEG region is energized to $V_g = -2.2$ V, substantially depleting the junction, leading to a normal state resistance $R_n = 740 \Omega$. At this gate voltage, the broad conductance dip at energies $eV > 2\Delta_{Al}$ is absent, and the DC voltages of the first three peaks (indicated with vertical black arrows) are positioned proportional to $1/n$, indicating that the voltage drop now occurs predominantly in the 2DEG region not covered by Al. At this gate voltage $I_c R_n$ is reduced from the $V_g = 0$ value. As we show below, the IV curves in Fig. 5.2 are consistent with near unity transmission through an SNcNS junction.

In highly transparent junctions, the resonances due to MAR appear as dips in the differential conductance, as opposed to the often used peaks. This subtle point can be appreciated by considering the nature of the current in a Josephson junction at finite voltages. In general, the current is a combination of the number of Andreev reflections, n , and the transmission τ of the junction. For the n 'th order Andreev reflection, the particle traverses the normal region

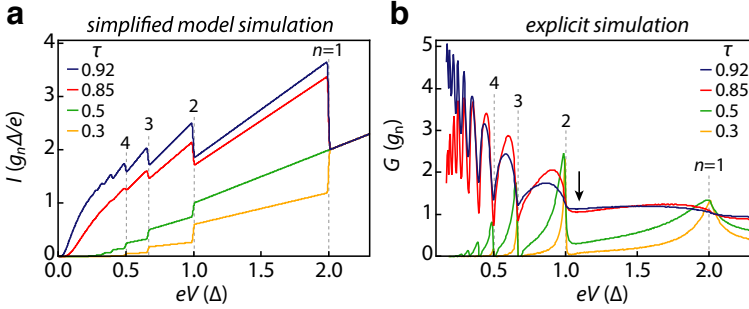


Figure 5.3: (a) Current through an SNS-junction, from the simplified model of Eq. (5.1), in units of $g_n \Delta/e$ (g_n is the normal state conductance), for several values of transmission through the junction. (b) conductances of an SNS-junction calculated using scattering approach for different values of the transparency τ . The vertical black arrow indicates the position of the conductance dip discussed in detail in Sec. 5.4.

$n + 1$ times, and neglecting the energy dependence of Andreev reflection probability, the current will depend on transmission as,

$$I(V) \sim (n + 1)\tau^{n+1}V. \quad (5.1)$$

For low τ , the current thus decreases rapidly for higher order Andreev reflection processes (*i.e.* increasing n). In contrast, for very transparent interfaces, higher order Andreev reflections will still yield an appreciable contribution to the current. This situation is demonstrated in Fig. 5.3(a), where we show the current in an SNS device, calculated according to Eq. 5.1. For low transparencies, the slope of the I versus V curves *increases* as n decreases and the current is increased at the transition from n to $n - 1$ Andreev reflections. As a result, the conductance of opaque junctions forms a staircase-pattern that increases in voltage with peaks at the sub-gap features (*cf.* the conductance depicted with the blue and green

curves in Fig. 5.3b, calculated using the model of Ref. [157]). In contrast, in the transmissive junctions, the current curve exhibits an opposite pattern, which results in a declining staircase-pattern in the conductance with the peaks replaced by dips (see the purple curve in Fig. 5.3(b)). This leads to an overall increase in the conductance *between* values of the voltage corresponding to integer multiples of the gap (*i.e.* at $V = 2\Delta/en$). Therefore, the vertical arrows in Fig. 5.2(b) point to local *minima*, not maxima, in conductance to indicate multiples of the gap, arising from the relation $V = 2\Delta/en$.

5.3 ELECTROSTATIC GATE DEPENDENCE

To extract the value of Δ^* , we plot the conductance from Fig. 5.2 against the DC voltage drop, as shown in Fig. 5.4(a). The theoretical MAR resonances in Fig. 5.4(a) are simulated using a generalized scattering matrix approach developed for SNS junctions [157, 166]. Within the model of an induced gap [153] the SNcNS system is interpreted as an effective S^*NS^* -junction, where S^* is the superconducting quantum well covered by Al, with a gap Δ^* and a critical temperature identical to that of the parent superconductor. Simulations are performed by calculating the conductance $G^{(\tau)}(V)$ of a single mode with transmission τ , from the DC component of the current $I^{(\tau)}(V, t) = \sum_{\mathbf{k}} I_{\mathbf{k}}^{(\tau)} \exp(2i\mathbf{k}eVt/\hbar)$. The time-independent Fourier component of $I_{\mathbf{k}}$ is calculated from the wave functions of the quasiparticles accelerated by the voltage V across the junction. In the case of a ballistic junction ($L < l_e$), the back-scattering effectively only occurs at the boundary between S^* and N (dashed white line in Fig. 5.1c). The total current through the junction is the sum of currents carried by N modes in M subbands. The resulting conductance through the multimode junction is given by $G(V) = \sum_i^M N_i G^{(\tau_i)}(V)$ where N_i is the number of modes in the

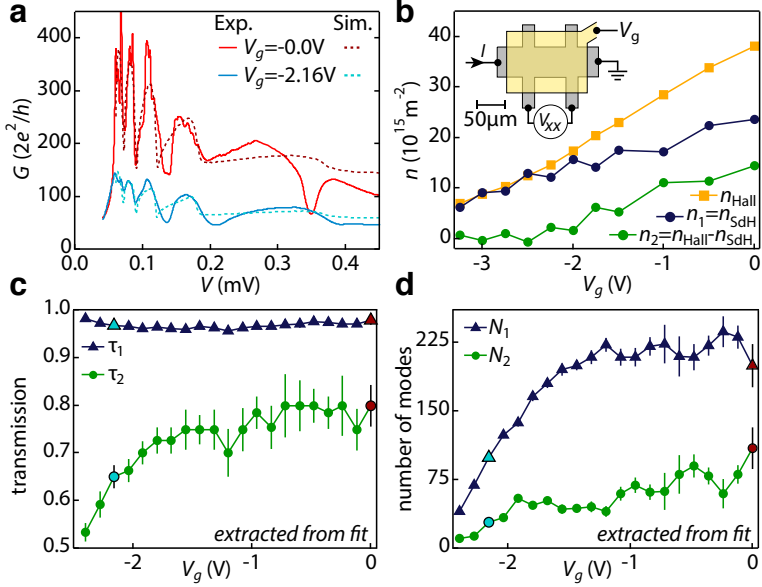


Figure 5.4: (a) Conductance as a function of bias voltage at two different gate voltages exhibiting resonances due to MAR. (b) Density in the 2DEG extracted from Hall slope and power spectrum of Shubnikov-de Haas oscillations versus gate voltage (See text for details). (c),(d), Transparency, τ_i , and number of modes, N_i , in subband i , as a function of top gate voltage V_g , extracted from the MAR data in (a). The red and teal points correspond to the fitting values used for the dashed curves in panel (a).

i 'th subband, and τ_i is the transmission of the modes in the i 'th subband.

A nonlinear least-squares procedure is used to fit simulated $G(V)$ curves to the data in Fig. 5.4b, where τ_i , Δ^* and N are fitting parameters and M is predefined (see also [167]). The minimal number of subbands needed to capture the essential features of the data was

found to be $M = 2$. For $M > 2$ the optimal fit did not populate the $i > 2$ subbands (i.e. $N_i \sim 0$ for $i > 2$), indicating that the data is well described by two subbands. The result of fitting to the MAR features at two V_g values are shown as dashed curves in Fig. 5.4(a). At $V_g = 0$, the induced gap was $\Delta^* = 182 \mu\text{eV}$ with $N_1 = 199$, $N_2 = 109$, $\tau_1 = 0.98$, and $\tau_2 = 0.8$. When the gate is energized to $V_g = -2.2 \text{ V}$ the fitting values are $\Delta^* = 180 \mu\text{eV}$, with $N_1 = 100$, $N_2 = 29$, $\tau_1 = 0.97$, and $\tau_2 = 0.65$. The gate-voltage dependence of the fitting parameters τ_i and N_i are shown in Figs. 5.4(c) and 5.4(d). The gap Δ^* extracted from the fitting routine is identical to the one measured in a tunneling experiment on the same wafer [156].

The presence of two transmission species in the optimal fit is attributed to the 2DEG having two occupied subbands. The carrier density in the 2DEG, denoted n_{Hall} , is measured in a Hall bar geometry via the Hall slope (shown in Fig. 5.4b). The density from the Hall slope is compared to the density extracted from the periodicity of the SdH oscillations in an out-of-plane magnetic field. The data in Fig. 5.4(b) show the density change in the 2DEG as the top gate is energized. The power spectrum of $\rho_{xx}(1/B)$ exhibit a two peak structure, indicating two subbands with different densities in the quantum well at $V_g = 0 \text{ V}$ [168]. The density corresponding to the major peak is denoted n_1 , and the difference $n_{\text{Hall}} - n_1$ is denoted n_2 . The density in the two subbands changes as the topgate is energized, as shown in Fig. 5.4(b), similar to N_1 and N_2 extracted from fitting to the MAR features. In particular, the N_2 species becomes depopulated at a gate voltage similar to the depletion of the second subband in the Hall bar (Fig. 5.4(b)). The decrease of transmission of the $i = 2$ species in Fig. 5.4(c) could be due to a breakdown of the ballistic assumption as the second subband is depleted.

Within the 1D Blonder-Tinkham-Klapwijk (BTK) formalism for an SN interface, the transparency is often parametrized using the

dimensionless quantity Z , related to the transmission via $\tau^{-1} = (1 + Z^2)$ [55]. For the first subband we extract an average transmission $\bar{\tau}_1 \gtrsim 0.97$, corresponding to a Z -parameter of $Z_1 \lesssim 0.18$. This indicates that the effective interface between the uncovered quantum well and the region covered by Al is pristine.

5.4 ELUCIDATING THE INDUCED GAP

The distinction between a BCS-like gap, Δ_{Al} , and an induced gap, Δ^* , is revealed through the temperature dependence of the superconducting properties. In the case where the effective thickness of the quantum well is much less than the normal-state coherence length, $d_{\text{N}} \ll \xi_{\text{N}}$, any position-dependence of the gap magnitude in the growth direction in the 2DEG can be neglected, and the temperature dependence of the induced gap depends on Δ_{Al} according to [84, 153, 169]

$$\Delta^*(T) = \frac{\Delta_{\text{Al}}(T)}{1 + \gamma_{\text{B}} \sqrt{\Delta_{\text{Al}}^2(T) - \Delta^{*2}(T)}/\pi k_{\text{B}} T_c}, \quad (5.2)$$

where $\Delta_{\text{Al}}(T)$ is determined self-consistently from BCS theory. The dimensionless parameter γ_{B} is a measure of the horizontal SN interface transparency (black, dashed line in Fig. 5.1(c)), where $\gamma_{\text{B}} = 0$ corresponds to a perfectly transparent interface [87]. The parameter γ_{B} represents the discontinuity in the superconducting pair-potential and gives rise to the difference between the gap in aluminum, Δ_{Al} , and the induced gap, Δ^* , in the 2DEG, denoted δ in Fig. 5.1(c). For the present case we find $\gamma_{\text{B}} = 0.87$, using $\Delta^* = 180 \mu\text{eV}$ and $\Delta_{\text{Al}} = 237 \mu\text{eV}$, consistent with a high quality interface between the quantum well covered by Al, and the Al itself.

To elucidate the nature of the induced superconducting gap, we study the temperature dependence of the differential conductance

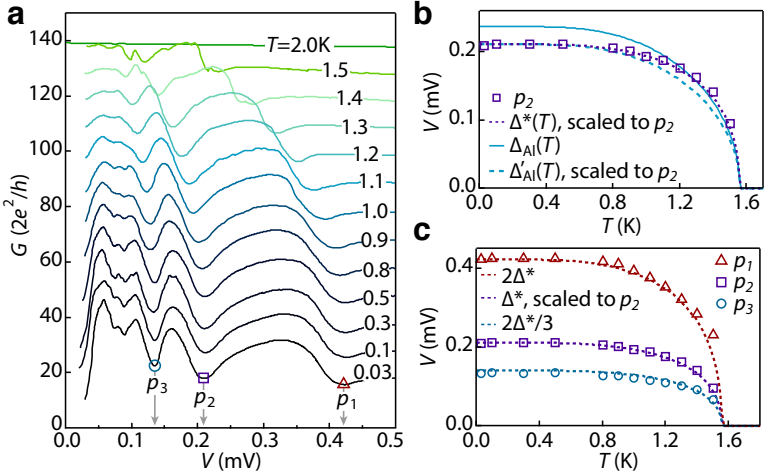


Figure 5.5: (a) Temperature dependence of the MAR features at $V_g = -2.2$ V. Traces successively offset by $10 \ 2e^2/h$. (b) Temperature dependence of the dip labeled p_2 . Dashed purple line is Eq.(5.2) scaled to match p_2 at base temperature. Solid teal line is temperature dependence of a BCS superconducting gap, and dashed teal line is a rescaling of $\Delta_{Al}(T)$, to match p_2 at base temperature. (c) Temperature dependence of first, second, and third dip positions, with multiples of $\Delta^*(T)$ from (b).

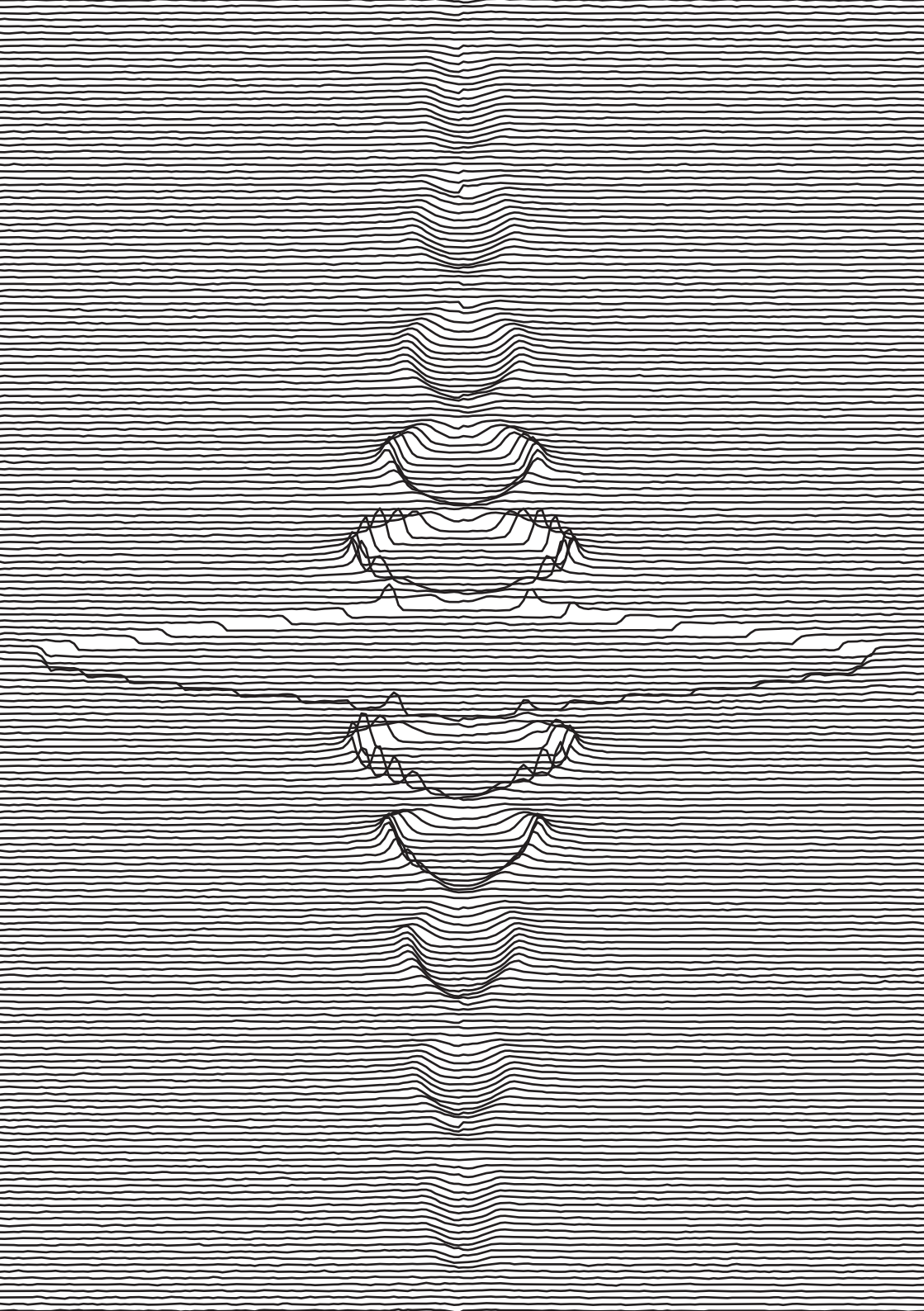
at $V_g = -2.2$ V, shown in Fig. 5.5(a). The position of the second MAR related dip (denoted p_2) is tracked in Fig. 5.5b as the temperature is increased. The curves in Fig. 5.5(b) show the solution of Eq. (5.2) (purple), temperature dependence of a BCS gap, $\Delta_{Al}(T)$, (teal), and a BCS-like gap, $\Delta'_{Al}(T)$, (teal, dashed), where the gap value has been rescaled to coincide with the data at $T = 30$ mK. The inadequacy of the temperature dependence of a BCS-like gap (both unscaled and rescaled) to account for the temperature dependence of the peaks is contrasted by the good correspondence

between Eq. (5.2) and our data. The temperature dependence of the first and third dip positions, p_1 and p_3 , are shown in Fig. 5.5c. The curves identified with p_1 and p_3 are found by multiplying $\Delta^*(T)$ by a factor of 2 and $2/3$, respectively, corresponding to $n = 1$ and $n = 3$ in the $2/n$ MAR series.

The small deviation between $V(p_2) \sim 0.21$ meV, which one might expect was located at $V = 2\Delta^*/(2e) = \Delta^*/e$, and the gap extracted from the fitting in Section 5.3 ($\Delta^* \sim 0.18$ meV) can be understood by again appealing to the simulation in Fig. 5.3(b). There, the black vertical arrow show the minimal conductance close to the $n = 2$ MAR resonance, which does not coincide exactly with Δ/e . From the simulation, we see that the voltage difference from the resistance maxima at the vertical arrow and the gap is approximately $\sim 10\%$, in good agreement with $V(p_2)$ and Δ^* which differ by $\sim 14\%$. Regardless, the correspondence between the temperature dependence of MAR features and temperature dependence of the gap is unchanged by this effect and the excellent agreement also with $n = 1$ and $n = 3$ resonances indicate that the superconducting properties of the junction are well described within the induced gap model.

5.5 CONCLUSION

In conclusion, we have measured MAR resonances in a Josephson junction in a InAs 2DEG heterostructure, where aluminum is epitaxially matched to the 2DEG. By fitting the conductance of the MAR features, we extract a transmission close to unity through an effective S^*NS^* -junction, where S^* represents the InAs quantum well covered by the Al. The temperature dependence of the MAR resonances is well-described by the theory of an effective induced gap, and we find $\Delta^* = 180 \mu\text{eV}$ in the 2DEG region covered by Al, close to the gap of the Al itself, indicating a transparent interface between the two.



ANOMALOUS FRAUNHOFER INTERFERENCE

In this chapter we investigate patterns of critical current as a function of perpendicular and in-plane magnetic fields in superconductor-semiconductor-superconductor (SNS) junctions based on InAs/InGaAs heterostructures with an epitaxial Al layer. Thin epitaxial Al allows the application of large in-plane field without destroying superconductivity. For fields perpendicular to the junction, flux focusing results in aperiodic node spacings in the pattern of critical currents known as Fraunhofer patterns by analogy to the related interference effect in optics. Adding an in-plane field yields two further anomalies in the pattern. First, higher order nodes are systematically strengthened, indicating current flow along the edges of the device, as a result of confinement of Andreev states driven by an induced flux dipole; second, asymmetries in the interference appear that depend on the field direction and magnitude. A model is presented, showing good agreement with experiment, elucidating the roles of flux focusing, Zeeman and spin-orbit coupling, and disorder in producing these effects.

Superconductor-normal-superconductor (SNS) junctions form a well-established platform to study the properties of superconducting hybrid structures. SNS junctions based on semiconductors with strong SOI have been proposed to study the topological phase transition [171–174], but could also potentially be used to quantify the strength of SOI in the semiconductor [175]. For instance, theoretical models have been developed to understand how the detailed SNS current-phase relation depends on SOI in two-dimensional junc-

Adapted from [170]

tions [176], as well as in single-channel junctions [177], quantum point contacts [178, 179], and nanowires [180].

Many details of the physics occurring in the junction are also encoded in the critical current. A measurement of the critical current as a function of the out-of-plane magnetic field B_z is paradigmatic in the study of SNS junctions. For increasing B_z , the winding of the superconducting phase by the enclosed flux leads to a characteristic modulation of the critical current I_c . For a rectangular junction with uniform current density

$$I_c(B_z) = I_c^{(0)} \left| \frac{\sin(\pi B_z L W / \Phi_0)}{(\pi B_z L W / \Phi_0)} \right|, \quad (6.1)$$

reminiscent of a single-slit Fraunhofer interference pattern in optics [54]. Here, L and W are the length and width of the normal region, $I_c^{(0)}$ is the zero-field critical current, and $\Phi_0 = h/2e$ is the flux quantum. This behavior has been observed in a wide variety of systems [79, 181] including 2DEGs with strong SOI [80]. Deviations from this Fraunhofer form can yield information about the local magnetic field profile [182] as well as the supercurrent density in the junction [120, 183]. Recently, such interference mapping has been used to probe edge states arising in two-dimensional topological insulators [184–186] and graphene [167].

In this chapter, we present an experimental and theoretical study of the magnetic field dependence of the interference pattern of critical currents in epitaxial Al/InAs/Al junctions, with both perpendicular field as well as a separately controlled in-plane field. We identify several interesting effects: (i) In a purely perpendicular field, we observe a deviation from a simple Fraunhofer pattern (Eq. (6.1)), which we interpret as arising from flux focusing due to the Meissner effect in the epitaxial Al leads. (ii) The interference pattern changes dramatically when an in-plane field is applied. A crossover is observed in the perpendicular-field interference pattern with increasing in-plane field, from a Fraunhofer-like pattern

with rapidly decreasing critical currents with node index, toward one resembling that of a superconducting quantum interference device (SQUID) with critical currents that depend only weakly on node index. We interpret this transition as again resulting from flux focusing: When the *in-plane* flux is excluded from the leads, an effective *out-of-plane* flux dipole appears in the junction region. This dipole dephases contributions to the supercurrent in the center of the junction, resulting in coherent transport only near the edges of the sample. (iii) Application of an in-plane field also induces striking asymmetries (upon reversing perpendicular field) in the interference pattern that depend on the magnitude and direction of the in-plane field, but also vary strongly from lobe to lobe and from sample to sample. Based on these observations, we conclude that flux focusing plays a key role in planar epitaxial devices, particularly in the presence of an in-plane field. Indeed, field modulations due to flux focusing may prove useful, for instance providing magnetic confinement of Andreev states. In the present devices, observation (iii)—asymmetries in the interference pattern—are dominated by disorder effects, masking related effects due to spin-orbit and Zeeman coupling.

The chapter is organized as follows: [Section 6.1](#) provides details on device fabrication and magnetotransport measurements. [Section 6.2](#) describes the behavior of the junction with a purely perpendicular magnetic field. [Section 6.3](#) describes junction behavior when the applied field is purely in-plane. [Section 6.4](#) reports effects of combined perpendicular and in-plane fields. Conclusions and open questions are discussed in [Section 6.5](#).

6.1 METHODS

Characterization of the epitaxial Al film yielded a superconducting transition temperature of $T_c = 1.5$ K, and collapse of superconductivity at an out-of-plane critical field $B_{z,c} \sim 30$ mT, and an

in-plane critical field $B_{r,c} \sim 1.6$ T (c.f. [Figure 4.5](#)). Separate transport measurements of the InAs quantum well (QW) with Al removed demonstrated an electron density of $n_e = 3.8 \times 10^{16} \text{ m}^{-2}$ and mobility $\mu = 0.43 \text{ m}^2\text{V}^{-1}\text{s}^{-1}$ at zero gate voltage, yielding a mean free path $l_e = 140$ nm. In this density regime, two QW subbands are occupied, as determined by magnetotransport measurements. Upon partially depleting the 2DEG with the top gate, the single subband limit is reached at gate voltage $V_g < -2.0$ V with a mobility peak $\mu = 0.7 \text{ m}^2\text{V}^{-1}\text{s}^{-1}$ for $n_e = 1.9 \times 10^{16} \text{ m}^{-2}$. The data presented in [Secs. 6.2 to 6.4](#) were all obtained with $V_g = 0$. Occupation of the second subband appears to play only a minor role in all device characteristics (c.f. [B.1](#)). Measurements on similar QWs have demonstrated large SOI, characterized by a spin-orbit length $l_{\text{so}} \sim 45$ nm [[151](#)]. The superconducting coherence length is estimated as $\xi = \hbar v_F / \Delta^* = 1.3 \text{ } \mu\text{m}$ ¹, with v_F the Fermi velocity and the induced superconducting gap $\Delta^* \sim 180 \text{ } \mu\text{eV}$ as determined from tunneling measurements presented in [Chapter 4](#).

Measurements were performed on six SNS devices, all of which showed qualitatively similar behavior (c.f. [Figure B.4](#)). The data in [Section 6.2](#) through [Section 6.4.1](#) were characteristic of all devices. Data similar to those presented in [Section 6.4.2](#) were obtained from several samples but with broad quantitative variation, as discussed below. We focus on data from one SNS junction with contact separation, $L = 450$ nm, and lateral width, $W = 1.5 \text{ } \mu\text{m}$ in the regime $l_e < L < \xi$ (see [Figure 6.1\(a\)](#)). The junction is oriented such that the current flows along the [011] orientation of the underlying crystal structure.

Throughout, we define the x -direction as in the plane of the electron gas and parallel to the average current flow, and the y -direction as in plane and perpendicular to average current flow. The inset in [Figure 6.1\(a\)](#) shows the corresponding components of the applied magnetic field \mathbf{B} .

¹ An effective mass of $m_{\text{eff}} = 0.05 m_e$ is estimated from k.p calculations

To avoid effects of hysteresis as a function of I [187] and B_z [188], measurements as in Fig. 6.1(c) were obtained by merging the four quadrants separated by white dashed lines, each taken separately by sweeping current and field away from zero.

6.2 PERPENDICULAR MAGNETIC FIELD

Sweeping the bias current I over a range of perpendicular magnetic fields B_z while measuring the differential resistance R results in the interference pattern shown in Figure 6.1(c). This pattern deviates from the expected Fraunhofer form predicted by Eq. (6.1). For instance, from Eq. (6.1) we expect equally spaced nodes of the critical current, at values of perpendicular field $B_z = n\Phi_0/(WL)$, where integer numbers of flux quanta penetrate the semiconductor region. Experimentally, we find a deviation from this uniform node spacing, as can be seen from the vertical dashed lines in Figure 6.1(c).

In order to investigate this variable node spacing in more detail, we plot in Figure 6.1(e) the critical current extracted from Figure 6.1(c) as a function of B_z (markers). For reference, we also show the expected Fraunhofer pattern (green) using the lithographic device area, for which $\Phi_0/(WL) = 3.1$ mT. From the data, we find a central lobe half-width of 0.97 mT and a reduced spacing of the subsequent side-lobes, gradually increasing and reaching 1.9 mT for the fifth side-lobe ².

² The deviation at high field between our result and the expectation is presumably due to an underestimation of the junction area due to the neglect of the finite penetration depth in the leads [189]. Utilizing an effective length $L_{\text{eff}} = L + 2\lambda_L$ (with λ_L estimated in Section B.1) yields an expected node spacing of 1.7 mT.

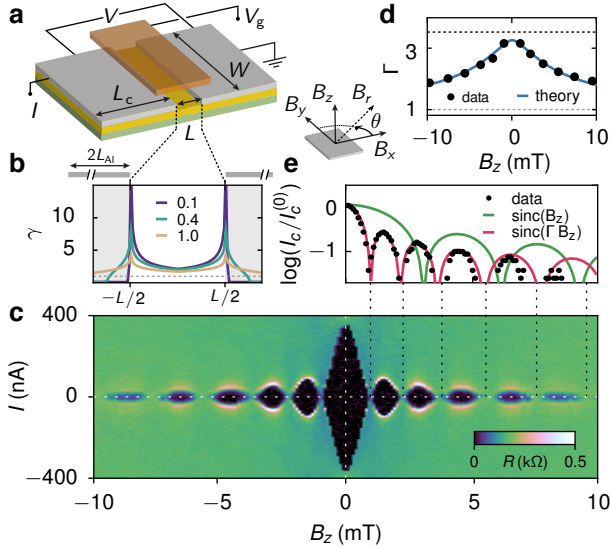


Figure 6.1: **SNS device schematic and Fraunhofer**, (a) Device and measurement schematic illustrating the extended superconducting Al banks (gray), InAs quantum well (yellow), and InGaAs barrier (green). The top gate (orange) is shown suspended above the junction, for clarity we have omitted the intervening ALD layer. L and W denote the junction length and width respectively. L_c indicates the physical aluminum contact length. The coordinate system is illustrated in the inset. (b) Local magnetic-field focusing parameter γ as a function of position x for three different ratios $\beta = B_z/B_f$. On the upper horizontal axis we highlight $2L_{Al}$, the contact length entering the model. (c) Differential resistance R , as a function of bias current I and perpendicular magnetic field B_z . (d) Total magnetic field enhancement in the junction Γ as a function of B_z , calculated by extraction of the nodes visible in (c,e) (markers), and a fit using Eqs. (6.3) to (6.6) (solid line). (e) Critical current I_c , plotted logarithmically to highlight periodicity, extracted from (c) (markers). Overlaid are the expectation of Eq. (6.1) (green) and the modified form taking into account field enhancement due to flux focusing (red).

To quantify the deviation from the expected uniform spacing, we introduce a dimensionless factor Γ , the ratio of the expected node position to the observed node position,

$$\Gamma(B_z^{(n)}) = \frac{n\Phi_0}{B_z^{(n)}LW'}, \quad (6.2)$$

where $B_z^{(n)}$ is the perpendicular magnetic field at node number n . A regular Fraunhofer pattern has $\Gamma = 1$ everywhere, as indicated in [Figure 6.1\(d\)](#). At low fields, we find $\Gamma \sim 3$. As B_z increases, Γ decreases, approaching unity at high fields. The black dots in [Figure 6.1\(d\)](#) show the extracted Γ based on the data of [Figure 6.1\(c\)](#).

The deviation from [Equation 6.1](#) leading to $\Gamma > 1$ can be understood as resulting from field-dependent flux focusing from the superconducting contacts. The qualitative behavior of Γ is consistent with the superconducting leads passing from a Meissner state at low field, through a mixed state, towards a fully flux-penetrated state above 10 mT. In the Meissner state, the contacts completely expel flux, causing the field in the junction region to be enhanced. When the magnetic field is increased, the thin aluminum banks are slowly pushed into a mixed state as they are penetrated by field lines, leading to a smaller field enhancement in the junction and correspondingly a decreasing Γ . At high field the banks are presumably fully penetrated by the incident flux, approaching a negligible field enhancement and $\Gamma \approx 1$.

Previous studies using thick niobium contacts also found large field enhancements in SNS junctions [[190](#), [191](#)]. In those studies, however, the leads remained in a full Meissner regime for the perpendicular field range studied, resulting in a constant field enhancement. Because the Al electrodes in the present system are operated close to their critical field B_c , the degree of flux focusing depends on field.

To examine the flux-focusing picture more quantitatively, we model the field profile inside the junction following Ref. [[192](#)] (see

also [188]). The effective field near a single thin superconducting strip of length $2L_{A1}$ and infinite width (see Figure 6.1(b)), subject to a perpendicular applied field, is given by

$$B_{\text{eff}}(\tilde{x}) = B_f \log \left(\frac{|\tilde{x}| \sqrt{L_{A1}^2 - a^2} + L_{A1} \sqrt{\tilde{x}^2 - a^2}}{a \sqrt{|\tilde{x}^2 - L_{A1}^2|}} \right), \quad (6.3)$$

for $|\tilde{x}| > a$ and $B_{\text{eff}}(\tilde{x}) = 0$ for $|\tilde{x}| \leq a$. The coordinate \tilde{x} is the in-plane coordinate perpendicular to the edges of the film, with $\tilde{x} = 0$ corresponding to the center of the film. The length $2a$ corresponds to the extent of a region centered at $\tilde{x} = 0$ where the field is fully expelled due to Meissner screening; this length is given by $a = L_{A1} / \cosh(B_z / B_f)$, with B_z the applied perpendicular magnetic field³ and B_f a characteristic field scale roughly corresponding to the field of first vortex penetration. To account for the finite width of our junction, we argue that $2L_{A1}$ in this case corresponds not to the physical contact length L_c (see Figure 6.1(a)), on the order of 10 μm , but to an effective length over which flux is focused into the junction. Flux lines further away than $\sim W$ from the junction edge are more likely to be expelled towards the sides rather than into the junction region. We thus use W as a cutoff for the effective contact length and set $L_{A1} = W$.

To account for both contacts in our SNS geometry, we approximate the total effective perpendicular field profile as

$$B_{\text{tot}}(x) = B_{\text{eff}}(L_{A1} + L/2 - |x|), \quad (6.4)$$

expressed in terms of the x -coordinate with $x = 0$ corresponding to the center of the SNS junction. We thus make the simplification that the focusing in the junction is dominated by the left(right)

³ For $B_z > B_f$, $B_{\text{eff}}(\tilde{x}) \propto B_z$. Indeed for large \tilde{x} we find $B_{\text{eff}}(\tilde{x}) = B_f \log \left(\cosh \left(\frac{B_z}{B_f} \right) \left[1 + \tanh \left(\frac{B_z}{B_f} \right) \right] \right) = B_z$.

contact for negative(positive) x . We then use Eqs. (6.3) and (6.4) to define a local field enhancement parameter

$$\gamma(\beta, x) = B_{\text{tot}}(x)/B_z, \quad (6.5)$$

which is a function of the ratio $\beta = B_z/B_f$. In Figure 6.1(b) we plot γ for three different β , illustrating the inhomogeneous field profile induced by the superconducting leads. The dashed line in Figure 6.1(b) highlights the expectation in the absence of focusing ($\gamma = 1$). Near zero applied field (blue line), the local enhancement peaks strongly close to the superconducting banks. Inside of the superconducting contacts, however, γ abruptly falls to zero. When the field is increased (cyan and gold lines) we see a gradual smoothing of the enhancement profile as more of the flux penetrates the superconducting banks.

Integrating Eq. (6.5) over the junction length allows us to calculate the total field enhancement,

$$\Gamma(B_z) = \frac{1}{L} \int_{-L/2}^{L/2} \gamma(\beta, x) dx. \quad (6.6)$$

We fit the data using Eq. (6.6) with B_f as the only free parameter. The resulting fit is shown as the blue line in Figure 6.1(d), yielding $B_f = 8.2$ mT. This is in good agreement with an estimate for the field of first vortex penetration of the film $B_{c1} = 7.7$ mT (see B.1). Besides, detailed calculations for a finite-width geometry predict a low-field enhancement of $\Gamma = (2W/L)^{2/3} \sim 3.5$ as shown by the black dashed line in Figure 6.1(d) [193]. The good agreement between this low-field prediction and our model further supports our approximation $L_{A1} = W$. The resulting continuous function $\Gamma(B_z)$ can then be used to plot the full interference pattern of $I_c(B_z)$, corrected for the flux focusing due to the presence of the superconducting contacts. The resulting $I_c(B_z)$ is plotted in red in Figure 6.1(e), and shows excellent agreement with the $I_c(B_z)$ extracted from Figure 6.1(c).

Despite its simplicity, our model captures the observed deviations from a regular Fraunhofer pattern in the interference pattern of critical currents, strongly suggesting that the observed aperiodic node spacings are indeed caused by flux focusing in the mixed state of the superconducting leads where $B_z \sim B_{c1}$. As a control experiment we have also studied a device of nominally identical dimensions, but with large flux holes located behind the superconducting contacts. Consistent with our interpretation, negligible field enhancement is observed in this device, independent of the applied field (c.f. [Figure B.3](#)).

6.3 IN-PLANE MAGNETIC FIELD

We next examine the effects of in-plane magnetic field on the SNS junction, initially without perpendicular field, $B_z = 0$. Differential resistance as a function of bias current and field magnitude is shown in [Figure 6.2](#) for two field orientations: field parallel to the current (x -direction, [Figure 6.2\(a\)](#)) and field perpendicular to the current (y -direction, [Figure 6.2\(b\)](#)). We see that the critical current exhibits a strong anisotropy. The critical field (where the supercurrent becomes fully suppressed) changes from ~ 200 mT for $\mathbf{B} \parallel \hat{x}$ to ~ 650 mT for $\mathbf{B} \parallel \hat{y}$. In [Figure 6.2\(d\)](#) we show the full dependence of I_c on the direction of the in-plane field, where we fixed the magnitude of the field to $B_r = 150$ mT and θ denotes the angle between \mathbf{B} and the x -direction.

We propose to interpret this anisotropy again in terms of flux focusing due to the Meissner effect. Indeed, also an in-plane field could give rise to flux focusing, since the thickness of the Al layer ($d \sim 10$ nm) is comparable to the London penetration depth of Al, $\lambda_L = 16$ nm [[142](#)].

One consequence of the in-plane Meissner effect would be that the density of flux lines just below the aluminum contacts increases, leading to local enhancements of the effective field inside the QW.

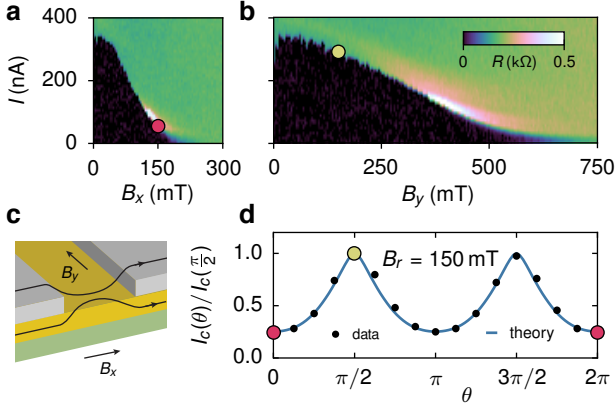


Figure 6.2: **Supercurrent in-plane magnetic field dependence**, (a) Differential resistance R , as a function of bias current I and in-plane magnetic field B_x , applied in the x -direction (along the direction of current flow). (b) As in (a) but with the in-plane field B_y along the y -direction. (c) Schematic indicating how an in-plane field along \hat{x} can result in an effective flux dipole in the normal region. (d) Normalized critical current I_c as a function of the angle θ between the in-plane field and \hat{x} ; the field has a fixed magnitude of $B_r = 150$ mT. The dots represent the experimental data, the solid line is a theory curve based on a one-parameter fit of α at $\theta = \pi$, using the model based on Eq. 6.7 (see below). The red and yellow markers highlight the correspondence with panels (a) and (b) respectively.

However, this focusing effect is not expected to depend strongly on the direction of the in-plane field. Another possible effect is that the bending of the field lines around the edges of the contacts may induce a flux dipole in the junction, as exaggerated schematically in Figure 6.2(c). Assuming that $\mathbf{B} \parallel \hat{\mathbf{x}}$, we see that close to the left contact there is a small component of flux inside the well in the positive z -direction, and close to the right contact there is a comparable component in the opposite direction. This flux dipole couples to the in-plane motion of the electrons and can therefore have a strong effect on the interference pattern of I_c . Furthermore, the effect is proportional to B_x only, and can thus lead to an anisotropy of I_c in the in-plane field direction.

For $\mathbf{B} \parallel \hat{\mathbf{y}}$ the suppression of the critical current with field appears to be fully accounted for by Zeeman effects only. Neglecting orbital effects, an estimate of the magnitude of the effective g -factor in the InAs QW from the critical field $B_{y,c}$ yields $|g^*| = 2\Delta^*/\mu_B B_{y,c} \sim 10$, which is in good agreement with previous measurements [151].

As soon as we let the in-plane field deviate from the y -direction, a flux dipole will be induced in the N region. The effect of this dipole is most easily understood within a semiclassical picture, where supercurrent arises from coherent transport of Andreev pairs between S regions along well-defined trajectories through the N region. A finite flux dipole makes the phase picked up along a trajectory depend explicitly on the angle ϑ between the trajectory and the x -axis. The dipole will therefore lead to a dephasing of contributions to the current arising from trajectories with different ϑ , and will thus suppress the supercurrent.

We develop a simple but quantitative model of supercurrent through an SNS junction in the presence of a flux dipole by assuming that the junction is ballistic and we can use a semiclassical approximation (where the Fermi wavelength is the smallest length scale in the problem). In the absence of a perpendicular field (or

for finite but small B_z) we can associate the Andreev bound states in the normal region with straight trajectories connecting the two proximitized regions in the QW. For the energy of such a bound state as a function of ϑ and the average y -coordinate y_0 one finds in the limit of $W, L \ll \xi$

$$E(y_0, \vartheta) = \pm \Delta^* \cos \left(\frac{\varphi}{2} - \pi \frac{\Phi}{\Phi_0} \frac{y_0}{W} - \pi \alpha \tan \vartheta \right), \quad (6.7)$$

where φ is the phase difference between the two proximitized regions, Φ is the homogeneous flux associated with B_z , and $\alpha = \alpha_0 \cos \theta$ depends on B_x and parametrizes the effect of flux focusing⁴. The contribution of all Andreev bound states to the free energy F of the junction is found by summing (6.7) over all allowed y_0 and ϑ , weighted by a Fermi function. The supercurrent then follows as $I_s(\varphi) = (2e/\hbar) \partial F / \partial \varphi$ and the critical current is simply $I_c = \max_{\varphi} I_s(\varphi)$.

We convert the sums over y_0 and ϑ into integrals and, assuming for simplicity zero temperature and fully absorbing sides at $y = \pm W/2$, we numerically compute the critical current for $\Phi = 0$ as a function of the in-plane field direction θ . Comparing the resulting $I_c(\theta)/I_c(\pi/2)$ with the data shown in Figure 6.2(d) results in a single-parameter fit yielding $\alpha_0 = 0.32 \pm 0.01$. The resulting fit is shown as the solid blue line in the figure and shows excellent agreement with the data. We can also try to connect this numerical value for α_0 to our device geometry. A rough estimate for α_0 in terms of device parameters is $\alpha_0 = \eta B_r L d_f / \Phi_0$, where d_f is the width of the strips close to the proximitized regions where flux focusing is significant and η is the fraction of B_x that locally contributes to magnetic flux oriented along $\pm \hat{z}$. We thus estimate that there is only a significant out-of-plane flux in two narrow strips

⁴ We note that this model neglects the effect of SOI. We have verified that spin-orbit effects, calculated along the lines of Ref. [176], yield changes on the order of a few percent while the experimental anisotropy is of the order 1.

of area $L \times d_f$ bordering the proximitized regions, and $0 \leq \eta \leq 1$ is a phenomenological parameter related to the average degree of bending of the flux lines. (For instance, $\eta = 1/\sqrt{2}$ would correspond to a situation where the flux lines make on average an angle of 45° with the plane of the junction within two strips of width d_f .) If we estimate $d_f = d = 10$ nm we find for $B_r = 150$ mT and $\alpha_0 = 0.32$ that $\eta = 0.29$, corresponding to an average local out-of-plane angle of $\sim 20^\circ$.

6.4 COMBINED PERPENDICULAR & IN-PLANE MAGNETIC FIELDS

Sweeping B_z while still applying an in-plane field we observe two new and striking effects, as shown in [Figure 6.3\(a,b\)](#). First, in the presence of an in-plane field, the critical current develops a pronounced asymmetry between positive and negative B_z ; we observe this for all directions of in-plane field. Second, increasing the in-plane field when directed along \hat{x} results in (i) a decrease of the zero-perpendicular-field critical current, $I_c^{(0)}$; (ii) a relative enhancement of all side-lobe maxima as compared to the central one, approaching a situation where all observable maxima are roughly equal; and (iii) a gradual decrease of the width of the central lobe. We initially focus on the latter effects, associated with B_x , and discuss the asymmetries in [Section 6.4.2](#).

6.4.1 *SNS-to-SQUID transition*

Both the narrowing of the central lobe and the gradual equalizing of lobe maxima with increasing B_x can be understood as resulting from the flux-focusing mechanism discussed in the previous section. As argued above, a large B_x could lead to a situation where the supercurrent in the center of the junction is suppressed and most transport takes place along the edges of the normal region,

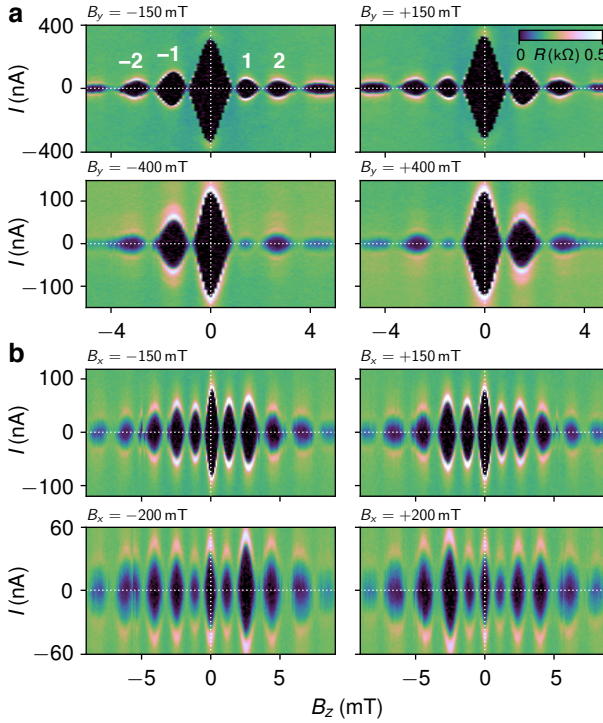


Figure 6.3: **In-plane field induced Fraunhofer asymmetry**, (a) Differential resistance R as a function of bias current I and B_z , measured for different values of fixed B_y : $B_y = \pm 150$ mT (upper row) and $B_y = \pm 400$ mT (bottom row). The white numbers in the upper left panel indicate the lobe indices. (b) As (a), for an in-plane magnetic field applied along \hat{x} , using $B_x = \pm 150$ mT (upper row) and $B_x = \pm 200$ mT (bottom row).

making the system more like a SQUID, with conduction only along sample edges, instead of a planar SNS junction with uniform current flow. In the pure-SQUID limit, one expects for the critical current $I_c(\Phi) \propto |\cos(\pi\Phi/\Phi_0)|$ instead of a Fraunhofer-like pattern, i.e., all lobes will have the same maximum value and the same width Φ_0 . This is qualitatively consistent with the trend we observe in [Figure 6.3\(b\)](#).

To further examine the picture of a focusing-induced flux dipole leading to SQUID-like current flow, we use the model from [Section 6.3](#) to calculate the critical current as a function of $\Phi = B_z LW$ for different focusing parameters α , and compare the resulting theoretical interference patterns $I_c(B_z)$ with experimental data ⁵.

In [Figure 6.4\(a\)](#), the calculated $I_c(B_z)$ is plotted for five values of α , corresponding to $B_x = 0, 100, 150, 200,$ and 300 mT (assuming for simplicity a linear relation between α and B_x , and setting $\alpha = 0.32$ for $B_x = 150$ mT). These numerical results reproduce the two main features discussed above: (i) As highlighted by the vertical gray dashed lines, the width of the central lobe decreases with increasing B_x . For $B_x = 0$ we find a width of roughly $2.6\Phi_0$ (slightly larger than the $2\Phi_0$, corresponding to a regular Fraunhofer pattern, presumably due to finite size effects ⁶), and for large B_x it approaches Φ_0 , the SQUID limit. (ii) The heights of all side-lobes in [Figure 6.4\(a\)](#) increase relative to the central lobe when increasing B_x , approaching a situation where all lobes are of comparable height. Both these trends are qualitatively consistent with

⁵ In this section we concentrate largely on qualitative features and thus for simplicity neglect the effect of out-of-plane focusing as discussed in [Section 6.2](#)

⁶ Close to the edges of the junction, where $y_0 \approx \pm W/2$, there are fewer angles ϑ available to construct Andreev bound states with. Consequently, the flux penetrating the N region close to the edges has less influence on the total average supercurrent through the junction than the flux penetrating the center of the region. To achieve the first full suppression of the supercurrent by perfect destructive interference of all trajectories, one thus needs to go to slightly higher fields than $B_z = \Phi_0/(WL)$.

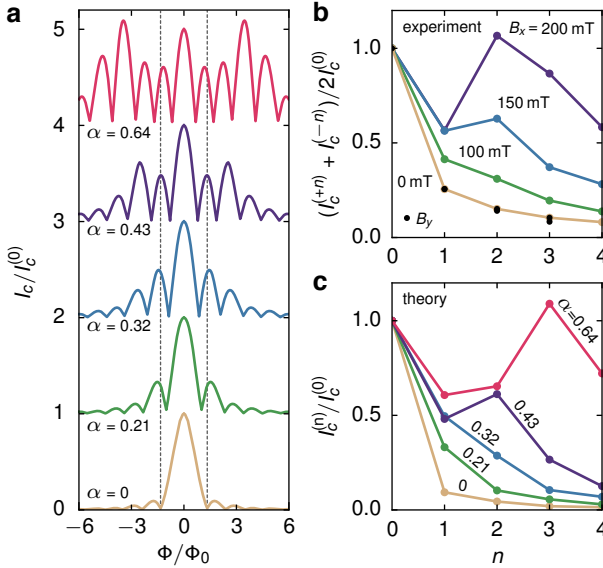


Figure 6.4: **Flux dipole induced SNS to SQUID transition**, (a) Numerically calculated critical current as a function of Φ , normalized by $I_c^{(0)}$. The in-plane field is assumed along \hat{x} and the different curves correspond to $\alpha = 0, 0.21, 0.32, 0.43$, and 0.64 , from bottom to top (each offset by 1). (b) Symmetrized side-lobe maxima extracted from experimental data, for different in-plane fields. The field magnitudes indicated in the plot refer to $\mathbf{B} \parallel \hat{x}$; all data points for $\mathbf{B} \parallel \hat{y}$ (black dots) fall on top of the set marked 0 mT. (c) Side-lobe maxima obtained from the numerical data shown in (a).

the experimental observations and support our interpretation in terms of a focusing-induced flux dipole.

We next examine the behavior of the sequence of side-lobe maxima for different B_x in more detail. In [Figure 6.4\(b\)](#) we show the experimentally obtained maxima for four different B_x , where we removed the complicating asymmetry in $\pm B_z$ (considered in detail below) by symmetrizing and normalizing the data, $(I_c^{(+n)} + I_c^{(-n)})/2I_c^{(0)}$, using side-lobe numbers n as indicated in the top left pane of [Figure 6.3\(a\)](#). When B_x is increased we see that (i) the side-lobe maxima are enhanced relative to the central peak, and (ii) the sequence of maxima $I_c^{(n)}$ becomes non-monotonic, even yielding side-lobes that exceed the central lobe in magnitude at the highest field ($B_x = 200$ mT). We can extract the same data from the numerical results presented in [Figure 6.4\(a\)](#), and show in [Figure 6.4\(c\)](#) the resulting lobe maxima $I_c^{(n)}$, normalized by $I_c^{(0)}$. Comparing with the experimental data, we see that the model not only reproduces the gradual enhancement of the side-lobe maxima for increasing B_x , but also captures the more detailed behavior of the series of side-lobes: Whereas at small B_x the maxima $I_c^{(n)}$ monotonically drop for increasing $|n|$, at larger B_x the series becomes non-monotonic, ultimately even producing interference patterns where side-lobes exceed the central maximum in height.

The black dots in [Figure 6.4\(b\)](#), all falling on top of the yellow curve corresponding to $B_x = 0$, represent two data sets with the side-lobe maxima for $B_y = 150$ and 300 mT (all at $B_x = 0$), where we removed the asymmetry by symmetrizing I_c in $\pm B_z$ (as above, this data is normalized by $I_c^{(0)}$). The fact that all these data are equal to the data without in-plane field, within experimental accuracy, confirms that the qualitative change of the interference pattern that we attribute to an SNS-to-SQUID transition only depends on B_x . It also suggests that the asymmetry in $\pm B_z$ has a physical

origin which is distinct from the focusing effects discussed in this section.

In conclusion, the model presented in [Section 6.3](#), that assumes a simple flux dipole in the normal region proportional to B_x , appears to capture many aspects of the qualitative behavior of $I_c(B_z)$ as a function of in-plane field. All global trends we observe in the data are reproduced by our numerical calculations, indicating a transition from Fraunhofer-like interference at zero in-plane field to SQUID-like behavior in the presence of sufficiently strong B_x . A flux dipole in the normal region, induced by flux focusing of the x -component of the in-plane field thus appears to provide the likely explanation for our observations. However, we emphasize that the model used in this section is *not* capable of generating the striking asymmetries in $\pm B_z$.

6.4.2 Asymmetries in the interference patterns

Finally, we turn our attention to the surprising asymmetries observed in the interference patterns of [Figure 6.3\(a,b\)](#). To quantify the asymmetry, we define an asymmetry parameter \mathcal{A}_n for each side-lobe pair $\{n, -n\}$ as

$$\mathcal{A}_n = \frac{I_c^{(-n)} - I_c^{(n)}}{I_c^{(-n)} + I_c^{(n)}}, \quad (6.8)$$

which yields the relative difference in the side-lobe maxima for $\pm B_z$. In this section, we will investigate systematic dependences of \mathcal{A}_n on the magnitude B_r and direction θ of the in-plane field.

In [Figure 6.5\(a\)](#), we plot \mathcal{A}_1 (blue) and \mathcal{A}_2 (red) as functions of B_r with the field applied along \hat{y} . The asymmetry of the first node \mathcal{A}_1 is seen to scale roughly linearly with B_r , reaching $\sim 100\%$ at the highest fields, while the asymmetry of the second node \mathcal{A}_2 remains zero within experimental uncertainty. In [Figure 6.5\(b\)](#), for in-plane

field now along \hat{x} , we now see that both \mathcal{A}_1 and \mathcal{A}_2 increase proportionally to B_r , both reaching $\sim 25\%$ at 250 mT, just before I_c gets fully suppressed (see [Figure 6.2](#)). All asymmetries thus seem to scale linearly with the magnitude of the applied in-plane field. The slope of $\mathcal{A}_n(B_r)$, however, varies considerably: from positive, to zero, to negative for different n and θ . From these two angles ($\theta = 0$ and $\theta = \pi/2$) no systematics are evident.

The dependence of the \mathcal{A}_n on the direction of the in-plane field is shown in [Figure 6.5\(c\)](#). We plot the measured absolute asymmetries $|\mathcal{A}_1|$ and $|\mathcal{A}_2|$ for 16 angles at a fixed field magnitude $B_r = 150$ mT (we use solid and dashed connectors to indicate where the obtained \mathcal{A}_n are positive and negative, respectively). As a reference, we include the anisotropic angular dependence of $I_c^{(0)}$ (filled gray area, plotted in arbitrary units), which we analyzed in terms of a Meissner-induced flux dipole in [Section 6.3](#). The observed evolution of the asymmetry as a function of θ in the present sample has a number of interesting characteristics: (i) The asymmetry of the first side-lobe is maximal for $\theta \sim 5\pi/8$ and minimal in the perpendicular direction $\theta \sim \pi/8$. (ii) The maximal and minimal asymmetries of the second lobe are roughly perpendicular to those of the first lobe. (iii) Consistent with the mirroring in B_z observed upon inversion of B_x or B_y (see [Figure 6.3](#)), both asymmetries have a well defined node at zero about which the behavior of \mathcal{A}_n are antisymmetric in θ (or equivalently B_r).

Separate samples have demonstrated similar behavior, including a linear scaling of the \mathcal{A}_n in field magnitude and a continuous angular evolution of the asymmetry antisymmetric upon π rotation ⁷. Many of the details, however, are very different from sample to sample: The observed magnitudes of \mathcal{A}_1 and \mathcal{A}_2 for given B_r fluctuate up to 100%, and also the angular alignment of their minima and maxima varies across different samples (also the roughly

⁷ See the [Figure B.4](#) for data from different samples.

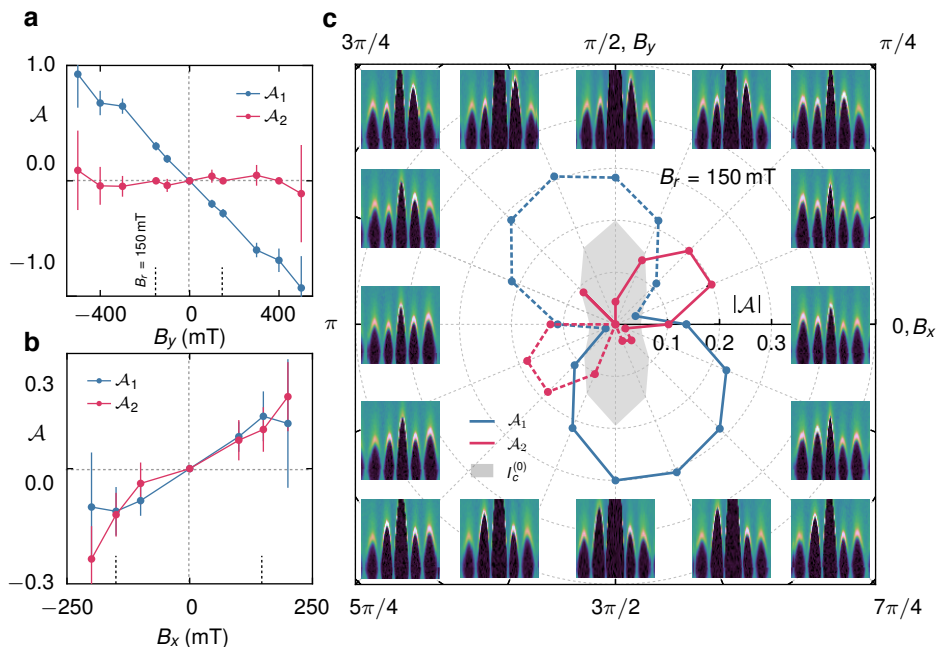


Figure 6.5: **Asymmetry evolution upon field rotation**, (a) Normalized asymmetry \mathcal{A} in the lobe maxima as a function of B_y , for the first two side-lobes (shown in blue and red respectively). (b) As (a), for magnetic fields oriented along \hat{x} . (c) Magnitude of the asymmetry parameter $|\mathcal{A}|$ as a function of in-plane field angle θ . Solid(dashed) lines connect points indicating where \mathcal{A}_n are positive(negative). The in-plane field is fixed to $B_r = 150$ mT. To emphasize the deviation of this angular dependence from the anisotropy observed for $B_z = 0$ (see Section 6.3), we include in gray the height of the central lobe $I_c^{(0)}$ as a function of θ (arbitrary units). The panels along the edges show the differential-resistance data from which the asymmetries are extracted.

perpendicular orientation of the maxima of \mathcal{A}_1 and \mathcal{A}_2 observed in Figure 6.5 is not a consistently observed feature). The variation of all these details does not display a clear trend following any of the controllable device parameters, such as W , L , or the orientation of the junction with respect to the crystallographic axes of the InAs wafer. This suggests that the asymmetries are the result of an intricate interplay of many device-dependent factors, most likely including SOI, disorder, local details of the coupling between the InAs and the Al, and the microscopic shape of the sample.

Although it thus seems difficult to pinpoint the physical mechanism responsible for the asymmetries, we can try to develop a qualitative picture by carrying out a general analysis along the lines of Ref. [194]. We construct a model (Bogoliubov-de Gennes) Hamiltonian, treating the electrons in the junction as a two-dimensional free electron gas in the presence of a vector potential due to the applied magnetic field (including the flux dipole proportional to B_x). We add to this Hamiltonian finite superconducting pairing potentials of equal magnitude under the left and right contacts, and terms accounting for Rashba and Dresselhaus SOI, Zeeman splitting, and an arbitrary disorder potential $V(x, y)$. We can then investigate under what circumstances the symmetries of the total Hamiltonian dictate the critical current to be symmetric in B_z and when this symmetry is broken.

The most important conclusion is that if $V(x, y) = 0$ the symmetry $I_c(+B_z) = I_c(-B_z)$ is protected, and the model will produce a symmetric interference pattern for a symmetrically shaped sample, no matter how all other parameters are tuned. Disorder or other spatial asymmetries in the junction are thus a necessary ingredient for obtaining an asymmetric critical current. More specifically, we find: (i) In the presence of an in-plane field oriented along \hat{x} , only one of the mirror asymmetries $V(x, y) \neq V(-x, y)$ or $V(x, y) \neq V(x, -y)$ has to be present to allow for an asymmetric interference pattern. (ii) If the in-plane field is along \hat{y} , a direction

along which we observe a strong asymmetry (see [Figure 6.5](#)), only $V(x, y) \neq V(x, -y)$ breaks the symmetry.

As a side note, we mention that some combinations of symmetry-breaking ingredients only affect the higher Fourier components of the current-phase relation $I_s(\varphi)$. For instance, in order to have $I_c(+B_z) \neq I_c(-B_z)$ in combination with a purely sinusoidal $I_s(\varphi)$, it is required to have (in addition to disorder): (i) a finite B_x or (ii) a finite B_y *and* SOI. In this case, the degree of asymmetry left at $\theta = \pi/2$ could thus present a measure for the strength of SOI in the junction. In our experiment, however, current was controlled rather than phase, so we do not know to what degree the current-phase relation is nonsinusoidal. In general, one expects junctions with weak NS-coupling to have a nearly sinusoidal $I_s(\varphi)$ [195]. Engineering a barrier between the normal and proximitized regions in the QW could thus present a way to obtain more detailed knowledge about the SOI in the sample.

Our qualitative analysis thus clearly supports the idea that a key role is played by structural asymmetries in the device, already suggested by the strong sample-to-sample variation observed in the data. As to the mechanisms that can break spatial symmetries in our samples, we identify three: (i) spatial variation in the couplings to the superconducting contacts, (ii) imperfections in the microscopic shape of the junction, or (iii) a random disorder potential. Owing to the epitaxial growth of Al and the small size of the junction, we expect the couplings to the contacts to be relatively homogeneous. Further, measurements of the asymmetry as a function of gate voltage, presented in [B.2](#), show that the asymmetries in I_c are robust to gating in both magnitude and angular dependence. This weak gate dependence could indicate that the dominant spatial symmetry breaking mechanism is stable, which also suggests that it is either the specific shape of the junction or a fixed disorder potential induced by ionized impurities in the QW. To further support this picture, we also performed tight-binding numerical

simulations of the supercurrent through a two-dimensional disordered SNS junction focusing on the asymmetry parameters \mathcal{A}_n ; the results are presented in [Section B.4](#). We find patterns that look similar to those extracted from the experimental data and also display a strong variation from device to device (i.e. when we change the disorder configuration). This also supports our speculation that disorder plays a crucial role in the underlying mechanisms responsible for the asymmetries.

An alternative explanation of the asymmetries one could propose is in terms of Abrikosov vortices near the junction; the presence of such vortices is known to induce asymmetries in the critical current upon inversion of B_z . In the limit of single vortices the behavior is well understood and studies have successfully mapped the position of vortices from the modification of interference patterns [[182](#), [196](#)]. For large numbers of vortices, experimental and theoretical investigations exist in the limit of disordered vortex arrays [[197](#), [198](#)], yielding seemingly random interference patterns. Theoretical work on ordered vortex arrays predicts symmetric interference patterns described by minor modifications to [Eq. \(6.1\)](#) [[199](#)].

While we expect flux penetration of the leads in a perpendicular field, and thus vortices to be present, we observe no indication of quantized vortex entrance events, i.e., sudden switches in the critical current [[196](#)]. Furthermore, we do not observe asymmetries without the application of an in-plane field, which seems to be incompatible with vortices as the origin of the asymmetry. Furthermore, the mirror symmetry in B_z of the observed asymmetry upon reversing the sign of the in-plane field would require an almost perfect reversal of the vortex configuration, which is highly unlikely.

To conclude, we believe that in the mechanisms underlying the asymmetries we explored in this section, an important role is being played by structural disorder in the samples. Given the com-

plexity of the system and the randomness of what appears to be the most important symmetry-breaking ingredient, it is currently unclear whether measurements of the asymmetry could be used to quantify the strengths of SOI and Zeeman coupling in these devices. SNS junctions designed with a well-defined built-in dominant asymmetry might allow for disentangling these effects; this warrants further work.

6.5 CONCLUSION

We report a systematic experimental study of the behavior of two-dimensional epitaxial Al/InAs/Al SNS junctions under the application of out-of-plane as well as in-plane magnetic fields. Measuring the critical current as a function of the magnitude and direction of the applied magnetic field, we discover a strong influence on the properties of the junction of flux focusing from the superconducting contacts, both for perpendicular and in-plane magnetic fields. For in-plane fields applied along the direction of average current flow, flux focusing results in an effective flux dipole in the normal region, causing transport to be localized towards the edges of the sample. We thus find that the in-plane field may act as a novel control knob allowing for magnetic confinement of Andreev states in such hybrid superconductor-semiconductor systems. We further observe striking asymmetries in the interference pattern $I_c(\pm B_z)$ when an in-plane field is applied. Although most qualitative properties of these asymmetries remain unexplained, we argue that the microscopic structure of the device plays an crucial role, potentially masking the influences of spin-orbit and Zeeman coupling.



SCALABLE MAJORANA DEVICES

Majorana zero modes have received widespread attention due to their potential to support topologically protected quantum computing [201]. Emerging as zero-energy states in one-dimensional semiconductors with induced superconductivity, Zeeman coupling, and spin-orbit interaction [71, 72], Majorana modes have been primarily investigated in individual InSb or InAs nanowires [12–16], including recently realized epitaxial hybrid nanowires [17, 125, 127]. Tests of non-Abelian statistics of Majoranas involve braiding [202, 203] or interferometric measurement [204–206], requiring branched geometries, which are challenging to realizing using nanowire growth. Scaling to large networks using arrays of assembled nanowire also appears difficult. Here we explore signatures of Majorana zero modes in devices made from a two-dimensional heterostructure [151, 156] using top-down lithography and gating. Scalable top-down fabrication readily allows complex geometries and large networks, paving the way toward applications of Majorana devices.

7.1 BALLISTIC TUNNEL PROBE

A schematic of one of the samples is shown in Fig. 7.1(a), with the heterostructure layers in the inset. The InAs/InGaAs quantum well is close to the surface and covered by a thin layer of epitaxial Al. Large mesas are first etched to isolate individual devices (not shown), then the Al top layer is selectively etched into an effective

Adapted from [200]

wire of width $W \sim 100$ nm and length $L \sim 1$ μm (Fig. 7.1(b)). One end of the wire is connected to a large Al plane, serving as measurement ground. On the other end, a ~ 40 nm gap (indicated by the dashed circle in Fig. 7.1a) separates the Al wire from the opposing Al plane, acting as voltage source. A global insulating layer and a metallic topgate were then deposited on the entire sample.

Initially, the Al wire is surrounded by conductive 2DEG. Applying a negative potential V_G to the top gate, the wide exposed 2DEG regions adjacent to the Al strip are depleted, leaving a narrow conducting InAs channel strongly coupled to the Al. Due to screening by the surrounding Al, conduction through the constriction persists to more negative gate voltages than the 2DEG planes, resulting in a gate voltage range where wire and Al plane are tunnel coupled. As we will show in the following, the constriction is single mode and ballistic. Furthermore, the asymmetric Al regions allow for a useful (and, to our knowledge, novel) magnetic-field tuning of the device properties. As the Al strip width W is significantly shorter than the superconducting coherence length $\xi_{\text{Al}} \sim 1.6$ μm [159], its critical field is enhanced with respect to the Al plane [208, 209]. It is then possible, by changing the magnetic field strength and orientation, to tune the wire-plane configuration from superconductor-superconductor (S-S), to superconductor-normal (S-N), to normal-normal (N-N). We give evidence of this tuning both in the open regime (Fig. 7.1(c)) and in the tunneling regime (Fig. 7.2(a)).

The four-terminal differential conductance of the device as a function of gate voltage is shown in Fig. 7.2(c). We are interested in the regime close to pinch-off, where the narrow junction is well defined. Applying an out of plane field $B_{\perp} = 1$ T, superconductivity in the whole system is suppressed, resulting in the N-N configuration. Similarly to a conventional quantum point contact, the conductance shows a plateau of $2e^2/h$, demonstrating the junction is single mode and ballistic. In the same gate voltage range, the

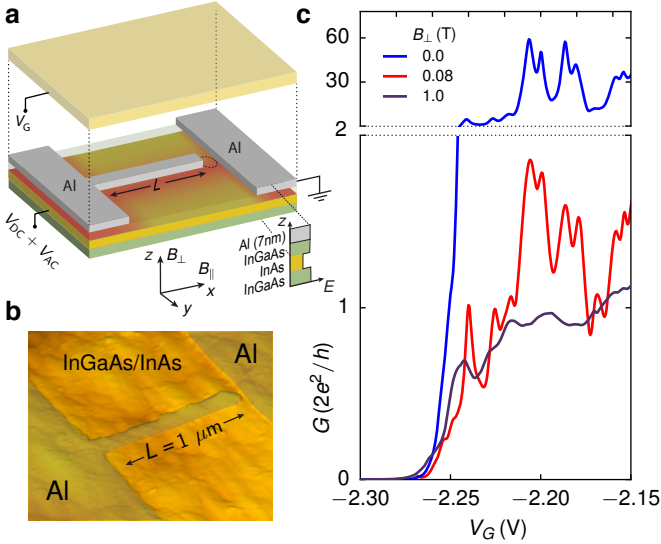


Figure 7.1: **Device schematic and behavior of the ballistic probe.** (a) Device schematic indicating the aluminum leads (gray), InAs 2DEG (yellow), InGaAs barrier (green) and top gate (orange). The insulating layer between the device structure and the electrostatic gate has been omitted for clarity. The tunneling probe location is indicated by the dashed circle. Inset: band alignment as a function of depth z highlighting the finite confining barrier between the Al and InAs. (b) False colored atomic force micrograph of a lithographically identical device before ALD and gate deposition. (c) Conductance as a function of gate voltage for $B_{\perp} = 0$ (blue), $B_{\perp} = 0.08$ T (red) and $B_{\perp} = 1$ T (purple).

zero field data (S-S configuration, blue line) shows a conductance increase up to $120 e^2/h$, reminiscent of a supercurrent. Finally, setting B_{\perp} to 0.08 T, the Al plane is driven normal ($B_{\perp,c} \sim 0.06$ T) while the wire persists in the superconducting regime, resulting in

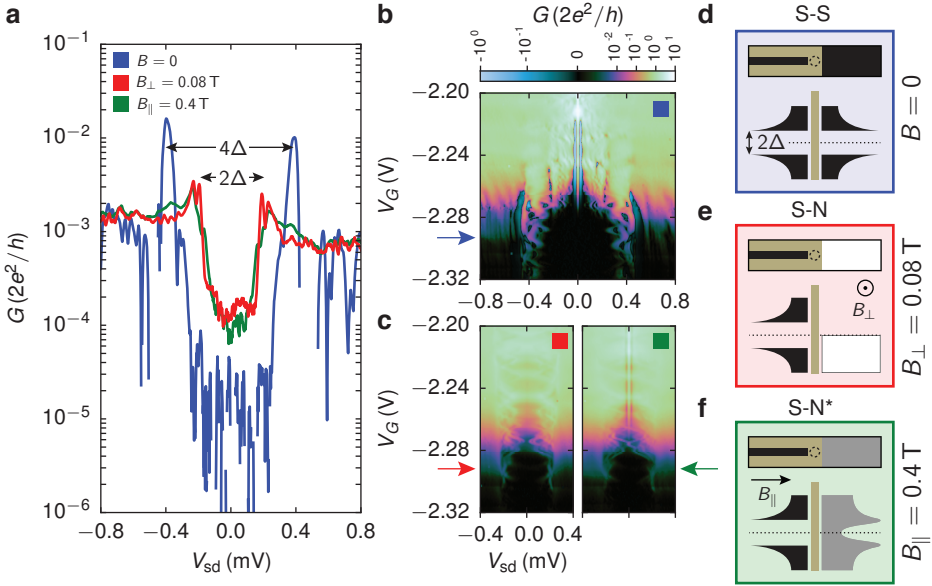


Figure 7.2: **Superconducting gap in the tunneling regime and transition to an effective normal probe in a magnetic field.** (a), Tunneling spectroscopy of the wire for $B = 0$ (blue), $B_{\perp} = 0.08$ T (red) and $B_{\parallel} = 0.4$ T, aligned along the wire (green). (b,c), Tunneling spectroscopy of the superconducting gap for the three field configurations in (a). The colors from (a) identify each panel, with arrows indicating the gate voltage location of the traces in (a). A non-linear color-scale is used [207]. (d–f) Schematic representations of the three regimes of operation shown in (a) with relative DOS in the wire (left) and Al plane (right). Superconducting Al is represented in black, white indicates that the Al has been driven normal and gray that the Al is still superconducting but the induced gap is soft.

the S-N configuration (red curve). In the S-N configuration the conductance plateau approaches $4e^2/h$ as expected in a single-mode

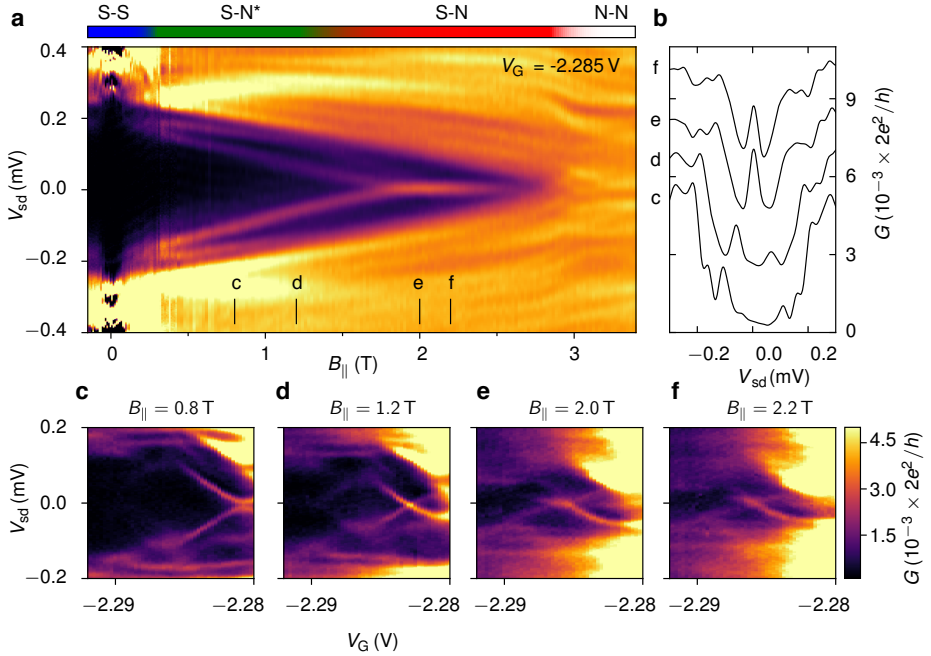


Figure 7.3: **Stable zero energy state at large in-plane field.** (a) Conductance as a function of source-drain bias and parallel magnetic field. The upper colorbar schematically indicates, with reference to Fig. 7.1, the DOS configuration in the wire and under the 2D plane. The colorscale used is shared with (c–f). (b) Line cuts taken at the points indicated in a. Curves are successively offset by $2.5 \times 10^{-3} 2e^2/h$. (c–f) Stability scans as a function of bias and gate voltage at the field positions indicated in (a).

S-N junction with high probability of Andreev reflection [124], and recently reported in a similar system [156].

7.2 MAGNETIC FIELD REGIMES

The magnetic tuning of the junction is also evident in the tunneling spectroscopy data shown in Fig. 7.2(a). In the S-S geometry (blue line), the zero field conductance shows a 4Δ gap, owing to convolution of two BCS-like densities of states with $\Delta = 180 \mu\text{eV}$, as schematically shown in Fig. 7.2(d) [210]. In the S-N configuration (red line) the constant density of states in the plane, as shown in Fig. 7.2(e), results in a direct measurement of the superconducting gap of the wire. The full gate voltage evolution in the S-S and S-N scenarios is presented in Fig. 7.2(b) and (c) (left panel), identified by the colored boxes. In both cases, a sharp transition from $G \sim 2e^2/h$ to $G \sim 0$ is observed at large bias, indicative of a clean junction. The S-S configuration also shows, for $V_{\text{sd}} = 0$ and $V_g > -2.28 \text{ V}$, a large conductance peak surrounded by regions of negative differential conductance, which is identified as a supercurrent precursor [211]. Similarly, regular sub-gap features in the open S-S regime are assigned to multiple Andreev reflections. Supercurrent and multiple Andreev reflections disappear in the S-N configuration (Fig. 7.2(c), left panel).

A particularly interesting situation is obtained for an in plane field $B_{\parallel} = 0.4 \text{ T}$ aligned along the wire, well below the critical field of the large Al plane ($B_{\parallel,c} \sim 1.3 \text{ T}$). Tunneling spectroscopy in this regime reveals a 2Δ gap (green line in Fig. 7.2(a)) very similar to the S-N configuration discussed previously. On the other hand, conductance in the open regime shows a supercurrent peak (Fig. 7.2(c), right panel), a hallmark of the S-S configuration. This seemingly contradictory scenario is readily explained with a superconducting density of states in the large Al regions developing a soft gap in an in-plane field, as shown in Fig. 7.2(f). In this configuration, referred to as S-N^{*}, the 2D plane stays superconducting, but in the tunneling regime acts as a quasi-constant DOS probing

the wire. Independent measurements of the field induced gap softening in a variety of samples are presented in the [Section C.2](#).

7.3 MAJORANA ZERO MODES

We now focus on probing the wire under conditions relevant for topological superconductivity. To enter the topological phase, a magnetic field aligned perpendicular to the spin-orbit direction must be applied. For a Rashba dominated system, as in the present case, the spin-orbit field is oriented in the plane of the 2DEG and perpendicular to current flow. We thus orient B_{\parallel} along the wire direction. The topological transition is expected at a field $B_{\parallel}^* = 2\sqrt{\Delta^2 + \mu^2}/g\mu_B$ [72], with μ the chemical potential, g the g -factor of the states in the wire, and μ_B the Bohr magneton.

Figure 7.3a shows the wire tunneling conductance as a function B_{\parallel} for a top gate voltage $V_G = -2.285$ V, setting the constriction in the tunneling regime. The 4Δ gap observed for $B_{\parallel} = 0$ collapses to 2Δ by $B_{\parallel} = 0.3$ T, attributed to the gap softening under the 2D plane (corresponding to the transition from Fig. 7.2(b) to (d)). The 2D plane evolves continuously from a softened gap (S-N^{*}) into the normal state (S-N) by $B_{\parallel} \sim 1.5$ T. For $B_{\parallel} \geq 2.9$ T, superconductivity in the Al wire is quenched, yielding the N-N state.

Starting from $B_{\parallel} = 0.4$ T a pair of states emerge from the gap edge and linearly approach $V_{sd} = 0$ with an effective g -factor $|g^*| = 2\delta V_{sd}/\mu_B \delta B \sim 4$ (see also [Section C.4](#)). At $B_{\parallel} = 1.8$ T the two states merge at zero energy and stick there until the overall gap collapses, at $B_{\parallel} = 2.9$ T. Figure 7.3(b) shows line cuts from Fig. 7.3(a) at the marked positions. The two states are symmetrically positioned around zero bias, as expected by particle-hole symmetry, but have different amplitudes. This is presumably due to finite voltage effects in conjunction with a spatially asymmetric device. Reverting the source and drain contacts results in a bias reversal of the asymmetry. Similarly to previous results in nanowires

[17], the g -factor associated to the Majorana precursors is significantly reduced from that of the bulk semiconductor ($g \sim -12$ for InAs). This is presumably due to the hybrid nature of these states, extending in both Al and InAs.

To emphasize the stability of the observed zero bias peak (ZBP), Figs. 7.3(c–f) show gate scans at the marked positions in Fig. 7.3a. At low field ($B_{\parallel} > 0.4$ T) two subgap Andreev states are present, which evolve as a function of bias and field. In Fig. 7.3(e), at $B_{\parallel} = 2.0$ T, these states merge at zero bias over a finite gate voltage range, distinct from the simple point-like crossing in Fig. 7.3(d). Further increasing the field (2.2 T in Fig. 7.3(f)) has a negligible effect on the ZBP, with only the bounding gap shrinking slightly.

7.4 MAGNETIC FIELD ANGLE AND TEMPERATURE DEPENDENCE

To further investigate the origin of the ZBP, we vary the magnetic field orientation θ in the 2DEG plane, with $\theta = 0$ being parallel to the wire. As explained above, a Majorana zero mode should only manifest itself for a sufficiently strong field along $\theta = 0$. Figure 7.4 shows three such rotations for constant magnetic field amplitudes B_r . In all cases, the rotations demonstrate the ZBP stability within a narrow angle range centered at $\theta = 0$, expanding with B_r , consistent with a larger field component perpendicular to \mathbf{B}_{S0} . For larger misalignment angles, the superconducting gap softens and the ZBP splits into two Andreev levels, presumably due to the failure of the topological criterion as the component of $|\mathbf{B}|$ perpendicular to \mathbf{B}_{S0} decreases.

Similarly to previous observations [12, 17], the height of the ZBP is significantly reduced from the quantized value of $2e^2/h$, predicted in the absence of disorder at zero temperature [212, 213]. Disorder in our samples is presumably comparable to conventional nanowires, as suggested by the observation of clear conductance plateaus and a hard superconducting gap. Despite this, the lim-

ited gate voltage range over which the ZBP appears is indicative of significant subband mixing, presumably addressable with wafer structures of higher quality. Figure 7.4(c) (top panel) shows the evolution of the ZBP of Fig. 7.3(a) for $B_{\parallel} = 2.0$ T as a function of mixing chamber temperature T_{mc} , with linecuts shown in Fig. 7.4(b). Consistent with previous measurements of Majorana modes [12], the ZBP is fully suppressed by 300 mK, corresponding to an energy scale for the topological gap on the order $\Delta_T \sim 30$ μeV . The superconducting gap persists up to 1 K, with an overall lifting of the gap background due to thermal quasiparticle excitation. Figure 7.4(c) (bottom panel) shows the peak height G_{max} and full width at half maximum (FWHM) for $T \leq 200$ mK, where the quasiparticle background conductance is negligible. Decreasing the temperature, the ZBP gets sharper and its height monotonically increases, with a saturation reached below $T \approx 50$ mK, presumably due to the failure of cooling the electrons further. In this intermediate regime, the peak conductance is proportional to $T^{-\alpha}$, with $\alpha = 0.4 \pm 0.02$ while the peak full width at half maximum (FWHM) scales approximately as G_{max}^{-1} . These observations suggest the ZBP height and width are temperature limited in the present experimental configuration, with the coupling to the leads playing a negligible role.

7.5 CONCLUSION

In conclusion, we have investigated transport signatures of Majorana zero modes in devices defined by top-down lithographic patterning of hybrid InAs-Al two-dimensional heterostructures. Measurements show many features observed in previous studies, including a non-universal zero-bias conductance peak, which appears when an external magnetic field is applied along the wire axis. The scalable fabrication developed here opens the door to complex device geometries and extended networks of Majorana devices.

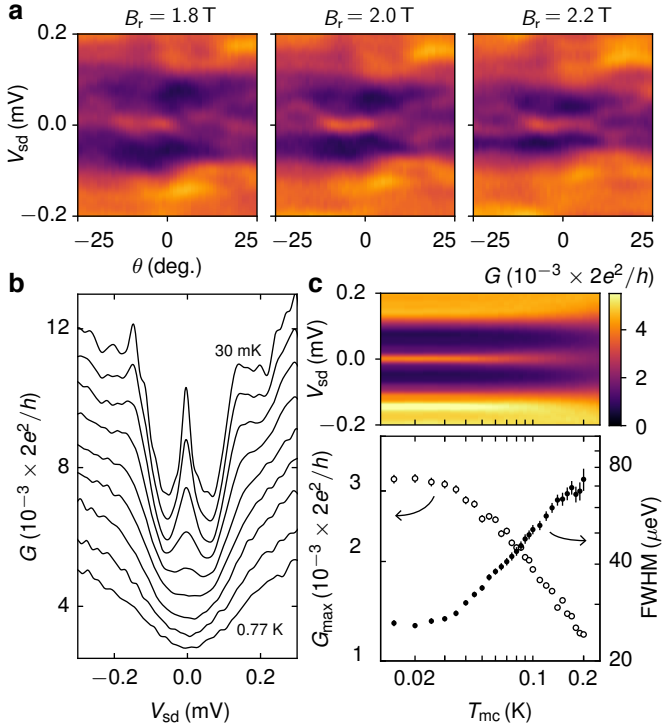


Figure 7.4: **Stability of the zero bias peak as a function of field angle and temperature.** (a) Conductance as a function of bias and in-plane magnetic field orientation θ for fixed field magnitudes B_r . $\theta = 0$ indicates a field alignment parallel to the wire. (b) Conductance linecuts as a function of bias for fixed values of the mixing chamber temperature T_{mc} . With decreasing temperature, the ZBP gets sharper and higher. Curves are offset for clarity. (c) Detailed temperature evolution of the ZBP (upper panel), and extracted ZBP height G_{max} and full width at half maximum (FWHM) as a function of T_{mc} (lower panel). Note that the vertical axes have logarithmic scales.

Part IV

APPENDIX

EPITAXIAL HETEROSTRUCTURE FABRICATION

1. **Clean:** 60 s acetone at 50°C. IPA rinse. N₂ blowdry.
 2. **Spin coat:** Deposit PMMA A4 at 500 RPM. Spin at 4000 RPM for 45 s. Bake at 185°C for 3 min.
 3. **Expose:**
 - a) Inner features at 500 pA, dose = 0.4 μs/dot
 - b) Outer features at 20 nA, dose = 0.36 μs/dot
 - c) Develop in MIBK:IPA (1:3) for 60 s
 - d) Rinse in IPA for 20 s. N₂ blow dry.
 4. **Ash:** O₂ plasma for 60 s.
 5. **Al etch:** 10 s in Transene D at 50°C. Rinse 20 s in MQ at 50°C. Rise 40 s in MQ at RT.
 6. **Mesa etch:** 10 min in (220 : 55 : 3 : 3) H₂O : Citric acid : H₃PO₄ : H₂O₂. Rinse for 40 s in MQ. N₂ blow dry.
 7. **Strip:** Follow [1](#)
-

Method A.1: **Mesa etch.**

-
1. **Clean:** 60 s acetone at 50°C. IPA rinse. N₂ blowdry.
 2. **Spin coat:** Deposit PMMA A₄ at 500 RPM. Spin at 4000 RPM for 45 s. Bake at 185°C for 3 min.
 3. **Expose:**
 - a) Inner features at 500 pA, dose = 0.4 μs/dot
 - b) Develop in MIBK:IPA (1:3) for 60 s
 - c) Rinse in IPA for 20 s. N₂ blow dry.
 4. **Ash:** O₂ plasma for 30 s.
 5. **Al etch:** 10 s in Transene D at 50°C. Rinse 20 s in MQ at 50°C. Rise 40 s in MQ at RT.
 6. **Strip:** Follow [1](#)
-

Method A.2: **Aluminium etch.**

-
1. **ALD setup:** Set ALD stage temperature to 90°C.
 2. **Purge:** Turn on N₂ flow and close all precursor valves. Purge chamber by running cleaning program.
 3. **Precursor:** Open trimethylaluminium precursor valve.
 4. **Clean:** 60 s acetone at 50°C. IPA rinse. N₂ blowdry.
 5. **Deposition:** Load sample into deposition chamber and pump it out. Start deposition process of 300 cycles of TMA followed by H₂O, with 30 s purge times after each pulse.
 6. **Verification:** Ensure the process is running smoothly by observing the pressure spikes on each pulse.
-

Method A.3: **Atomic layer deposition.**

-
1. **Clean:** 60 s acetone at 50°C. IPA rinse. N₂ blowdry.
 2. **Spin coat:** Deposit PMMA A₄ at 500 RPM. Spin at 4000 RPM for 45 s. Bake at 185°C for 3 min.
 3. **Expose:**
 - a) Inner features at 500 pA, dose = 0.4 μs/dot
 - b) Develop in MIBK:IPA (1:3) for 60 s
 - c) Rinse in IPA for 20 s. N₂ blow dry.
 4. **Ash:** O₂ plasma for 45 s.
 5. **Sticking layer:** Deposit 5 nm of Ti at 1Å/s.
 6. **Metal deposition:** Deposit 50 nm of Au at 1.5Å/s.
 7. **Liftoff:** 1 h in dioxalane at 50°C. If necessary, use N₂ gun with syringe attachment to lightly blow bubbles.
-

Method A.4: **Fine gate deposition.**

-
1. **Clean:** 60 s acetone at 50°C. IPA rinse. N₂ blowdry.
 2. **Spin coat:**
 - a) Deposit EL9 at 500 RPM. Spin at 4000 RPM for 45 s. Bake at 185°C for 3 min.
 - b) Deposit PMMA A₄ at 500 RPM. Spin at 4000 RPM for 45 s. Bake at 185°C for 3 min.
 3. **Expose:**
 - a) Inner features at 500 pA, dose = 0.4 μs/dot
 - b) Outer features at 20 nA, dose = 0.4 μs/dot
 - c) Develop in MIBK:IPA (1:3) for 60 s
 - d) Rinse in IPA for 20 s. N₂ blow dry.
 4. **Ash:** O₂ plasma for 60 s.
 5. **Sticking layer:** Deposit 5 nm of Ti at 1Å/s.
 6. **Metal deposition:** Deposit 250 nm of Au at 1.5Å/s.
 7. **Liftoff:** 4 h in dioxalane at 50°C. If necessary, use N₂ gun with syringe attachment to lightly blow bubbles.
-

Method A.5: **Outer gate deposition.**

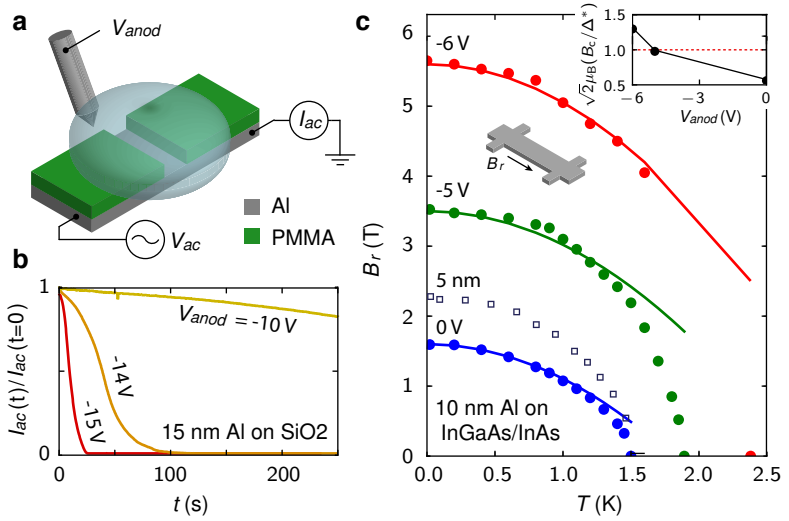


Figure A.1: **Anodization** (a) Anodization test setup with real-time monitoring in an SNS geometry following [214]. (b) Normalized current passing through the SNS structure as a function of time for three different anodization voltages, the final oxide thickness is proportional to the applied voltage (~ 1 nm/V for Al [215]). For $V_{anod} = -15$ V the full thickness of the film has been oxidized and the current falls to zero. (c) The same method can also be used to thin down Al films. Superconducting phase boundary measured in a Hallbar geometry (inset) for as-grown 10 nm (blue dots) and 5 nm (open squares) Al films, and films anodized at -5 V (green) and -6 V (red). The significant increase in T_c and B_c for the anodized films may indicate successfully thinned films, however the formation of coupled Al islands cannot be ruled out.

ANOMALOUS FRAUNHOFER SIMULATIONS

B.1 ESTIMATING B_{c1}

In order to determine B_{c1} we need to estimate the parameter $\kappa = \lambda/\xi$. We use values for bulk Al from the literature [159]: $\xi_{\text{bulk}} = 1.6 \text{ } \mu\text{m}$ and $T_{c,\text{bulk}} = 1.2 \text{ K}$. From our measurements we have an accurate value for T_c (see Section 4.3.1) and we know from [54] that

$$\Delta(0) = 1.76 k_B T_c \quad \text{and} \quad \xi = \frac{\hbar v_F}{\pi \Delta}. \quad (\text{B.1})$$

These expressions allow us to determine the coherence length in the thin film limit as a function of known parameters, yielding

$$\xi_{\text{thin}} = \xi_{\text{bulk}} \frac{T_{c,\text{bulk}}}{T_{c,\text{thin}}}, \quad (\text{B.2})$$

the same method is e.g. used in Ref. [216]. Substituting the known values of $T_{c,\text{bulk}}$, ξ_{bulk} and the $T_c = 1.5 \text{ K}$ measured gives $\xi = 1.28 \text{ } \mu\text{m}$ for the superconducting film. We may also estimate the penetration depth from known quantities [54, 217]

$$\lambda = \lambda_L(0) \sqrt{1 + \frac{\xi}{d}}. \quad (\text{B.3})$$

Using the value for $\lambda_L = \lambda_{L,\text{bulk}} = 16 \text{ nm}$ from the literature and using the modified ξ calculated above, we obtain $\lambda = 180 \text{ nm}$ for a film thickness of $d = 10 \text{ nm}$.

Finally we can estimate B_{c1} . For type-II superconductors the field of first vortex penetration (assuming a magnetic field perpendicular to the film) is given by [54]

$$B_{c1} \approx \frac{\Phi_0}{4\pi\lambda^2} \log \kappa = \frac{B_c}{\sqrt{2}\kappa} \log \kappa. \quad (\text{B.4})$$

Importantly this formula assumes that $\kappa > 1/\sqrt{2}$. For our values $\kappa \approx 0.2 \times (1/\sqrt{2})$, clearly in the type-I regime. However, in the thin-film limit the penetration depth is renormalized such that $\kappa = \Lambda/\xi$ [218, 219], where $\Lambda \sim \lambda^2/d$. Using this renormalization we obtain $\kappa \sim 2.5$, which lies in the type-II regime. Using these numbers together with $B_{c,z} \sim 30$ mT yields $B_{c1} = 7.7$ mT. It is worth noting that the first vortex may penetrate before B_{c1} is reached [220].

B.2 GATE DEPENDENCE

The QW used for the experiment hosts two subbands at $V_g = 0$. Based on Hall measurements, we know that the transition to the single subband limit is achieved at $V_g \sim -2$ V (c.f. Figure 5.4).

Figure B.1 (a) shows the measured differential resistance R , as a function of gate voltage V_g and bias current I . The interference patterns obtained at four different values of V_g are shown in Figure B.1(c-f). From these data we can extract the field-dependent critical current $I_c(B_z)$, which we correct for the flux focusing parameter Γ (see Section 6.2). The resulting $I_c(B_z)$ can be used to calculate the supercurrent density $J_c(y)$ using the Dynes and Fulton method [120], the results are shown in the insets in Figure B.1(c-f). All curves show a supercurrent density accumulation towards the lateral edges of the SNS, the effect being more accentuated at negative gate voltages. This effect is also captured in Figure B.1(b), where we plot the normalized side-lobe maxima. Compatibly with the accumulation of J_c at the edges, the side-lobe maxima are gradually lifted upon depletion of the 2DEG. For $V_g < -2$ V, an

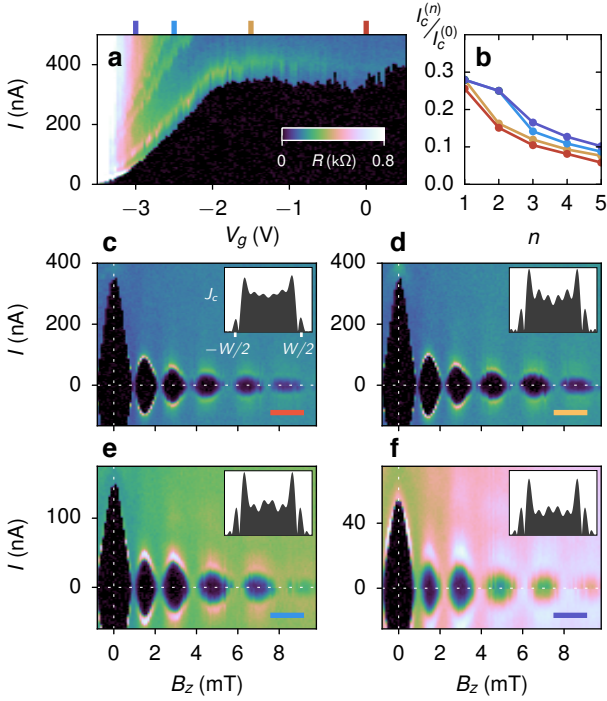


Figure B.1: **Supercurrent density gate dependence.** (a) Differential resistance R , as a function of gate voltage V_g and bias current I . (b) Normalized critical current as a function of side-lobe index n , for varying gate voltages, denoted by the colored markers in (a). (c-f) Differential resistance R , as a function of bias current I and out-of-plane magnetic field B_z , for the different values of gate voltage denoted in (a). Insets show the extracted supercurrent density $J_c(y)$. (c) is based on the same dataset as shown in [Figure 6.1\(c\)](#)

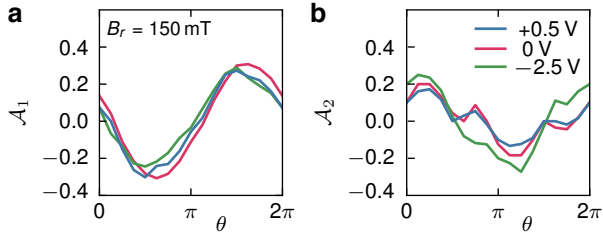


Figure B.2: **Gate dependence of the Fraunhofer asymmetry.** (a) Measured magnetic field asymmetry \mathcal{A}_1 for the first side-lobe as a function of in-plane field angle θ . (b) as (a) for the second side-lobe \mathcal{A}_2 . Curves are colored according to gate voltage. Note that the zero gate voltage data is the same as that displayed in [Figure 6.5](#).

anomalous lifting of the $n = 2$ side-lobe is observed, similar to [Figure 6.4\(b\)](#) where in an in-plane field is applied. We interpret the gate-voltage-induced enhancement of the critical current density at the mesa edges with band bending. InAs is well known to host a surface accumulation layer due to the breaking of the translational symmetry of the crystal [19, 20]. Due to the presumably high initial electron density at the edges we expect these features to dominate as the 2DEG is depleted.

Finally we investigate the effect of the gate on the asymmetries in the interference pattern. In [Figure B.2\(a,b\)](#) we plot the asymmetry of the first two lobes, \mathcal{A}_1 and \mathcal{A}_2 respectively, as a function of in-plane field angle at a fixed magnitude of $B_r = 150 \text{ mT}$. The asymmetry of the two lobes is largely independent of gate voltage, both in amplitude and angular alignment. These results highlight how the asymmetries are robust against variation of carrier density and subband occupation of the system.

B.3 ADDITIONAL DEVICES

B.3.1 Flux focusing control device

The behavior of a control device with large regions of removed aluminum behind the junction, as shown in [Figure B.3\(a\)](#), is demonstrated in [Figure B.3\(b\)](#) and (c). The dimensions of the central semi-conducting region are lithographically identical to that of the primary device studied in [Chapter 6](#), cf. [Figure 6.1\(a\)](#). In contrast the device in [Chapter 6](#) with Al lead dimensions $W = 1.5 \mu\text{m}$ and $2L_{\text{Al}} \sim 10 \mu\text{m}$, the contacts of the device presented here have $W = 1.5 \mu\text{m}$ and $2L_{\text{Al}} = 0.3 \mu\text{m}$. The lack of extended aluminum planes atop the leads results in a more uniform magnetic field profile perpendicular to the junction plane, minimizing flux focusing. [Figure B.3\(b\)](#) shows the measured interference pattern of $I_c(B_z)$ on this device. All figures from here on including colorplots are displayed on a constant colorscale ranging from $R = 0$ to $R = 0.5 \text{ k}$. By extracting the positions of the visible node closings we obtain an effective field enhancement as shown in [Figure B.3\(c\)](#), which can be compared to [Figure 6.1\(d\)](#). Whilst a finite enhancement is observed, the value is roughly constant in the field range measured. Applying the model developed in [Eqs. 6.3–6.6](#) to the present flux-minimizing geometry yields the blue curve, in good agreement with the data.

B.3.2 Devices rotated with respect to crystal axes

A number of additional samples were investigated where the device design was rotated relative to the crystal, as shown in the top right of [Figure B.4](#). These devices are otherwise lithographically identical to the one examined in [Chapter 6](#).

The top row of [Figure B.4](#) shows the interference patterns observed in all devices. The second row shows the extracted field

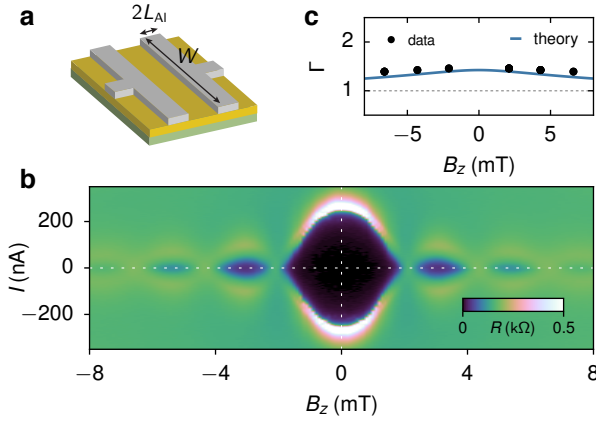


Figure B.3: **No flux focusing** (a) Schematic of the flux-focusing control device. (b) Differential resistance R as a function of current I and perpendicular field B_z . (c) Extracted field enhancement at the nodes visible in (b) (markers), and fit using Eqs. 6.3–6.6 (solid line).

enhancement parameters of all visible nodes for each device (markers). For comparison with Chapter 6 we also plot the enhancement envelope from Figure 6.1(d) (solid gray line). All devices show aperiodic node spacings, with the effective field enhancement decreasing with increasing applied field. The variation in $\Gamma(B_z)$ observed across the samples is attributed to small variations in the effective sample dimensions arising during processing. The third row demonstrates the behavior of the critical current for a purely in-plane field ($B_z = 0$) as a function of field angle θ (the current is normalized to the maximum value $I_{c,max}$ measured at zero field). Curves are shown for varying in-plane field magnitudes and gate voltages as detailed in the legend. Overall, we see roughly a factor of two suppression of I_c between $B_T = 75$ mT and 150 mT when

the field is applied along the current (x direction, $\theta = 0$). For fields applied perpendicular to the current (y direction, $\theta = \pi/2$) the suppression is considerably weaker, consistent with our interpretation in terms of flux focusing. Negligible differences are observed for different values of gate voltage. The fourth and fifth rows demonstrate the behavior of the asymmetry parameters \mathcal{A} of the first and second side-lobe pair respectively. Concentrating initially on the [011] column, corresponding to a device nominally identical to the one examined in [Chapter 6](#), it is clear that the specific behavior of the asymmetry is not quantitatively reproducible across devices (data from [Figure 6.5\(c\)](#) and [Figure B.2\(a\)](#) are shown in solid gray for comparison). Furthermore, comparing all four junctions we do not observe any systematic dependence on crystal orientation as one might expect for an intrinsic spin-orbit dominated effect. These results support our suggestion outlined in [Chapter 6](#) that disorder plays a key role in determining the precise magnitude and alignment of the asymmetries.

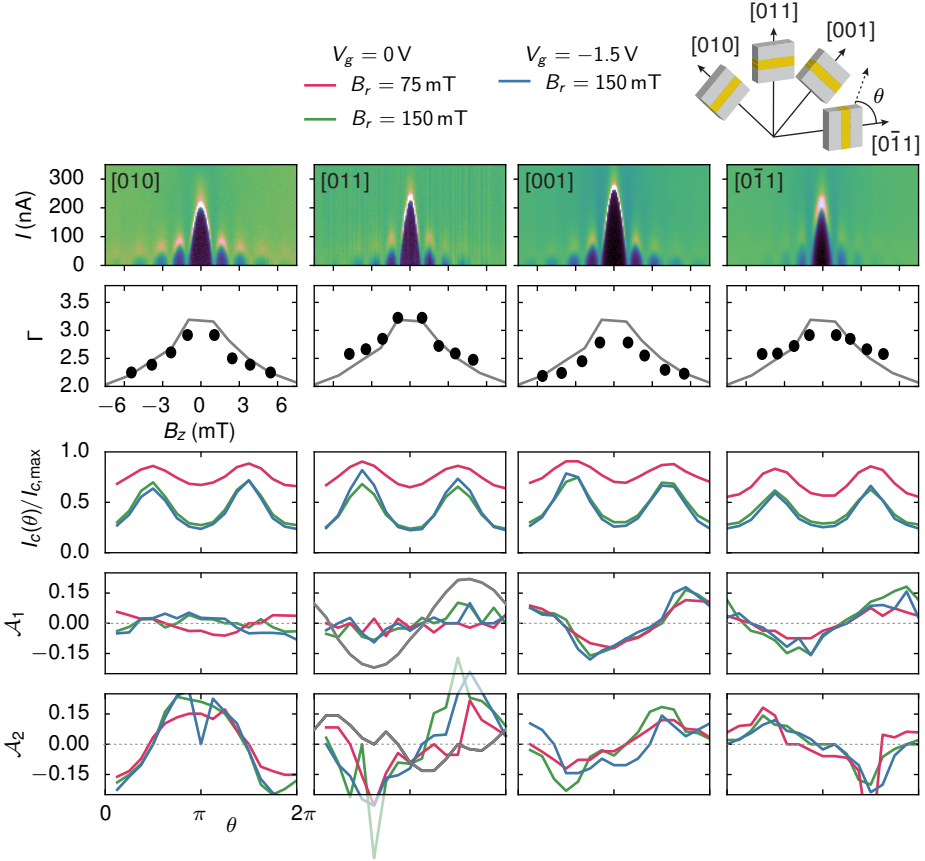


Figure B.4: **Additional devices.**(Top row) Differential resistance as function of applied current and perpendicular magnetic field for four additional devices. (Second row) Extracted field enhancement at the nodes of the interference pattern (markers). The gray line indicates the behavior of the device studied in Chapter 6. (Third row) Behavior of the critical current at $B_z = 0$, as a function of in plane field angle θ . Different curves correspond to different field magnitudes and gate voltages. Note that for all devices θ is measured with respect to the direction of current flow as indicated in the top right inset. (Fourth row) Extracted asymmetry of the first side-lobe pair \mathcal{A}_1 . The gray line for the [011] device indicates the behavior of the nominally identical device studied in Chapter 6. (Fifth row) The same for the second side-lobe pair \mathcal{A}_2 .

B.4 TIGHT BINDING SIMULATIONS

To support the suggestion of [Section 6.4.2](#) that the microscopic (disordered) structure of the junction can play a crucial role for the behavior of the asymmetries in the interference pattern, we present numerical simulations of the supercurrent through a two-dimensional disordered SNS-junction. For the normal region we write the model Hamiltonian

$$\mathcal{H}_N = \left\{ \frac{\hat{\mathbf{p}}^2}{2m} - \mu + V(x, y) \right\} \tau_z + \frac{1}{2} g \mu_B \tilde{\mathbf{B}} \cdot \boldsymbol{\sigma} + \mathcal{H}_{SO}, \quad (\text{B.5})$$

where momentum operator $\hat{\mathbf{p}} = -i\hbar\nabla_{\mathbf{r}} - e\mathbf{A}$ again includes the effect of a vector potential $\mathbf{A} = -\tilde{B}_z y \hat{x} \tau_z$. As before, we include in-plane flux focusing by making the magnetic field position-dependent: the field $\tilde{\mathbf{B}}$ is the effective field including the flux focusing, whereas \mathbf{B} is the actual applied field. Explicitly, we use

$$\tilde{\mathbf{B}}(x) = \begin{cases} (\sqrt{1-f^2}B_x, B_y, B_z + fB_x) & -L/2 \leq x < -L/2 + d_f, \\ (B_x, B_y, B_z) & -L/2 + d_f \leq x < L/2 - d_f, \\ (\sqrt{1-f^2}B_x, B_y, B_z - fB_x) & L/2 - d_f \leq x \leq L/2. \end{cases} \quad (\text{B.6})$$

The z -component of the field thus gets shifted by a $\pm fB_x$ in a strip of width d_f next to the contacts. We further include the chemical potential μ and a (possibly disordered) electronic potential $V(x, y)$ in the first term of \mathcal{H} .

The calculations that follow are based on a perturbative expansion of the free energy of the central normal region, assuming for ease of calculation weak coupling to the superconductors (see Ref. [\[194\]](#) and especially its Supplementary Material for all details of the calculation). For the numerical simulations we discretize the full Hamiltonian (B.5) for the electrons in the normal part.

In our simulations we use a 30×120 lattice with lattice constant $a = 2.5$ nm, resulting in $L = 75$ nm and $W = 300$ nm. Using an effective electronic mass of $m = 0.026 m_e$ this yields a hopping matrix element $t = \hbar^2/2ma^2 = 234$ meV. We use a Fermi wavelength of $\lambda_F = 20$ nm, which corresponds to $\mu = 0.62 t$, and a g -factor of $g = -10$, yielding a “Zeeman length” $l_Z = 2\pi\hbar v_F/|g|\mu_B B \approx 50$ μm for $B = 200$ mT. The Rashba and Dresselhaus coefficients are set to $\alpha = 1$ eV \AA and $\beta = 0.25$ eV \AA respectively, corresponding to spin-orbit lengths $\pi\hbar^2/m\alpha = 92$ nm and $\pi\hbar^2/m\beta = 368$ nm. We further take $\Delta = 0.2$ meV, such that the coherence length $\xi = \hbar v_F/\pi\Delta \approx 1.5$ μm , in the short-junction limit. The temperature is set to $T = 100$ mK and we use an NS coupling parameter $\kappa = 3$ meV. We include disorder by adding an onsite potential $V(x, y)$ with its elements picked from a uniform distribution between $[-U/2, U/2]$, where $U = (48a/l_e)^{1/2}(\mu/t)^{1/4}t$ with $l_e = 50$ nm being the effective electronic mean free path. The width of the strips where flux focusing is present is set to $d_f = 15$ nm, with its strength f as well as the in-plane field magnitude B_{\parallel} varied for different plots, see below.

The results are presented in [Figure B.5](#), [B.6](#) and [B.7](#). In [Figure B.5\(a–c\)](#) we show the interference pattern of critical currents $I_c(B_z)$ for three different disorder realizations, using $f = 10\%$ and an in-plane field of $B_r = 200$ mT oriented along the x -direction. We repeated these calculations, varying the angle θ between the in-plane field and the x -axis from 0 to 2π in 36 steps. For each interference pattern we find the local maxima, which give the $I_c^{(n)}$ as defined in [Chapter 6](#). The resulting asymmetry of the first two side lobe pairs,

$$\mathcal{A}_n = \frac{I_c^{(-n)} - I_c^{(n)}}{I_c^{(-n)} + I_c^{(n)}} \quad (\text{B.7})$$

with $n = 1, 2$, is then calculated as a function of θ . In [Figure B.5\(d–f\)](#) we present polar plots of the resulting $|\mathcal{A}_{1,2}|$ for the three disorder

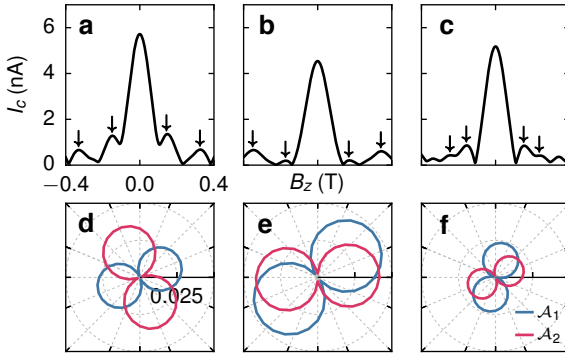


Figure B.5: **Varying disorder configuration.** (a–c) Critical current as a function of B_z for three distinct disorder configurations. In all panels an in-plane field of 200 mT is applied along B_x and other parameters are fixed as detailed in the text. The local maxima corresponding to the first two side-lobes are marked with arrows. (d–f) Lobe asymmetries $\mathcal{A}_{1,2}$, in blue and red respectively, as a function of in-plane field angle, for the disorder configurations in (a–c).

der configurations used in Figure B.5. These results can be qualitatively compared with Figure 6.5, as well as the experimental data shown in Figure B.4. We see that the overall patterns always look similar in shape, but with significant differences in both angular alignment of the maxima, as well as angular separation between the lobes. Furthermore, the overall magnitudes of the asymmetries appear to depend strongly (on the order of $\sim 100\%$) on the precise disorder configuration. In general numerical simulations yield consistently smaller asymmetries than those observed in experiment for a wide range of parameters. Furthermore, for comparable disorder strengths to those estimated experimentally (as characterized by the mean free path), the obtained diffraction patterns deviate

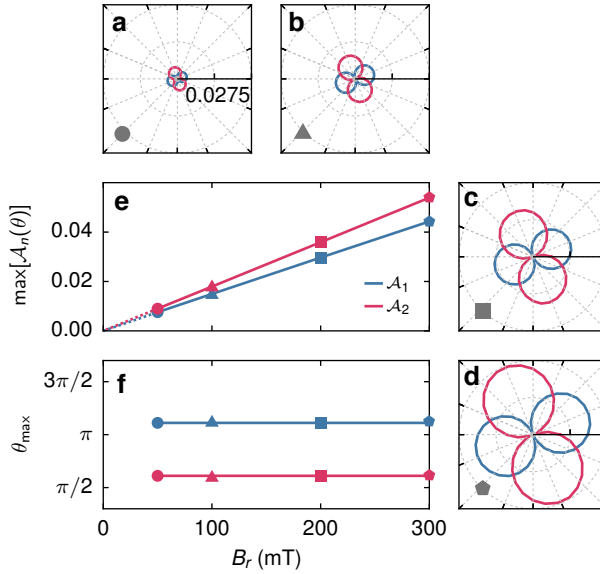


Figure B.6: **Varying Zeeman strength.** (a–d) Behavior of the side-lobe asymmetries $\mathcal{A}_{1,2}$, in blue and red respectively, as a function of in-plane field angle for increasing B_r , denoted by markers indicated in (e,f). In all plots the same disorder configuration as in Figure B.5(a,d) was used. (e) The maximum asymmetry $\max_{\theta}[\mathcal{A}_{1,2}]$ as a function of B_r . (f) The angle θ_{\max} where the maximal asymmetries occur, as a function of B_r .

strongly from the Fraunhofer form and we regularly observe a finite lifting of the nodes as seen in Figure B.5(a), incompatible with experimental observations. The reasons for these discrepancies between experiment and numerical simulations are at present not well understood.

In [Figure B.6](#) we investigate the effect of the magnitude of the in-plane field. In (a–d) we again plot the asymmetry parameters $|\mathcal{A}_{1,2}|$ using the same disorder configuration and other parameters as in [Figure B.5\(a,d\)](#), but now for different in-plane field magnitudes $B_r = 50, 100, 200,$ and 300 mT. The maximal asymmetries of the first and second lobe $\max_{\theta}[\mathcal{A}_{1,2}]$, in blue and red respectively, are shown in [Figure B.6\(e\)](#) as function of in-plane field magnitude. The dotted lines intercepting zero are added to emphasize that the model yields effectively zero asymmetry (up to floating point accuracy) in the absence of an in-plane field. Consistent with our experimental findings, the asymmetries of both lobes appear to grow linearly with different slopes. To allow for a fair comparison with [Figure 6.3](#) we track the angular position of the asymmetry maxima θ_{\max} in [Figure B.6](#) and find that changes in in-plane field strength do not affect the angular alignment of the observed asymmetry pattern. This appears to be consistent with the data presented in [Figure B.4](#) for the supplementary devices.

In [Figure B.7\(a–e\)](#) we gradually change the strength of the flux focusing, setting $f = 0\%, 1\%, 2\%, 5\%$, and 10% respectively, using the same disorder configuration as in [Figure B.5\(a,d\)](#) and [Figure B.6](#) and with $B_r = 200$ mT. We find that a change in the effective dipole has a significant effect on the angular alignment of the first lobe asymmetry \mathcal{A}_1 (blue), rotating roughly by $\pi/2$ when the dipole strength is changed from 0% to 10% , as shown explicitly in [Figure B.7\(g\)](#): In the absence of a dipole, the asymmetry is zero for a field parallel to current flow; when the dipole is strong ($f = 10\%$) the asymmetry is almost maximal in this direction. This change may indicate that there are asymmetries of different origins. The overall increase in magnitude of \mathcal{A}_1 for increasing f , as shown in [Figure B.7\(f\)](#), could support this interpretation. The largely independent behavior of the second lobe asymmetry \mathcal{A}_2 (red) in both magnitude and angular alignment as seen in (f) and (g) is currently not understood.

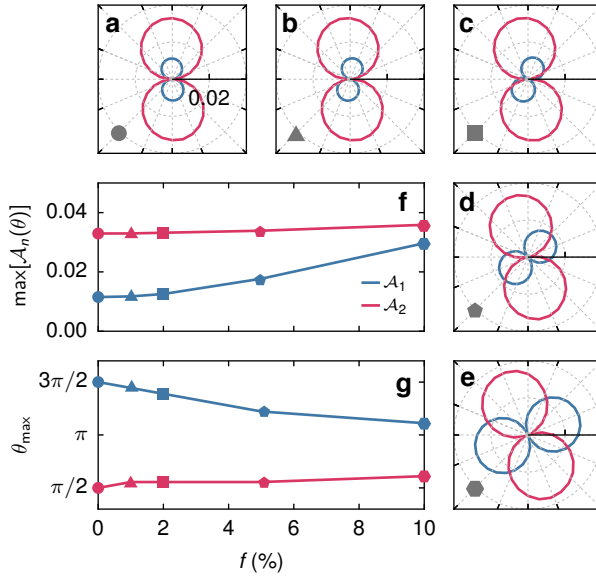


Figure B.7: **Effect of the dipole.** (a–e) Behavior of the side-lobe asymmetries $\mathcal{A}_{1,2}$, in blue and red respectively, as a function of in-plane field angle for increasing dipole strength f , denoted by markers indicated in (f,g). (f) The behavior of the maximum asymmetry $\max_n[\mathcal{A}_{1,2}]$ as a function of f . (g) The angle θ_{\max} where the maximal asymmetries occur, as a function of f .

WIRE DEVICES

C.1 SINGLE CHANNEL JUNCTION

As shown in [Figure 7.1\(c\)](#), the geometry of our sample allows for the formation of a single mode ballistic junction. In case of a junction connecting two normal metals, it is well known that the conductance G_N is proportional to the junction transmission T . This is not the case for a junction connecting a normal metal to a superconductor. In this scenario, the conductance G_S is linked to the normal state conductance G_N by [\[124\]](#):

$$G_S = 2G_0 \frac{(G_N)^2}{(2G_0 - G_N)^2} \quad (\text{C.1})$$

where $G_0 = 2e^2/h$. In our experiments we associate G_S with the zero bias conductance ($G^{V_{SD}=0}$) and G_N with the conductance measured at source drain biases larger than the superconducting gap ($G^{V_{SD}>\Delta}$). [Figure C.1](#) shows a parametric plot of $G^{V_{SD}>\Delta}$ versus $G^{V_{SD}=0}$ for various magnetic field configurations studied in the [Chapter 7](#), together with the expectation of [Eq. C.1](#) (solid black line).

In the S-S configuration (blue dots), $G^{V_{SD}=0}$ sharply increases for high transmission due to the presence of a supercurrent (not shown in [Fig. C.1](#)). On the other hand, for low transmission, the conductance in the S-S configuration is suppressed below the S-N expectation owing to the gapped densities of states on either side of the junction. The regimes attributed in the [Chapter 7](#) to S-N and S-N* behavior, $B_{\perp} = 0.08$ T (red dots) and $B_{\parallel} = 0.4$ T (red pluses)

respectively, are both in good agreement with the theoretical expectation for a single mode S-N junction over two orders of magnitude. For larger in-plane fields (green dots for $B_{\parallel} = 1.0$ T and black pluses for $B_{\parallel} = 1.8$ T), relevant for accessing the topological regime, the superconducting gap softens and the in-gap conductance behaves similarly to the S-N case. This allows us to perform direct tunneling spectroscopy and observe Majorana modes at $V_{SD} = 0$. The softening of the gap for large in-plane magnetic field is consistent with recent experiments on quasi-ballistic nanowire junctions [16]. As a guide to the eye, we also plot the proportional relation expected for a N-N junction (dashed black).

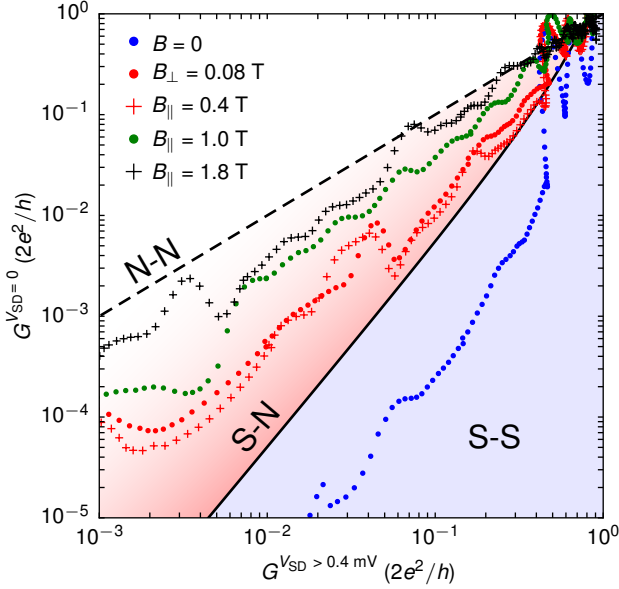


Figure C.1: **Magnetic field tuning.** Zero bias conductance $G^{V_{SD}=0}$ as a function of normal state conductance $G^{V_{SD}>0.4 \text{ mV}}$ in various field configurations. The shaded blue region denotes the expectation for a superconductor-superconductor (S-S) junction. The solid black line is the expectation for a single mode superconductor-normal (S-N) junction [124]. The dashed black line is $G^{V_{SD}=0} = G^{V_{SD}>0.4 \text{ mV}}$ as expected for a normal-normal junction (N-N).

C.2 SUPERCONDUCTING TRANSITIONS

To further elucidate the mechanisms behind the magnetic field tuning of our devices, in Fig. C.2 we compare spectroscopic data (Figs. C.2(a-h)) in two gate voltage regimes as a function of out-

of-plane and in-plane magnetic field (left and right hand side of Fig. C.2, respectively). Furthermore, we plot in Figs. C.2(i,j) the resistance of the large Al leads as a function of magnetic field, separately measured in a four terminal configuration. Figures C.2(a,b) show spectroscopic data of the wire for very low coupling ($G^{V_{SD} > 0.4 \text{ mV}} \ll 2e^2/h$), with line cuts at constant V_{SD} shown in Fig. C.2(c,d). In this case, the gate voltage is more negative than in Figure 7.3(a), and no subgap states appear. Figures C.2(e,f) and the line cuts of Figs. C.2(g,h) show results obtained for a more positive gate voltage, setting $G^{V_{SD} > 0.4 \text{ mV}} \approx 2e^2/h$ and allowing the flow of a supercurrent (visible here as a conductance enhancement up to an order of magnitude over the normal state for $V_{SD} = 0$). For perpendicular magnetic fields, the Al planes turn normal at $B_{\perp} = 0.05 \text{ T}$. This is clearly associated to the 4Δ to 2Δ transition in the tunneling regime as well as the suppression of the conductance enhancement in the open regime. The gap closing and relative rise in the $V_{SD} = 0$ conductance for $B_{\perp} = 0.45 \text{ T}$ marks the collapse of the superconductivity in the Al wire. For an in-plane magnetic field, the 4Δ to 2Δ transition and the suppression of the supercurrent are markedly different, with only the latter coinciding with the critical field of the Al planes ($B_{\parallel} = 1.3 \text{ T}$). As discussed further with reference of Fig. C.3, $B_{\parallel} = 0.3 \text{ T}$ marks instead the typical field scale necessary to lift the hard gap in the superconducting density of states below the large Al planes. Above $B_{\parallel} = 0.3 \text{ T}$, the wire is effectively probed by a constant density of states.

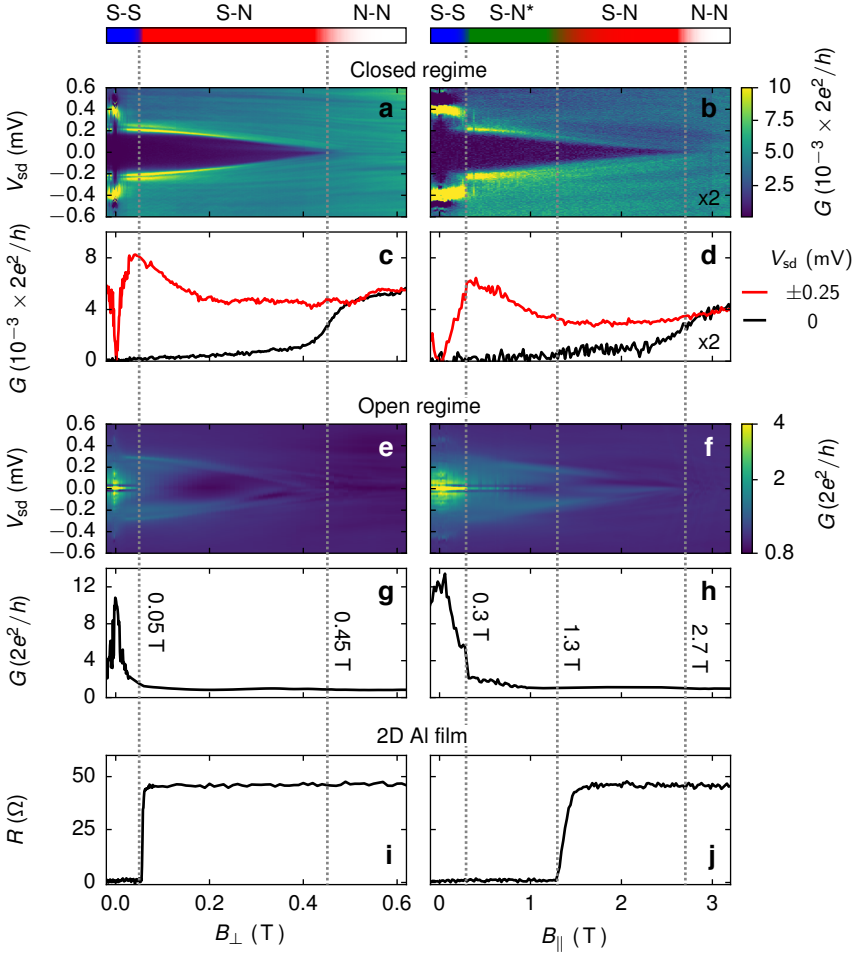


Figure C.2: **Open and closed regimes** Conductance as a function of bias and perpendicular (a) and parallel (b) magnetic fields in the tunneling regime. Line cuts are shown in (c) and (d), at both $V_{sd} = 0$ (black line) and $V_{sd} = \pm 0.25$ mV (red). Note that in (b) and (d) the conductance has been scaled up by a factor of two to allow for plotting on the same colorscale. Similarly in (e–h) the dependence of the conductance on magnetic field is shown in the open regime. The resistance of the Al film is shown in (i) and (j) for B_{\perp} and B_{\parallel} respectively.

C.3 S-QPC-N AND S-QPC-S

To directly probe the magnetic field evolution of the superconducting density of states below a large Al plane, we perform tunneling measurements from a normal contact (Fig. C.3(a), S-N configuration) and between two symmetric Al planes (Fig. C.3(e), S-S configuration). In both cases the tunneling probe is given by two evaporated Ti/Au gates defining a quantum point contact in the InAs 2DEG, similarly to Ref. [156]. Tunneling spectroscopy as a function of an in-plane magnetic field aligned along or perpendicular to the current direction (B_{\parallel} and B_{\perp} respectively), are shown in Fig. C.3(b,c,f,g). As expected, the zero field conductance shows a 2Δ gap in the S-N configuration and a 4Δ in the S-S configuration. Further inspection reveals the in-gap conductance suppression for the S-S configuration is much stronger than in the S-N case, as discussed with reference to Fig. C.1. In both configurations, an in-plane field above 200 mT lifts the in-gap conductance. In the S-N configuration it is evident the inducing subgap conductance does not influence the gap size, which is largely unaffected for $B < 400$ mT. In the S-S configuration, however, the convolution of the two DOS yields four peaks in conductance at $\pm 2\Delta$ and $\pm\Delta$. As the field is increased further towards $B_{\parallel} = 0.4$ T the $\pm\Delta$ edges are independent of field. In conclusion, both devices demonstrate that for magnetic fields of the order of 400 mT, the superconducting gap measured in a 2D geometry stays roughly constant, however with a significant increase in the subgap conductance.

C.4 SUBGAP STATE G-FACTORS

To investigate the extent of the gate-tuneability of 2DEG under the Al wire, in Figure C.4 we investigate the g-factors of Andreev bound states as a function of gate voltage at $B = 1$ T. Figure C.4(a) shows the the tunneling conductance as a function of source-drain

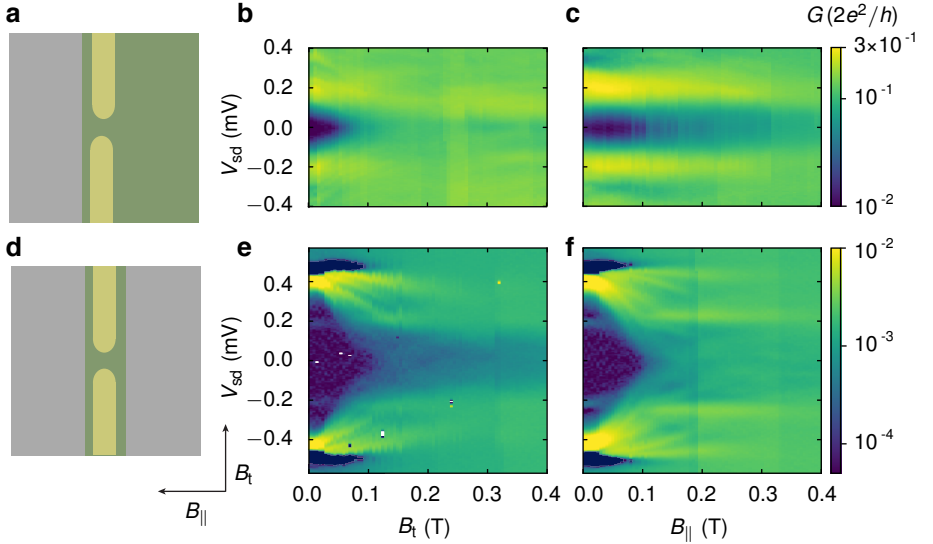


Figure C.3: **Behavior of proximitized 2D regions.**(a) Schematic of a S-QPC-N geometry with the corresponding field dependence of the measured superconducting gap shown in (b) and (c) for magnetic fields applied along B_t and $B_{||}$ respectively. Both fields are in the plane of the 2DEG as shown in (e). (d–f) similarly for a S-QPC-S geometry.

bias and gate voltage, revealing a spectrum of subgap Andreev bound states. By measuring the evolution of these states in magnetic field at different gate voltages as shown in Figure C.4(c–f) we extracted the g-factors of the individual states, shown in Figure C.4(b) by the black dots. The red line indicates the average g-factor at a given gate voltage. Below $V_g = -2.88$ V (indicated by the blue shading), no subgap states are visible, and the g-factor is estimated from the closing of the superconducting gap.

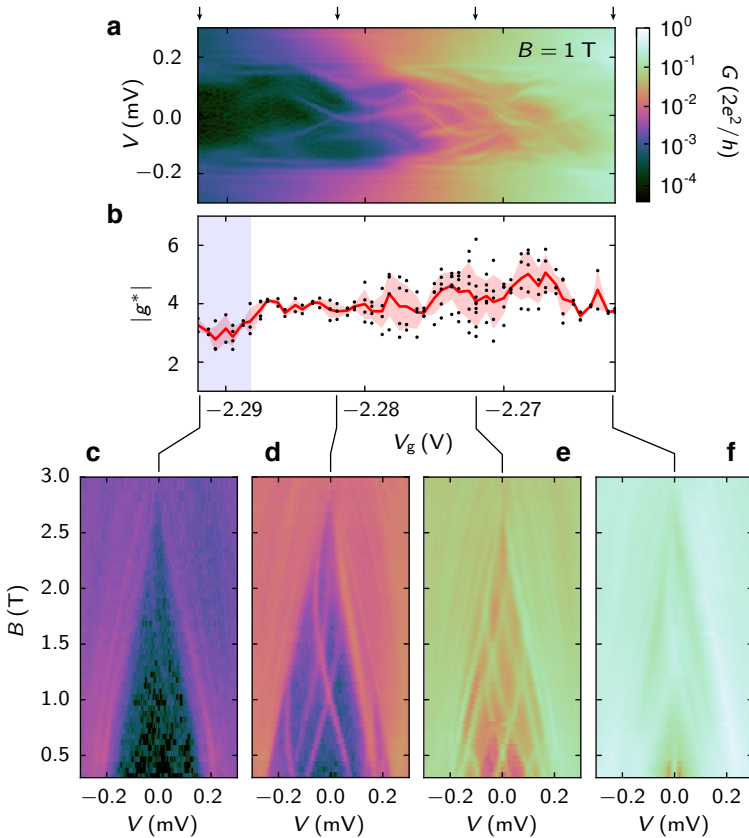


Figure C.4: **Dependence of g factor on gate voltage.** (a) Conductance as a function of gate voltage and source-drain bias at $B = 1$ T. (c–f) Conductance as a function of magnetic field and source-drain bias, revealing the g -factors of subgap Andreev bound states. The extracted values for all visible states are plotted in (b) as a function of gate voltage (black points). The average g -factor at each gate voltage is shown by the red line. The blue shading indicates that no subgap states can be resolved and the g -factor is estimated from the slope of the collapsing superconducting gap.

BIBLIOGRAPHY

- [1] J. Bardeen and W. H. Brattain. "The transistor, a semi-conductor triode." *Physical Review* 74.2 (1948), p. 230.
- [2] W. Shockley. "Transistor technology evokes new physics." *Nobel lecture* (1956), pp. 344–374.
- [3] J. S. Kilby. *Miniaturized electronic circuits*. US Patent 3,138,743. June 1964.
- [4] L. L. Sohn, L. P. Kouwenhoven, and G. Schön. *Mesoscopic electron transport*. Vol. 345. Berlin: Springer Science & Business Media, 2013.
- [5] A. T. Johnson, L. P. Kouwenhoven, W. de Jong, N. C. van der Vaart, C. J. P. M. Harmans, and C. T. Foxon. "Zero-dimensional states and single electron charging in quantum dots." *Phys. Rev. Lett.* 69 (10 1992), pp. 1592–1595. DOI: [10.1103/PhysRevLett.69.1592](https://doi.org/10.1103/PhysRevLett.69.1592).
- [6] C. M. Marcus, A. J. Rimberg, R. M. Westervelt, P. F. Hopkins, and A. C. Gossard. "Conductance fluctuations and chaotic scattering in ballistic microstructures." *Phys. Rev. Lett.* 69 (3 1992), pp. 506–509. DOI: [10.1103/PhysRevLett.69.506](https://doi.org/10.1103/PhysRevLett.69.506).
- [7] B. Van Wees, H Van Houten, C. Beenakker, J. G. Williamson, L. Kouwenhoven, D Van der Marel, and C. Foxon. "Quantized conductance of point contacts in a two-dimensional electron gas." *Phys. Rev. Lett.* 60.9 (1988), p. 848.
- [8] B. J. van Wees, L. P. Kouwenhoven, C. J. P. M. Harmans, J. G. Williamson, C. E. Timmering, M. E. I. Broekaart, C. T. Foxon, and J. J. Harris. "Observation of zero-dimensional states in a one-dimensional electron interferometer." *Phys. Rev. Lett.*

- 62 (21 1989), pp. 2523–2526. DOI: [10.1103/PhysRevLett.62.2523](https://doi.org/10.1103/PhysRevLett.62.2523).
- [9] H. K. Onnes. “Investigations into the properties of substances at low temperatures, which have led, amongst other things, to the preparation of liquid helium.” *Nobel lecture* 4 (1913).
- [10] B. Josephson. “Possible new effects in superconductive tunnelling.” *Physics Letters* 1.7 (1962), pp. 251–253. DOI: [http://dx.doi.org/10.1016/0031-9163\(62\)91369-0](http://dx.doi.org/10.1016/0031-9163(62)91369-0).
- [11] B. D. Josephson. “The discovery of tunnelling supercurrents.” *Rev. Mod. Phys.* 46 (2 1974), pp. 251–254. DOI: [10.1103/RevModPhys.46.251](https://doi.org/10.1103/RevModPhys.46.251).
- [12] V. Mourik, K. Zuo, S. M. Frolov, S. R. Plissard, E. P. A. M. Bakkers, and L. P. Kouwenhoven. “Signatures of Majorana Fermions in Hybrid Superconductor-Semiconductor Nanowire Devices.” *Science* 336.6084 (2012), pp. 1003–1007. DOI: [10.1126/science.1222360](https://doi.org/10.1126/science.1222360).
- [13] A. Das, Y. Ronen, Y. Most, Y. Oreg, M. Heiblum, and H. Shtrikman. “Zero-bias peaks and splitting in an Al-InAs nanowire topological superconductor as a signature of Majorana fermions.” *Nat. Phys.* 8.12 (2012), pp. 887–895.
- [14] M. T. Deng, C. L. Yu, G. Y. Huang, M. Larsson, P. Caroff, and H. Q. Xu. “Anomalous Zero-Bias Conductance Peak in a Nb-InSb Nanowire-Nb Hybrid Device.” *Nano Lett.* 12.12 (2012), pp. 6414–6419. DOI: [10.1021/nl303758w](https://doi.org/10.1021/nl303758w).
- [15] H. O. H. Churchill, V. Fatemi, K. Grove-Rasmussen, M. T. Deng, P. Caroff, H. Q. Xu, and C. M. Marcus. “Superconductor-nanowire devices from tunneling to the multichannel regime: Zero-bias oscillations and magnetoconductance crossover.” *Phys. Rev. B* 87 (24 2013), p. 241401. DOI: [10.1103/PhysRevB.87.241401](https://doi.org/10.1103/PhysRevB.87.241401).

- [16] H. Zhang, Ö. Gül, S. Conesa-Boj, K. Zuo, V. Mourik, F. K. de Vries, J. van Veen, D. J. van Woerkom, M. P. Nowak, M. Wimmer, D. Car, S. Plissard, E. P. A. M. Bakkers, M. Quintero-Pérez, S. Goswami, K. Watanabe, T. Taniguchi, and L. P. Kouwenhoven. "Ballistic Majorana nanowire devices." *ArXiv e-prints* (Mar. 2016).
- [17] M. T. Deng, S. Vaitiekenas, E. B. Hansen, J. Danon, M. Lei-jinse, K. Flensberg, J. Nygård, P. Krogstrup, and C. M. Marcus. "Majorana bound state in a coupled quantum-dot hybrid-nanowire system." *Science* 354.6319 (2016), pp. 1557–1562. DOI: [10.1126/science.aaf3961](https://doi.org/10.1126/science.aaf3961).
- [18] N. Ashcroft and N. Mermin. *Solid State Physics*. Philadelphia: Saunders College Publishing, 1976.
- [19] D. C. Tsui. "Observation of Surface Bound State and Two-Dimensional Energy Band by Electron Tunneling." *Phys. Rev. Lett.* 24 (7 1970), pp. 303–306. DOI: [10.1103/PhysRevLett.24.303](https://doi.org/10.1103/PhysRevLett.24.303).
- [20] M. Noguchi, K. Hirakawa, and T. Ikoma. "Intrinsic electron accumulation layers on reconstructed clean InAs(100) surfaces." *Phys. Rev. Lett.* 66 (17 1991), pp. 2243–2246. DOI: [10.1103/PhysRevLett.66.2243](https://doi.org/10.1103/PhysRevLett.66.2243).
- [21] L. O. Olsson, C. B. M. Andersson, M. C. Håkansson, J. Kanski, L. Ilver, and U. O. Karlsson. "Charge Accumulation at InAs Surfaces." *Phys. Rev. Lett.* 76 (19 1996), pp. 3626–3629. DOI: [10.1103/PhysRevLett.76.3626](https://doi.org/10.1103/PhysRevLett.76.3626).
- [22] K. Horn. "Chapter 7 - Electronic Structure of Semiconductor Surfaces." *Electronic Structure*. Ed. by K. Horn and M. Scheffler. Vol. 2. Handbook of Surface Science. Amsterdam: North-Holland, 2000, pp. 383–431. DOI: [https://doi.org/10.1016/S1573-4331\(00\)80011-6](https://doi.org/10.1016/S1573-4331(00)80011-6).

- [23] W. Mönch. *Semiconductor Surfaces and Interfaces*. 3rd ed. Springer Series in Surface Sciences 26. Springer-Verlag Berlin Heidelberg, 2001.
- [24] L. F. J. Piper, T. D. Veal, M. J. Lowe, and C. F. McConville. “Electron depletion at InAs free surfaces: Doping-induced acceptorlike gap states.” *Phys. Rev. B* 73 (19 2006), p. 195321. DOI: [10.1103/PhysRevB.73.195321](https://doi.org/10.1103/PhysRevB.73.195321).
- [25] N. Olszowska, J. Lis, P. Ciochon, L. Walczak, E. G. Michel, and J. J. Kolodziej. “Effect of a skin-deep surface zone on the formation of a two-dimensional electron gas at a semiconductor surface.” *Phys. Rev. B* 94 (11 2016), p. 115305. DOI: [10.1103/PhysRevB.94.115305](https://doi.org/10.1103/PhysRevB.94.115305).
- [26] C. Weisbuch and B. Vinter. *Quantum Semiconductor Structures: Fundamentals and Applications*. Boston: Academic Press, 1991.
- [27] V. Radantsev, T. Deryabina, L. Zverev, I Kulaev, and S. Kholmotova. “Subband structure and scattering mechanisms of a surface two-dimensional electron gas in heavily-doped InAs.” *Zh. Eksp. Teor. Fiz* 91 (1986), pp. 1016–1029.
- [28] F. Stern and W. E. Howard. “Properties of Semiconductor Surface Inversion Layers in the Electric Quantum Limit.” *Phys. Rev.* 163 (3 1967), pp. 816–835. DOI: [10.1103/PhysRev.163.816](https://doi.org/10.1103/PhysRev.163.816).
- [29] I Vurgaftman, J. Meyer, and L. Ram-Mohan. “Band parameters for III–V compound semiconductors and their alloys.” *Journal of applied physics* 89.11 (2001), pp. 5815–5875.
- [30] A. Y. Cho and J. Arthur. “Molecular beam epitaxy.” *Progress in Solid State Chemistry* 10 (1975), pp. 157–191.
- [31] B. A. Joyce. “Molecular beam epitaxy.” *Reports on Progress in Physics* 48.12 (1985), p. 1637.

- [32] J. R. Arthur. "Molecular beam epitaxy." *Surface Science* 500.1 (2002), pp. 189–217.
- [33] C. Chang, E. Mendez, L. Chang, and L. Esaki. "Quantum wells of InAs between AlSb." *Surface Science* 142.1 (1984), pp. 598–602. DOI: [http://dx.doi.org/10.1016/0039-6028\(84\)90368-6](http://dx.doi.org/10.1016/0039-6028(84)90368-6).
- [34] J. Nitta, T. Akazaki, H. Takayanagi, and K. Arai. "Transport properties in an InAs-inserted-channel $\text{In}_{0.52}\text{Al}_{0.48}\text{As}/\text{In}_{0.53}\text{Ga}_{0.47}\text{As}$ heterostructure coupled superconducting junction." *Phys. Rev. B* 46 (21 1992), pp. 14286–14289. DOI: [10.1103/PhysRevB.46.14286](https://doi.org/10.1103/PhysRevB.46.14286).
- [35] T. Ihn. *Semiconductor Nanostructures: Quantum states and electronic transport*. Oxford: Oxford University Press, 2010.
- [36] G. Stillman and C. Wolfe. "Electrical characterization of epitaxial layers." *Thin Solid Films* 31.1 (1976), pp. 69–88. DOI: [http://dx.doi.org/10.1016/0040-6090\(76\)90355-2](http://dx.doi.org/10.1016/0040-6090(76)90355-2).
- [37] L. H. Thomas. "The motion of a spinning electron." *Nature* 117 (1926), p. 514. DOI: [10.1038/117514a0](https://doi.org/10.1038/117514a0).
- [38] L. Thomas. "I. The kinematics of an electron with an axis." *The London, Edinburgh, and Dublin Philosophical Magazine and Journal of Science* 3.13 (1927), pp. 1–22. DOI: [10.1080/14786440108564170](https://doi.org/10.1080/14786440108564170).
- [39] V. Lechner. "Bulk and structure inversion asymmetry in semiconductor quantum well structures." PhD thesis. Universität Regensburg, 2012.
- [40] A. N. Chantis, M. van Schilfgaarde, and T. Kotani. "Ab Initio." *Phys. Rev. Lett.* 96 (8 2006), p. 086405. DOI: [10.1103/PhysRevLett.96.086405](https://doi.org/10.1103/PhysRevLett.96.086405).

- [41] G. W. Winkler, D. Varjas, R. Skolasinski, A. A. Soluyanov, M. Troyer, and M. Wimmer. "Orbital Contributions to the Electron g Factor in Semiconductor Nanowires." *Phys. Rev. Lett.* 119 (3 2017), p. 037701. DOI: [10.1103/PhysRevLett.119.037701](https://doi.org/10.1103/PhysRevLett.119.037701).
- [42] M. Valín-Rodríguez and R. G. Nazmitdinov. "Model for spin-orbit effects in two-dimensional semiconductors in magnetic fields." *Phys. Rev. B* 73 (23 2006), p. 235306. DOI: [10.1103/PhysRevB.73.235306](https://doi.org/10.1103/PhysRevB.73.235306).
- [43] M. Büttiker. "Quantized transmission of a saddle-point constriction." *Phys. Rev. B* 41 (11 1990), pp. 7906–7909. DOI: [10.1103/PhysRevB.41.7906](https://doi.org/10.1103/PhysRevB.41.7906).
- [44] J. Connor. "On the analytical description of resonance tunnelling reactions." *Molecular Physics* 15.1 (1968), pp. 37–46. DOI: [10.1080/00268976800100791](https://doi.org/10.1080/00268976800100791).
- [45] W. H. Miller. "Uniform Semiclassical Approximations for Elastic Scattering and Eigenvalue Problems." *The Journal of Chemical Physics* 48.1 (1968), pp. 464–467. DOI: [10.1063/1.1667946](https://doi.org/10.1063/1.1667946).
- [46] B. J. van Wees, L. P. Kouwenhoven, H. van Houten, C. W. J. Beenakker, J. E. Mooij, C. T. Foxon, and J. J. Harris. "Quantized conductance of magnetoelectric subbands in ballistic point contacts." *Phys. Rev. B* 38 (5 1988), pp. 3625–3627. DOI: [10.1103/PhysRevB.38.3625](https://doi.org/10.1103/PhysRevB.38.3625).
- [47] D. A. Wharam, T. J. Thornton, R. Newbury, M. Pepper, H. Ahmed, J. E. F. Frost, D. G. Hasko, D. C. Peacock, D. A. Ritchie, and G. A. C. Jones. "One-dimensional transport and the quantisation of the ballistic resistance." *Journal of Physics C: Solid State Physics* 21.8 (1988), p. L209.

- [48] G. C. Gardner, S. Fallahi, J. D. Watson, and M. J. Manfra. "Modified MBE hardware and techniques and role of gallium purity for attainment of two dimensional electron gas mobility $> 35 \times 10^6$ cm²/Vs in AlGaAs/GaAs quantum wells grown by MBE." *Journal of Crystal Growth* 441 (2016), pp. 71–77. DOI: [10.1016/j.jcrysgro.2016.02.010](https://doi.org/10.1016/j.jcrysgro.2016.02.010).
- [49] T. Tschirky, S. Mueller, C. A. Lehner, S. Fält, T. Ihn, K. Ensslin, and W. Wegscheider. "Scattering mechanisms of highest-mobility InAs/Al_xGa_{1-x}Sb quantum wells." *Phys. Rev. B* 95 (11 2017), p. 115304. DOI: [10.1103/PhysRevB.95.115304](https://doi.org/10.1103/PhysRevB.95.115304).
- [50] W. Yi, A. A. Kiselev, J. Thorp, R. Noah, B.-M. Nguyen, S. Bui, R. D. Rajavel, T. Hussain, M. F. Gyure, P. Kratz, Q. Qian, M. J. Manfra, V. S. Pribiag, L. P. Kouwenhoven, C. M. Marcus, and M. Sokolich. "Gate-tunable high mobility remote-doped InSb/In_{1-x}Al_xSb quantum well heterostructures." *Applied Physics Letters* 106.14 (2015), p. 142103. DOI: [10.1063/1.4917027](https://doi.org/10.1063/1.4917027).
- [51] R. Winkler. *Spin–Orbit Coupling Effects in Two-Dimensional Electron and Hole Systems*. Springer Berlin Heidelberg, 2003. DOI: [10.1007/b13586](https://doi.org/10.1007/b13586).
- [52] J. Bardeen, L. N. Cooper, and J. R. Schrieffer. "Theory of Superconductivity." *Phys. Rev.* 108 (5 1957), pp. 1175–1204. DOI: [10.1103/PhysRev.108.1175](https://doi.org/10.1103/PhysRev.108.1175).
- [53] P. De Gennes. *Superconductivity Of Metals And Alloys*. New York: Benjamin, 1993.
- [54] M. Tinkham. *Introduction to Superconductivity*. New York: Dover, 2004.

- [55] G. E. Blonder, M Tinkham, and T Klapwijk. "Transition from metallic to tunneling regimes in superconducting microconstrictions: Excess current, charge imbalance, and supercurrent conversion." *Phys. Rev. B* 25:7 (Apr. 1982), pp. 4515–4532.
- [56] E. M. Spanton, M. Deng, S. Vaitiekėnas, P. Krogstrup, J. Nygård, C. M. Marcus, and K. A. Moler. "Current–phase relations of few-mode InAs nanowire Josephson junctions." *Nature Physics* (2017). DOI: [10.1038/nphys4224](https://doi.org/10.1038/nphys4224).
- [57] I. O. Kulik. "Macroscopic Quantization and the Proximity Effect in S-N-S Junctions." *Soviet Journal of Experimental and Theoretical Physics* 30 (1969), p. 944.
- [58] W. Haberkorn, H. Knauer, and J. Richter. "A theoretical study of the current-phase relation in Josephson contacts." *physica status solidi (a)* 47:2 (1978), K161–K164. DOI: [10.1002/pssa.2210470266](https://doi.org/10.1002/pssa.2210470266).
- [59] G. B. Arnold. "Superconducting tunneling without the tunneling Hamiltonian." *Journal of Low Temperature Physics* 59:1 (1985), pp. 143–183. DOI: [10.1007/BF00681510](https://doi.org/10.1007/BF00681510).
- [60] A. Furusaki and M. Tsukada. "A unified theory of clean Josephson junctions." *Physica B: Condensed Matter* 165 (1990), pp. 967–968. DOI: [http://dx.doi.org/10.1016/S0921-4526\(09\)80069-0](http://dx.doi.org/10.1016/S0921-4526(09)80069-0).
- [61] A. V. Zaitsev. "Quasiclassical equations of the theory of superconductivity for contiguous metals and the properties of constricted microcontacts." *Zh. Eksp. Teor. Fiz* 86 (1984), pp. 1742–1758.
- [62] L. Glazman and K. Matveev. "Resonant Josephson current through Kondo impurities in a tunnel barrier." *JETP Lett.* 49:10 (1989), pp. 659–662.

- [63] P. F. Bagwell. "Suppression of the Josephson current through a narrow, mesoscopic, semiconductor channel by a single impurity." *Phys. Rev. B* 46 (19 1992), pp. 12573–12586. DOI: [10.1103/PhysRevB.46.12573](https://doi.org/10.1103/PhysRevB.46.12573).
- [64] C. W. J. Beenakker and H van Houten. "Josephson current through a superconducting quantum point contact shorter than the coherence length." *Phys. Rev. Lett.* 66.23 (June 1991), pp. 3056–3059.
- [65] A. Furusaki, H. Takayanagi, and M. Tsukada. "Josephson effect of the superconducting quantum point contact." *Phys. Rev. B* 45 (18 1992), pp. 10563–10575. DOI: [10.1103/PhysRevB.45.10563](https://doi.org/10.1103/PhysRevB.45.10563).
- [66] I. Kulik and A. Omel'Yanchuk. "Properties of superconducting microbridges in the pure limit." *Sov. J. Low Temp. Phys.(Engl. Transl.);(United States)* 3.7 (1977).
- [67] E. Majorana. "Teoria simmetrica dell'ettrone e del positrone." *Il Nuovo Cimento (1924-1942)* 14.4 (1937), p. 171.
- [68] P. W. Anderson. "More Is Different." *Science* 177.4047 (1972), pp. 393–396. DOI: [10.1126/science.177.4047.393](https://doi.org/10.1126/science.177.4047.393).
- [69] N. Read and D. Green. "Paired states of fermions in two dimensions with breaking of parity and time-reversal symmetries and the fractional quantum Hall effect." *Phys. Rev. B* 61 (15 2000), pp. 10267–10297. DOI: [10.1103/PhysRevB.61.10267](https://doi.org/10.1103/PhysRevB.61.10267).
- [70] A. Y. Kitaev. "Unpaired Majorana fermions in quantum wires." *Physics-Uspekhi* 44.10S (2001), p. 131.
- [71] R. M. Lutchyn, J. D. Sau, and S. Das Sarma. "Majorana Fermions and a Topological Phase Transition in Semiconductor-Superconductor Heterostructures." *Phys. Rev. Lett.* 105 (7 2010), p. 077001. DOI: [10.1103/PhysRevLett.105.077001](https://doi.org/10.1103/PhysRevLett.105.077001).

- [72] Y. Oreg, G. Refael, and F. von Oppen. "Helical Liquids and Majorana Bound States in Quantum Wires." *Phys. Rev. Lett.* 105 (17 2010), p. 177002. DOI: [10.1103/PhysRevLett.105.177002](https://doi.org/10.1103/PhysRevLett.105.177002).
- [73] P. W. Anderson and J. M. Rowell. "Probable Observation of the Josephson Superconducting Tunneling Effect." *Phys. Rev. Lett.* 10 (6 1963), pp. 230–232. DOI: [10.1103/PhysRevLett.10.230](https://doi.org/10.1103/PhysRevLett.10.230).
- [74] P. Cardinne, J. Nordman, and M. Renard. "On the use of low barrier potential materials to improve high frequency coupling to Josephson tunnel junctions." *Revue de Physique Appliquée* 9.1 (1974), pp. 167–171. DOI: [10.1051/rphysap:0197400901016700](https://doi.org/10.1051/rphysap:0197400901016700).
- [75] C. L. Huang and T. Van Duzer. "Josephson tunneling through locally thinned silicon wafers." *Appl. Phys. Lett.* 25.12 (1974), pp. 753–756. DOI: <http://dx.doi.org/10.1063/1.1655388>.
- [76] C. Huang and T. V. Duzer. "Single-crystal silicon-barrier Josephson junctions." *IEEE Transactions on Magnetics* 11.2 (1975), pp. 766–769. DOI: [10.1109/TMAG.1975.1058702](https://doi.org/10.1109/TMAG.1975.1058702).
- [77] T. Nishino, M. Miyake, Y. Harada, and U. Kawabe. "Three-terminal superconducting device using a Si single-crystal film." *IEEE Electron Device Letters* 6.6 (1985), pp. 297–299. DOI: [10.1109/EDL.1985.26131](https://doi.org/10.1109/EDL.1985.26131).
- [78] H. Takayanagi and T. Kawakami. "Superconducting Proximity Effect in the Native Inversion Layer on InAs." *Phys. Rev. Lett.* 54 (22 1985), pp. 2449–2452. DOI: [10.1103/PhysRevLett.54.2449](https://doi.org/10.1103/PhysRevLett.54.2449).
- [79] J. M. Rowell. "Magnetic Field Dependence of the Josephson Tunnel Current." *Phys. Rev. Lett.* 11 (5 1963), pp. 200–202. DOI: [10.1103/PhysRevLett.11.200](https://doi.org/10.1103/PhysRevLett.11.200).

- [80] K. Inoue and T. Kawakami. "Magnetic field dependencies of critical currents in InAs-coupled Josephson junctions." *J. Appl. Phys.* 65.4 (1989), p. 1631. DOI: [10.1063/1.342930](https://doi.org/10.1063/1.342930).
- [81] A. W. Kleinsasser, T. N. Jackson, G. D. Pettit, H. Schmid, J. M. Woodall, and D. P. Kern. "n-InAs/GaAs heterostructure superconducting weak links with Nb electrodes." *Appl. Phys. Lett.* 49.25 (1986), pp. 1741–1743. DOI: [10.1063/1.97233](https://doi.org/10.1063/1.97233).
- [82] C. Nguyen, J. Werking, H. Kroemer, and E. L. Hu. "InAsAlSb quantum well as superconducting weak link with high critical current density." *Appl. Phys. Lett.* 57.1 (1990), pp. 87–89. DOI: <http://dx.doi.org/10.1063/1.103546>.
- [83] H. Takayanagi, T. Akazaki, and J. Nitta. "Observation of Maximum Supercurrent Quantization in a Superconducting Quantum Point Contact." *Phys. Rev. Lett.* 75 (19 1995), pp. 3533–3536. DOI: [10.1103/PhysRevLett.75.3533](https://doi.org/10.1103/PhysRevLett.75.3533).
- [84] A Chrestin, T Matsuyama, and U Merkt. "Evidence for a proximity-induced energy gap in Nb/InAs/Nb junctions." *Phys. Rev. B* 55.13 (Apr. 1997), pp. 8457–8465.
- [85] P. H. C. Magnée, S. G. den Hartog, B. J. v. Wees, T. M. Klapwijk, W. van de Graaf, and G. Borghs. "Influence of low energy Ar sputtering on the electronic properties of InAs based quantum well structures." *Appl. Phys. Lett.* 67.24 (1995), pp. 3569–3571. DOI: <http://dx.doi.org/10.1063/1.115320>.
- [86] K. Neurohr, A. A. Golubov, T. Klocke, J. Kaufmann, T. Schäpers, J. Appenzeller, D. Uhlisch, A. V. Ustinov, M. Hollfelder, H. Lüth, and A. I. Braginski. "Properties of lateral Nb contacts to a two-dimensional electron gas in an $\text{In}_{0.77}\text{Ga}_{0.23}\text{As}/\text{InP}$ heterostructure." *Phys. Rev. B* 54 (23 1996), pp. 17018–17028. DOI: [10.1103/PhysRevB.54.17018](https://doi.org/10.1103/PhysRevB.54.17018).

- [87] T. Schäpers. *Superconductor/Semiconductor Junctions*. Vol. 174. Springer Tracts in Modern Physics. Berlin, Heidelberg: Springer, 2001.
- [88] Y.-J. Doh, J. A. van Dam, A. L. Roest, E. P. A. M. Bakkers, L. P. Kouwenhoven, and S. De Franceschi. "Tunable Supercurrent Through Semiconductor Nanowires." *Science* 309.5732 (Aug. 2005), pp. 272–275.
- [89] J. A. Van Dam, Y. V. Nazarov, E. P. Bakkers, S. De Franceschi, and L. P. Kouwenhoven. "Supercurrent reversal in quantum dots." *Nature* 442.7103 (2006), pp. 667–670.
- [90] J. Xiang, A. Vidan, M. Tinkham, R. M. Westervelt, and C. M. Lieber. "Ge/Si nanowire mesoscopic Josephson junctions." *Nature Nanotechnology* 1.3 (Dec. 2006), pp. 208–213.
- [91] E. J. Lee, X. Jiang, M. Houzet, R. Aguado, C. M. Lieber, and S. De Franceschi. "Spin-resolved Andreev levels and parity crossings in hybrid superconductor-semiconductor nanostructures." *Nature nanotechnology* 9.1 (2014), pp. 79–84.
- [92] S. Takei, B. M. Fregoso, H.-Y. Hui, A. M. Lobos, and S. Das Sarma. "Soft Superconducting Gap in Semiconductor Majorana Nanowires." *Phys. Rev. Lett.* 110.18 (Apr. 2013), p. 186803.
- [93] M. Millea, A. Silver, and L. Flesner. "Superconducting contacts to p-InAs." *IEEE Trans. Magn.* 15.1 (1979), pp. 435–438. DOI: [10.1109/TMAG.1979.1060276](https://doi.org/10.1109/TMAG.1979.1060276).
- [94] A. F. Morpurgo, S. Holl, B. J. van Wees, T. M. Klapwijk, and G. Borghs. "Phase Conjugated Andreev Backscattering in Two-Dimensional Ballistic Cavities." *Phys. Rev. Lett.* 78 (13 1997), pp. 2636–2639. DOI: [10.1103/PhysRevLett.78.2636](https://doi.org/10.1103/PhysRevLett.78.2636).

- [95] J. P. Heida, B. J. van Wees, T. M. Klapwijk, and G. Borghs. "Critical currents in ballistic two-dimensional InAs-based superconducting weak links." *Phys. Rev. B* 60 (18 1999), pp. 13135–13138. DOI: [10.1103/PhysRevB.60.13135](https://doi.org/10.1103/PhysRevB.60.13135).
- [96] F. Deon, V. Pellegrini, F. Giazotto, G. Biasiol, L. Sorba, and F. Beltram. "Proximity effect in a two-dimensional electron gas probed with a lateral quantum dot." *Phys. Rev. B* 84 (10 2011), p. 100506. DOI: [10.1103/PhysRevB.84.100506](https://doi.org/10.1103/PhysRevB.84.100506).
- [97] H. Irie, Y. Harada, H. Sugiyama, and T. Akazaki. "Josephson coupling through one-dimensional ballistic channel in semiconductor-superconductor hybrid quantum point contacts." *Phys. Rev. B* 89 (16 2014), p. 165415. DOI: [10.1103/PhysRevB.89.165415](https://doi.org/10.1103/PhysRevB.89.165415).
- [98] Z. Wan, A. Kazakov, M. J. Manfra, L. N. Pfeiffer, K. W. West, and L. P. Rokhinson. "Induced superconductivity in high-mobility two-dimensional electron gas in gallium arsenide heterostructures." *Nat. Commun.* 6 (2015).
- [99] C. Nguyen, H. Kroemer, and E. L. Hu. "Anomalous Andreev conductance in InAs-AlSb quantum well structures with Nb electrodes." *Phys. Rev. Lett.* 69 (19 1992), pp. 2847–2850. DOI: [10.1103/PhysRevLett.69.2847](https://doi.org/10.1103/PhysRevLett.69.2847).
- [100] F. Giazotto, K. Grove-Rasmussen, R. Fazio, F. Beltram, E. H. Linfield, and D. A. Ritchie. "Josephson Current in Nb/InAs/Nb Highly Transmissive Ballistic Junctions." *Journal of Superconductivity* 17.2 (2004), pp. 317–321. DOI: [10.1023/B:JOSC.0000021231.01260.94](https://doi.org/10.1023/B:JOSC.0000021231.01260.94).
- [101] M. Amado, A. Fornieri, F. Carillo, G. Biasiol, L. Sorba, V. Pellegrini, and F. Giazotto. "Electrostatic tailoring of magnetic interference in quantum point contact ballistic Josephson junctions." *Phys. Rev. B* 87 (13 2013), p. 134506. DOI: [10.1103/PhysRevB.87.134506](https://doi.org/10.1103/PhysRevB.87.134506).

- [102] J. Shabani, S. Das Sarma, and C. J. Palmstrøm. "An apparent metal-insulator transition in high-mobility two-dimensional InAs heterostructures." *Phys. Rev. B* 90 (16 2014), p. 161303. DOI: [10.1103/PhysRevB.90.161303](https://doi.org/10.1103/PhysRevB.90.161303).
- [103] J. Shabani, A. P. McFadden, B. Shojaei, and C. J. Palmstrøm. "Gating of high-mobility InAs metamorphic heterostructures." *Applied Physics Letters* 105.26 (2014), p. 262105. DOI: [10.1063/1.4905370](https://doi.org/10.1063/1.4905370).
- [104] J. Shabani, Y. Kim, A. P. McFadden, R. M. Lutchyn, C. Nayak, and C. J. palmstrøm. "Tuning spin orbit interaction in high quality gate-defined InAs one-dimensional channels." *ArXiv e-prints* (Aug. 2014).
- [105] D. Uhlisch, A. A. Golubov, M. Hollfelder, K. Neurohr, A. V. Ustinov, A. I. Braginski, and H. Lüth. "Investigation of Nb contacts to a GaInAs/InP heterostructure." *Czechoslovak Journal of Physics* 46.2 (1996), pp. 657–658. DOI: [10.1007/BF02583636](https://doi.org/10.1007/BF02583636).
- [106] L. C. Mur, C. J. P. M. Harmans, J. E. Mooij, J. F. Carlin, A. Rudra, and M. Ilegems. "Experimental indication for supercurrents carried by opened transport channels." *Phys. Rev. B* 54 (4 1996), R2327–R2330. DOI: [10.1103/PhysRevB.54.R2327](https://doi.org/10.1103/PhysRevB.54.R2327).
- [107] J. P. Heida, B. J. van Wees, T. M. Klapwijk, and G. Borghs. "Nonlocal supercurrent in mesoscopic Josephson junctions." *Phys. Rev. B* 57 (10 1998), pp. 5618–5621. DOI: [10.1103/PhysRevB.57.R5618](https://doi.org/10.1103/PhysRevB.57.R5618).
- [108] G. Bastian, E. O. Göbel, A. B. Zorin, H. Schulze, J. Niemeyer, T. Weimann, M. R. Bennett, and K. E. Singer. "Quasiparticle Interference Effects in a Ballistic Superconductor-Semiconductor-Superconductor Josephson Junction." *Phys. Rev. Lett.* 81 (8 1998), pp. 1686–1689. DOI: [10.1103/PhysRevLett.81.1686](https://doi.org/10.1103/PhysRevLett.81.1686).

- [109] H. Takayanagi and T. Akazaki. "Submicron Gate-Fitted Superconducting Junction Using a Two-Dimensional Electron Gas." *Japanese Journal of Applied Physics* 34.12S (1995), p. 6977.
- [110] K. Neurohr, T. Schäpers, J. Malindretos, S. Lachenmann, A. I. Braginski, H. Lüth, M. Behet, G. Borghs, and A. A. Golubov. "Local suppression of Josephson currents in niobium/two-dimensional electron gas/niobium structures by an injection current." *Phys. Rev. B* 59 (17 1999), pp. 11197–11200. DOI: [10.1103/PhysRevB.59.11197](https://doi.org/10.1103/PhysRevB.59.11197).
- [111] I. E. Batov, T. Schäpers, A. A. Golubov, and A. V. Ustinov. "Andreev reflection and enhanced subgap conductance in NbN/Au/InGaAs-InP junctions." *Journal of Applied Physics* 96.6 (2004), pp. 3366–3370. DOI: [10.1063/1.1783612](https://doi.org/10.1063/1.1783612).
- [112] B.-R. Choi, A. E. Hansen, T. Kontos, C. Hoffmann, S. Oberholzer, W. Belzig, C. Schönenberger, T. Akazaki, and H. Takayanagi. "Shot-noise and conductance measurements of transparent superconductor/two-dimensional electron gas junctions." *Phys. Rev. B* 72 (2 2005), p. 024501. DOI: [10.1103/PhysRevB.72.024501](https://doi.org/10.1103/PhysRevB.72.024501).
- [113] L. Wang, I. Meric, P. Y. Huang, Q. Gao, Y. Gao, H. Tran, T. Taniguchi, K. Watanabe, L. M. Campos, D. A. Muller, J. Guo, P. Kim, J. Hone, K. L. Shepard, and C. R. Dean. "One-Dimensional Electrical Contact to a Two-Dimensional Material." *Science* 342.6158 (2013), pp. 614–617. DOI: [10.1126/science.1244358](https://doi.org/10.1126/science.1244358).
- [114] V. E. Calado, S. Goswami, G. Nanda, M. Diez, A. R. Akhmerov, K. Watanabe, T. Taniguchi, T. M. Klapwijk, and L. M. K. Vandersypen. "Ballistic Josephson junctions in edge-contacted graphene." *Nature Nanotechnology* 10.9 (2015), pp. 761–764. DOI: [10.1038/nnano.2015.156](https://doi.org/10.1038/nnano.2015.156).

- [115] A. Clawson. "Guide to references on III–V semiconductor chemical etching." *Materials Science and Engineering: R: Reports* 31.1–6 (2001), pp. 1–438. DOI: [https://doi.org/10.1016/S0927-796X\(00\)00027-9](https://doi.org/10.1016/S0927-796X(00)00027-9).
- [116] P. H. C. Magnée, S. G. den Hartog, B. J. van Wees, T. M. Klapwijk, W. van de Graaf, and G. Borghs. "Experimental determination of the quasiparticle decay length ξ_{qp} in a diffusive superconducting quantum well." *Phys. Rev. B* 52 (16 1995), R11630–R11633. DOI: [10.1103/PhysRevB.52.R11630](https://doi.org/10.1103/PhysRevB.52.R11630).
- [117] E. Philofsky. "Intermetallic formation in gold-aluminum systems." *Solid-State Electronics* 13.10 (1970), pp. 1391–1394. DOI: [http://dx.doi.org/10.1016/0038-1101\(70\)90172-3](http://dx.doi.org/10.1016/0038-1101(70)90172-3).
- [118] M. Kjaergaard. "Proximity Induced Superconducting Properties In One And Two Dimensional Semiconductors: Towards Topological States Of Matter." PhD thesis. Copenhagen University, Sept. 2015.
- [119] I. Yanson. "Effect of Fluctuations on the Dependence of the Josephson Current on the Magnetic Field." *Soviet Physics JETP* 31 (1970), pp. 800–806.
- [120] R. C. Dynes and T. A. Fulton. "Supercurrent Density Distribution in Josephson Junctions." *Phys. Rev. B* 3 (9 1971), pp. 3015–3023. DOI: [10.1103/PhysRevB.3.3015](https://doi.org/10.1103/PhysRevB.3.3015).
- [121] A. Barone, G. Paternò, M. Russo, and R. Vaglio. "Diffraction and interference phenomena in single Josephson junctions." *physica status solidi (a)* 41.2 (1977), pp. 393–401. DOI: [10.1002/pssa.2210410206](https://doi.org/10.1002/pssa.2210410206).
- [122] A. Barone, G. Paternò, M. Russo, and R. Vaglio. "Experimental results and analysis of structural fluctuations in photosensitive Josephson junctions." *Sov. Phys. JETP*, 47.4 (1978), pp. 776–778.

- [123] K. K. Likharev. "Superconducting weak links." *Rev. Mod. Phys.* 51 (1 1979), pp. 101–159. DOI: [10.1103/RevModPhys.51.101](https://doi.org/10.1103/RevModPhys.51.101).
- [124] C. W. J. Beenakker. "Quantum transport in semiconductor-superconductor microjunctions." *Phys. Rev. B* 46 (19 1992), pp. 12841–12844. DOI: [10.1103/PhysRevB.46.12841](https://doi.org/10.1103/PhysRevB.46.12841).
- [125] W. Chang, S. M. Albrecht, T. S. Jespersen, F. Kuemmeth, P. Krogstrup, J. Nygård, and C. M. Marcus. "Hard gap in epitaxial semiconductor–superconductor nanowires." *Nature Nanotechnology* 10.3 (2015), pp. 232–236.
- [126] L. Pfeiffer, H. Störmer, K. Baldwin, K. West, A. Goñi, A. Pinczuk, R. Ashoori, M. Dignam, and W. Wegscheider. "Cleaved edge overgrowth for quantum wire fabrication." *Journal of Crystal Growth* 127.1 (1993), pp. 849–857. DOI: [http://dx.doi.org/10.1016/0022-0248\(93\)90746-J](http://dx.doi.org/10.1016/0022-0248(93)90746-J).
- [127] P. Krogstrup, N. L. B. Ziino, W. Chang, S. M. Albrecht, M. H. Madsen, E. Johnson, J. Nygård, C. M. Marcus, and T. S. Jespersen. "Epitaxy of semiconductor–superconductor nanowires." *Nature Materials* 14.4 (2015), pp. 400–406. DOI: [10.1038/nmat4176](https://doi.org/10.1038/nmat4176).
- [128] R. Taboryski, T. Clausen, J. B. Hansen, J. L. Skov, J. Kutchinsky, C. B. Sorensen, and P. E. Lindelof. "Andreev reflections at interfaces between δ -doped GaAs and superconducting Al films." *Applied Physics Letters* 69.5 (1996), pp. 656–658. DOI: [10.1063/1.117796](https://doi.org/10.1063/1.117796).
- [129] R. Taboryski, T. Clausen, J. Kutchinsky, C. B. Sorensen, P. E. Lindelof, J. B. Hansen, and J. L. Skov. "Superconductor-semiconductor-superconductor planar junctions of aluminium on δ -doped gallium-arsenide." *IEEE Transactions on Applied Superconductivity* 7.2 (1997), pp. 2809–2813. DOI: [10.1109/77.621821](https://doi.org/10.1109/77.621821).

- [130] D. A. Williams. "NS junctions using high-mobility GaAs:AlGaAs heterostructures." *Superlattices and Microstructures* 25.5 (1999), pp. 701–709. DOI: <http://dx.doi.org/10.1006/spmi.1999.0716>.
- [131] J. Kutchinsky, R. Taboryski, T. Clausen, C. B. Sørensen, A. Kristensen, P. E. Lindelof, J. Bindslev Hansen, C. Schelde Jacobsen, and J. L. Skov. "Decay Lengths for Diffusive Transport Activated by Andreev Reflections in Al/n-GaAs/Al Superconductor-Semiconductor-Superconductor Junctions." *Phys. Rev. Lett.* 78 (5 1997), pp. 931–934. DOI: [10.1103/PhysRevLett.78.931](https://doi.org/10.1103/PhysRevLett.78.931).
- [132] J. Kutchinsky, R. Taboryski, C. B. Sørensen, J. B. Hansen, and P. E. Lindelof. "Observation of Supercurrent Enhancement in SNS Junctions by Nonequilibrium Injection into Supercurrent Carrying Bound Andreev States." *Phys. Rev. Lett.* 83 (23 1999), pp. 4856–4859. DOI: [10.1103/PhysRevLett.83.4856](https://doi.org/10.1103/PhysRevLett.83.4856).
- [133] J. Kutchinsky, R. Taboryski, O. Kuhn, C. B. Sørensen, P. E. Lindelof, A. Kristensen, J. Bindslev Hansen, C. Schelde Jacobsen, and J. L. Skov. "Coherent diffusive transport mediated by Andreev reflections at $V = \Delta/e$ in a mesoscopic superconductor/semiconductor/superconductor junction." *Phys. Rev. B* 56 (6 1997), R2932–R2935. DOI: [10.1103/PhysRevB.56.R2932](https://doi.org/10.1103/PhysRevB.56.R2932).
- [134] R. Taboryski, J. Kutchinsky, J. B. Hansen, M. Wildt, C. B. Sørensen, and P. E. Lindelof. "Multiple Andreev reflections in diffusive SNS structures." *Superlattices and Microstructures* 25.5 (1999), pp. 829–837. DOI: <http://dx.doi.org/10.1006/spmi.1999.0712>.
- [135] B. Shojaei, A. McFadden, J. Shabani, B. D. Schultz, and C. J. Palmstrøm. "Studies of scattering mechanisms in gate tunable InAs/(Al,Ga)Sb two dimensional electron gases." *Ap-*

- plied Physics Letters* 106.22 (2015), p. 222101. DOI: [10.1063/1.4921970](https://doi.org/10.1063/1.4921970).
- [136] B. Shojaei, A. C. C. Drachmann, M. Pendharkar, D. J. Pennachio, M. P. Echlin, P. G. Callahan, S. Kraemer, T. M. Pollock, C. M. Marcus, and C. J. Palmstrøm. "Limits to mobility in InAs quantum wells with nearly lattice-matched barriers." *Phys. Rev. B* 94 (24 2016), p. 245306. DOI: [10.1103/PhysRevB.94.245306](https://doi.org/10.1103/PhysRevB.94.245306).
- [137] B. Shojaei, P. J. J. O'Malley, J. Shabani, P. Roushan, B. D. Schultz, R. M. Lutchyn, C. Nayak, J. M. Martinis, and C. J. Palmstrøm. "Demonstration of gate control of spin splitting in a high-mobility InAs/AlSb two-dimensional electron gas." *Phys. Rev. B* 93 (7 2016), p. 075302. DOI: [10.1103/PhysRevB.93.075302](https://doi.org/10.1103/PhysRevB.93.075302).
- [138] W. S. Cole, S. Das Sarma, and T. D. Stanescu. "Effects of large induced superconducting gap on semiconductor Majorana nanowires." *Phys. Rev. B* 92.17 (Nov. 2015), p. 174511.
- [139] T. D. Stanescu, R. M. Lutchyn, and S. Das Sarma. "Majorana fermions in semiconductor nanowires." *Phys. Rev. B* 84 (14 2011), p. 144522. DOI: [10.1103/PhysRevB.84.144522](https://doi.org/10.1103/PhysRevB.84.144522).
- [140] J. Alicea. "Majorana fermions in a tunable semiconductor device." *Phys. Rev. B* 81 (12 2010), p. 125318. DOI: [10.1103/PhysRevB.81.125318](https://doi.org/10.1103/PhysRevB.81.125318).
- [141] J. F. Cochran and D. E. Mapother. "Superconducting Transition in Aluminum." *Phys. Rev.* 111 (1 1958), pp. 132–142. DOI: [10.1103/PhysRev.111.132](https://doi.org/10.1103/PhysRev.111.132).
- [142] I. S. Khukhareva. "The Superconducting Properties of Thin Aluminum Films." *JETP Lett.* 16.4 (1963).

- [143] R. Meservey and D. H. Douglass. "Energy Gap Measurements by Tunneling between Superconducting Films. II. Magnetic Field Dependence." *Phys. Rev.* 135 (1A 1964), A24–A33. DOI: [10.1103/PhysRev.135.A24](https://doi.org/10.1103/PhysRev.135.A24).
- [144] P. M. Tedrow and R. Meservey. "Critical magnetic field of very thin superconducting aluminum films." *Phys. Rev. B* 25 (1 1982), pp. 171–178. DOI: [10.1103/PhysRevB.25.171](https://doi.org/10.1103/PhysRevB.25.171).
- [145] Y. L. Loh, N. Trivedi, Y. M. Xiong, P. W. Adams, and G. Catelani. "Origin of Excess Low-Energy States in a Disordered Superconductor in a Zeeman Field." *Phys. Rev. Lett.* 107 (6 2011), p. 067003. DOI: [10.1103/PhysRevLett.107.067003](https://doi.org/10.1103/PhysRevLett.107.067003).
- [146] B. S. Chandrasekhar. "A note on the maximum critical field of high-field superconductors." *Applied Physics Letters* 1.1 (1962), pp. 7–8. DOI: [10.1063/1.1777362](https://doi.org/10.1063/1.1777362).
- [147] A. M. Clogston. "Upper Limit for the Critical Field in Hard Superconductors." *Phys. Rev. Lett.* 9 (6 1962), pp. 266–267. DOI: [10.1103/PhysRevLett.9.266](https://doi.org/10.1103/PhysRevLett.9.266).
- [148] P. Wójcik. "Thickness-Dependent Oscillations of the Critical Magnetic Field Induced by the Quantum Size Effect in Superconducting Nanofilms." *Journal of Superconductivity and Novel Magnetism* 28.2 (2015), pp. 339–343. DOI: [10.1007/s10948-014-2676-z](https://doi.org/10.1007/s10948-014-2676-z).
- [149] S. Iordanskii, Y. Lyanda-Geller, and G. Pikus. "Pis'ma Zh. Eksp. Teor. Fiz. 60, 199." *JETP Lett.* 60 (1994), p. 206.
- [150] W. Knap, C. Skierbiszewski, A. Zduniak, E. Litwin-Staszewska, D. Bertho, F. Kobbi, J. L. Robert, G. E. Pikus, F. G. Pikus, S. V. Iordanskii, V. Mosser, K. Zekentes, and Y. B. Lyanda-Geller. "Weak antilocalization and spin precession in quantum wells." *Phys. Rev. B* 53 (7 1996), p. 3912. DOI: [10.1103/PhysRevB.53.3912](https://doi.org/10.1103/PhysRevB.53.3912).

- [151] J. Shabani, M. Kjaergaard, H. J. Suominen, Y. Kim, F. Nichele, K. Pakrouski, T. Stankevic, R. M. Lutchyn, P. Krogstrup, R. Feidenhans'l, S. Kraemer, C. Nayak, M. Troyer, C. M. Marcus, and C. J. Palmstrøm. "Two-dimensional epitaxial superconductor-semiconductor heterostructures: A platform for topological superconducting networks." *Phys. Rev. B* 93 (15 2016), p. 155402. DOI: [10.1103/PhysRevB.93.155402](https://doi.org/10.1103/PhysRevB.93.155402).
- [152] M. Kjaergaard*, **H. J. Suominen***, M. P. Nowak, A. R. Akhmerov, J. Shabani, C. J. Palmstrøm, F. Nichele, and C. M. Marcus. "Transparent Semiconductor-Superconductor Interface and Induced Gap in an Epitaxial Heterostructure Josephson Junction." *Physical Review Applied* 7 (3 2017), p. 034029. DOI: [10.1103/PhysRevApplied.7.034029](https://doi.org/10.1103/PhysRevApplied.7.034029).
- [153] B. A. Aminov, A. A. Golubov, and M. Y. Kupriyanov. "Quasiparticle current in ballistic constrictions with finite transparencies of interfaces." *Phys. Rev. B* 53.1 (1996), pp. 365–373.
- [154] C. R. Reeg and D. L. Maslov. "Hard gap in a normal layer coupled to a superconductor." *Phys. Rev. B* 94 (2 2016), p. 020501. DOI: [10.1103/PhysRevB.94.020501](https://doi.org/10.1103/PhysRevB.94.020501).
- [155] A. A. Golubov and M. Y. Kupriyanov. "Quasiparticle current in ballistic NcN'S junctions." *Physica C* 259.1-2 (1996), pp. 27–35.
- [156] M. Kjaergaard, F. Nichele, H. J. Suominen, M. P. Nowak, M. Wimmer, A. R. Akhmerov, J. A. Folk, K. Flensberg, J. Shabani, C. J. Palmstrøm, and C. M. Marcus. "Quantized conductance doubling and hard gap in a two-dimensional semiconductor–superconductor heterostructure." *Nat. Commun.* 7 (2016), p. 12841. DOI: [10.1038/ncomms12841](https://doi.org/10.1038/ncomms12841).

- [157] D Averin and A Bardas. "ac Josephson Effect in a Single Quantum Channel." *Phys. Rev. Lett.* 75.9 (Aug. 1995), pp. 1831–1834.
- [158] S Li, N Kang, D. X. Fan, L. B. Wang, Y. Q. Huang, P Caroff, and H. Q. Xu. "Coherent Charge Transport in Ballistic InSb Nanowire Josephson Junctions." *Scientific Reports* 6 (Apr. 2016), p. 24822.
- [159] R. Meservey and B. B. Schwartz. "Equilibrium properties: comparison of experimental results with predictions of the BCS theory." *Superconductivity Vol. 1*. Ed. by R. D. Parks. New York: Marcel Dekker Inc., 1969, p. 126.
- [160] R Meservey and P. M. Tedrow. "Properties of very thin aluminum films." *Journal of Applied Physics* 42.51 (1971).
- [161] N. A. Court, A. J. Ferguson, and R. G. Clark. "Energy gap measurement of nanostructured aluminium thin films for single Cooper-pair devices." *Superconductor Science and Technology* 21.1 (Jan. 2008), p. 015013.
- [162] M Octavio, M Tinkham, G. E. Blonder, and T Klapwijk. "Subharmonic energy-gap structure in superconducting constrictions." *Phys. Rev. B* 27.11 (June 1983), pp. 6739–6746.
- [163] A. W. Kleinsasser, T. N. Jackson, D McInturff, F Rammo, G. D. Pettit, and J. M. Woodall. "Crossover from tunneling to metallic behavior in superconductor-semiconductor contacts." *Appl. Phys. Lett.* 57.17 (1990), p. 1811.
- [164] S. N. Artemenko, A. F. Volkov, and A. V. Zaitsev. "On the excess current in microbridges S-c-S and S-c-N." *Solid State Communications* 30.12 (June 1979), pp. 771–773.
- [165] C. Nguyen, H. Kroemer, and E. L. Hu. "Contact resistance of superconductor-semiconductor interfaces: The case of Nb-InAs/AlSb quantum-well structures." *Applied Physics Letters* 65.1 (1994), pp. 103–105. DOI: [10.1063/1.113047](https://doi.org/10.1063/1.113047).

- [166] B. Ludoph, N. van der Post, E. N. Bratus, E. V. Bezuglyi, V. S. Shumeiko, G. Wendin, and J. M. van Ruitenbeek. "Multiple Andreev reflection in single-atom niobium junctions." *Phys. Rev. B* 61 (12 2000), pp. 8561–8569. DOI: [10.1103/PhysRevB.61.8561](https://doi.org/10.1103/PhysRevB.61.8561).
- [167] M. T. Allen, O. Shtanko, I. C. Fulga, A. R. Akhmerov, K. Watanabe, T. Taniguchi, P. Jarillo-Herrero, L. S. Levitov, and A. Yacoby. "Spatially resolved edge currents and guided-wave electronic states in graphene." *Nat Phys* 12.2 (Feb. 2016), pp. 128–133.
- [168] N. S. Averkiev, L. E. Golub, S. A. Tarasenko, and M. Willander. "Theory of magneto-oscillation effects in quasi-two-dimensional semiconductor structures." *Journal of Physics: Condensed Matter* 13.11 (Mar. 2001), pp. 2517–2530.
- [169] A. F. Volkov, P. H. C. Magnée, B. J. Van Wees, and T. M. Klapwijk. "Proximity and Josephson effects in superconductor-two-dimensional electron gas planar junctions." *Physica C: Superconductivity* 242.3-4 (Feb. 1995), pp. 261–266.
- [170] **H. J. Suominen**, J. Danon, M. Kjaergaard, K. Flensberg, J. Shabani, C. J. Palmstrøm, F. Nichele, and C. M. Marcus. "Anomalous Fraunhofer interference in epitaxial superconductor-semiconductor Josephson junctions." *Physical Review B* 95 (3 2017), p. 035307. DOI: [10.1103/PhysRevB.95.035307](https://doi.org/10.1103/PhysRevB.95.035307).
- [171] P. San-Jose, J. Cayao, E. Prada, and R. Aguado. "Multiple Andreev reflection and critical current in topological superconducting nanowire junctions." *New J. Phys.* 15.7 (2013), p. 075019.
- [172] P. San-Jose, E. Prada, and R. Aguado. "Mapping the Topological Phase Diagram of Multiband Semiconductors with Supercurrents." *Phys. Rev. Lett.* 112 (13 2014), p. 137001. DOI: [10.1103/PhysRevLett.112.137001](https://doi.org/10.1103/PhysRevLett.112.137001).

- [173] M. Hell, M. Leijnse, and K. Flensberg. "Two-Dimensional Platform for Networks of Majorana Bound States." *Phys. Rev. Lett.* 118 (10 2017), p. 107701. DOI: [10.1103/PhysRevLett.118.107701](https://doi.org/10.1103/PhysRevLett.118.107701).
- [174] F. Pientka, A. Keselman, E. Berg, A. Yacoby, A. Stern, and B. I. Halperin. "Topological Superconductivity in a Planar Josephson Junction." *Phys. Rev. X* 7 (2 2017), p. 021032. DOI: [10.1103/PhysRevX.7.021032](https://doi.org/10.1103/PhysRevX.7.021032).
- [175] J.-F. Liu and K. S. Chan. "Relation between symmetry breaking and the anomalous Josephson effect." *Phys. Rev. B* 82 (12 2010), p. 125305. DOI: [10.1103/PhysRevB.82.125305](https://doi.org/10.1103/PhysRevB.82.125305).
- [176] E. V. Bezuglyi, A. S. Rozhavsky, I. D. Vagner, and P. Wyder. "Combined effect of Zeeman splitting and spin-orbit interaction on the Josephson current in a superconductor–two-dimensional electron gas–superconductor structure." *Phys. Rev. B* 66 (5 2002), p. 052508. DOI: [10.1103/PhysRevB.66.052508](https://doi.org/10.1103/PhysRevB.66.052508).
- [177] B. Béri, J. H. Bardarson, and C. W. J. Beenakker. "Splitting of Andreev levels in a Josephson junction by spin-orbit coupling." *Phys. Rev. B* 77.4 (2008), p. 045311. DOI: [10.1103/PhysRevB.77.045311](https://doi.org/10.1103/PhysRevB.77.045311).
- [178] A. A. Reynoso, G. Usaj, C. A. Balseiro, D. Feinberg, and M. Avignon. "Anomalous Josephson Current in Junctions with Spin Polarizing Quantum Point Contacts." *Phys. Rev. Lett.* 101.10 (2008), p. 107001. DOI: [10.1103/physrevlett.101.107001](https://doi.org/10.1103/physrevlett.101.107001).
- [179] A. A. Reynoso, G. Usaj, C. A. Balseiro, D. Feinberg, and M. Avignon. "Spin-orbit-induced chirality of Andreev states in Josephson junctions." *Phys. Rev. B* 86.21 (2012), p. 214519. DOI: [10.1103/PhysRevB.86.214519](https://doi.org/10.1103/PhysRevB.86.214519).

- [180] T. Yokoyama, M. Eto, and Y. V. Nazarov. "Anomalous Josephson effect induced by spin-orbit interaction and Zeeman effect in semiconductor nanowires." *Phys. Rev. B* 89.19 (2014), p. 195407. DOI: [10.1103/physrevb.89.195407](https://doi.org/10.1103/physrevb.89.195407).
- [181] T. Nishino, U. Kawabe, and E. Yamada. "Magnetic field dependence of the critical superconducting current induced by the proximity effect in silicon." *Phys. Rev. B* 34 (7 1986), pp. 4857–4860. DOI: [10.1103/PhysRevB.34.4857](https://doi.org/10.1103/PhysRevB.34.4857).
- [182] S. L. Miller, K. R. Biagi, J. R. Clem, and D. K. Finnemore. "Critical currents of cross-type superconducting-normal-superconducting junctions in perpendicular magnetic fields." *Phys. Rev. B* 31 (5 1985), pp. 2684–2693. DOI: [10.1103/PhysRevB.31.2684](https://doi.org/10.1103/PhysRevB.31.2684).
- [183] H.-Y. Hui, A. M. Lobos, J. D. Sau, and S. Das Sarma. "Proximity-induced superconductivity and Josephson critical current in quantum spin Hall systems." *Phys. Rev. B* 90 (22 2014), p. 224517. DOI: [10.1103/PhysRevB.90.224517](https://doi.org/10.1103/PhysRevB.90.224517).
- [184] J. H. Lee, G.-H. Lee, J. Park, J. Lee, S.-G. Nam, Y.-S. Shin, J. S. Kim, and H.-J. Lee. "Local and Nonlocal Fraunhofer-like Pattern from an Edge-Stepped Topological Surface Josephson Current Distribution." *Nano Letters* 14.9 (2014). PMID: 25084551, pp. 5029–5034. DOI: [10.1021/nl501481b](https://doi.org/10.1021/nl501481b).
- [185] S. Hart, H. Ren, T. Wagner, P. Leubner, M. Muhlbauer, C. Brune, H. Buhmann, L. W. Molenkamp, and A. Yacoby. "Induced superconductivity in the quantum spin Hall edge." *Nat. Phys.* 10.9 (Sept. 2014), pp. 638–643.
- [186] V. S. Pribiag, A. J. A. Beukman, F. Qu, M. C. Cassidy, C. Charpentier, W. Wegscheider, and L. P. Kouwenhoven. "Edge-mode superconductivity in a two-dimensional topological insulator." *Nat. Nano* 10.7 (July 2015), pp. 593–597.

- [187] H. Courtois, M. Meschke, J. T. Peltonen, and J. P. Pekola. "Origin of Hysteresis in a Proximity Josephson Junction." *Phys. Rev. Lett.* 101 (6 2008), p. 067002. DOI: [10.1103/PhysRevLett.101.067002](https://doi.org/10.1103/PhysRevLett.101.067002).
- [188] E. H. Brandt and M. Indenbom. "Type-II-superconductor strip with current in a perpendicular magnetic field." *Phys. Rev. B* 48 (17 1993), pp. 12893–12906. DOI: [10.1103/PhysRevB.48.12893](https://doi.org/10.1103/PhysRevB.48.12893).
- [189] A. Barone and G. Paterno. *Physics and Applications of the Josephson Effect*. New York: Wiley and Sons, 1982.
- [190] Y. Harada, S. Jensen, T. Akazaki, and H. Takayanagi. "Anomalous magnetic flux periodicity of supercurrent in mesoscopic SNS Josephson junctions." *Physica C: Superconductivity* 367.1-4 (2002), pp. 229–233. DOI: [http://dx.doi.org/10.1016/S0921-4534\(01\)01023-1](http://dx.doi.org/10.1016/S0921-4534(01)01023-1).
- [191] J. Paajaste, M. Amado, S. Roddaro, F. S. Bergeret, D. Ercolani, L. Sorba, and F. Giazotto. "Pb/InAs Nanowire Josephson Junction with High Critical Current and Magnetic Flux Focusing." *Nano Lett.* 15.3 (2015), pp. 1803–1808. DOI: [10.1021/nl504544s](https://doi.org/10.1021/nl504544s).
- [192] E. Zeldov, J. R. Clem, M. McElfresh, and M. Darwin. "Magnetization and transport currents in thin superconducting films." *Phys. Rev. B* 49 (14 1994), pp. 9802–9822. DOI: [10.1103/PhysRevB.49.9802](https://doi.org/10.1103/PhysRevB.49.9802).
- [193] J. Gu, W. Cha, K. Gamo, and S. Namba. "Properties of niobium superconducting bridges prepared by electron-beam lithography and ion implantation." *J. Appl. Phys.* 50.10 (1979), pp. 6437–6442. DOI: <http://dx.doi.org/10.1063/1.325736>.

- [194] A. Rasmussen, J. Danon, H. Suominen, F. Nichele, M. Kjaergaard, and K. Flensberg. "Effects of spin-orbit coupling and spatial symmetries on the Josephson current in SNS junctions." *Phys. Rev. B* 93 (15 2016), p. 155406. DOI: [10.1103/PhysRevB.93.155406](https://doi.org/10.1103/PhysRevB.93.155406).
- [195] A. A. Golubov, M. Y. Kupriyanov, and E. Il'ichev. "The current-phase relation in Josephson junctions." *Rev. Mod. Phys.* 76 (2 2004), pp. 411–469. DOI: [10.1103/RevModPhys.76.411](https://doi.org/10.1103/RevModPhys.76.411).
- [196] T. Golod, A. Rydh, and V. M. Krasnov. "Detection of the Phase Shift from a Single Abrikosov Vortex." *Phys. Rev. Lett.* 104.22 (2010).
- [197] M. V. Fistul'. "Mesoscopic behavior of Josephson junctions with randomly disposed Abrikosov vortices." *JETP Lett.* 69.1 (1989), pp. 209–213.
- [198] M. A. Itzler and M. Tinkham. "Vortex pinning by disordered columnar defects in large Josephson junctions." *Phys. Rev. B* 53 (18 1996), R11949–R11952. DOI: [10.1103/PhysRevB.53.R11949](https://doi.org/10.1103/PhysRevB.53.R11949).
- [199] M. V. Fistul' and G. F. Giuliani. "Theory of finite-size effects and vortex penetration in small Josephson junctions." *Phys. Rev. B* 51 (2 1995), pp. 1090–1095. DOI: [10.1103/PhysRevB.51.1090](https://doi.org/10.1103/PhysRevB.51.1090).
- [200] **H. J. Suominen**, M. Kjaergaard, A. R. Hamilton, J. Shabani, C. J. Palmstrøm, C. M. Marcus, and F. Nichele. "Zero-Energy Modes from Coalescing Andreev States in a Two-Dimensional Semiconductor-Superconductor Hybrid Platform." *Under review* (2017).
- [201] A. Kitaev. "Fault-tolerant quantum computation by anyons." *Annals of Physics* 303.1 (2003), pp. 2–30. DOI: [10.1016/s0003-4916\(02\)00018-0](https://doi.org/10.1016/s0003-4916(02)00018-0).

- [202] J. Alicea, Y. Oreg, G. Refael, F. von Oppen, and M. P. Fisher. “Non-Abelian statistics and topological quantum information processing in 1D wire networks.” *Nat. Phys.* 7.5 (2011), pp. 412–417.
- [203] D. Aasen, M. Hell, R. V. Mishmash, A. Higginbotham, J. Danon, M. Leijnse, T. S. Jespersen, J. A. Folk, C. M. Marcus, K. Flensberg, and J. Alicea. “Milestones Toward Majorana-Based Quantum Computing.” *Phys. Rev. X* 6 (3 2016), p. 031016. DOI: [10.1103/PhysRevX.6.031016](https://doi.org/10.1103/PhysRevX.6.031016).
- [204] S. Vijay and L. Fu. “Teleportation-based quantum information processing with Majorana zero modes.” *Phys. Rev. B* 94 (23 2016), p. 235446. DOI: [10.1103/PhysRevB.94.235446](https://doi.org/10.1103/PhysRevB.94.235446).
- [205] T. Karzig, C. Knapp, R. M. Lutchyn, P. Bonderson, M. B. Hastings, C. Nayak, J. Alicea, K. Flensberg, S. Plugge, Y. Oreg, C. M. Marcus, and M. H. Freedman. “Scalable designs for quasiparticle-poisoning-protected topological quantum computation with Majorana zero modes.” *Phys. Rev. B* 95 (23 2017), p. 235305. DOI: [10.1103/PhysRevB.95.235305](https://doi.org/10.1103/PhysRevB.95.235305).
- [206] S. Plugge, A. Rasmussen, R. Egger, and K. Flensberg. “Majorana box qubits.” *New Journal of Physics* 19.1 (2017), p. 012001.
- [207] M. Hofheinz. “Coulomb blockade in silicon nanowire MOSFETs.” PhD thesis. Université Joseph Fourier (Grenoble), 2006.
- [208] V. V. Moshchalkov, L. Gielen, C. Strunk, R. Jonckheere, X. Qiu, C. V. Haesendonck, and Y. Bruynseraede. “Effect of sample topology on the critical fields of mesoscopic superconductors.” *Nature* 373.6512 (1995), pp. 319–322. DOI: [10.1038/373319a0](https://doi.org/10.1038/373319a0).

- [209] M. Poza, E. Bascones, J. G. Rodrigo, N. Agraït, S. Vieira, and F. Guinea. "Nanosized superconducting constrictions." *Phys. Rev. B* 58 (17 1998), pp. 11173–11176. DOI: [10.1103/PhysRevB.58.11173](https://doi.org/10.1103/PhysRevB.58.11173).
- [210] E. L. Wolf. *Principles of Electron Tunneling Spectroscopy Second Edition*. Oxford University Press (OUP), 2011. DOI: [10.1093/acprof:oso/9780199589494.001.0001](https://doi.org/10.1093/acprof:oso/9780199589494.001.0001).
- [211] M. Iansiti, M. Tinkham, A. T. Johnson, W. F. Smith, and C. J. Lobb. "Charging effects and quantum properties of small superconducting tunnel junctions." *Phys. Rev. B* 39 (10 1989), pp. 6465–6484. DOI: [10.1103/PhysRevB.39.6465](https://doi.org/10.1103/PhysRevB.39.6465).
- [212] K. T. Law, P. A. Lee, and T. K. Ng. "Majorana Fermion Induced Resonant Andreev Reflection." *Phys. Rev. Lett.* 103 (23 2009), p. 237001. DOI: [10.1103/PhysRevLett.103.237001](https://doi.org/10.1103/PhysRevLett.103.237001).
- [213] K. Flensberg. "Tunneling characteristics of a chain of Majorana bound states." *Phys. Rev. B* 82 (18 2010), p. 180516. DOI: [10.1103/PhysRevB.82.180516](https://doi.org/10.1103/PhysRevB.82.180516).
- [214] Y. Nakamura, D. L. Klein, and J. S. Tsai. "Al/Al₂O₃/Al single electron transistors operable up to 30 K utilizing anodization controlled miniaturization enhancement." *Applied Physics Letters* 68.2 (1996), pp. 275–277. DOI: [10.1063/1.115661](https://doi.org/10.1063/1.115661).
- [215] G. Hass. "On the Preparation of Hard Oxide Films with Precisely Controlled Thickness on Evaporated Aluminum Mirrors." *J. Opt. Soc. Am.* 39.7 (1949), pp. 532–540. DOI: [10.1364/JOSA.39.000532](https://doi.org/10.1364/JOSA.39.000532).
- [216] J. Hauser. "Penetration depth and related properties of Al films with enhanced superconductivity." *J. Low Temp. Phys.* 7:3-4 (1972), pp. 335–349. DOI: [10.1007/BF00660071](https://doi.org/10.1007/BF00660071).

- [217] A. I. Gubin, K. S. Il'in, S. A. Vitusevich, M. Siegel, and N. Klein. "Dependence of magnetic penetration depth on the thickness of superconducting Nb thin films." *Phys. Rev. B* 72 (6 2005), p. 064503. DOI: [10.1103/PhysRevB.72.064503](https://doi.org/10.1103/PhysRevB.72.064503).
- [218] J. Pearl. "Current distribution in superconducting films carrying quantized fluxoids." *Appl. Phys. Lett.* 5.4 (1964), pp. 65–66. DOI: [10.1063/1.1754056](https://doi.org/10.1063/1.1754056).
- [219] V. N. Gladilin, J. Ge, J. Gutierrez, M. Timmermans, J. V. de Vondel, J. Tempere, J. T. Devreese, and V. V. Moshchalkov. "Vortices in a wedge made of a type-I superconductor." *New J. Phys.* 17.6 (2015), p. 063032.
- [220] J. Gutierrez, B. Raes, J. Van de Vondel, A. V. Silhanek, R. B. G. Kramer, G. W. Ataklti, and V. V. Moshchalkov. "First vortex entry into a perpendicularly magnetized superconducting thin film." *Phys. Rev. B* 88 (18 2013), p. 184504. DOI: [10.1103/PhysRevB.88.184504](https://doi.org/10.1103/PhysRevB.88.184504).